

7-2-2011

# Electromagnetic pulse technology : biological and terahertz applications

Prashanth Kumar

Follow this and additional works at: [https://digitalrepository.unm.edu/ece\\_etds](https://digitalrepository.unm.edu/ece_etds)

---

## Recommended Citation

Kumar, Prashanth. "Electromagnetic pulse technology : biological and terahertz applications." (2011).  
[https://digitalrepository.unm.edu/ece\\_etds/145](https://digitalrepository.unm.edu/ece_etds/145)

This Dissertation is brought to you for free and open access by the Engineering ETDs at UNM Digital Repository. It has been accepted for inclusion in Electrical and Computer Engineering ETDs by an authorized administrator of UNM Digital Repository. For more information, please contact [disc@unm.edu](mailto:disc@unm.edu).

Prashanth Kumar

*Candidate*

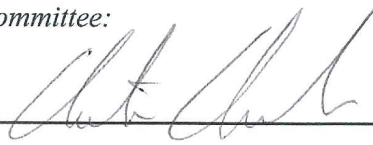
Electrical and Computer Engineering

*Department*

This dissertation is approved, and it is acceptable in quality and form for publication:

*Approved by the Dissertation Committee:*

Prof. Christos G. Christodoulou



, Chairperson

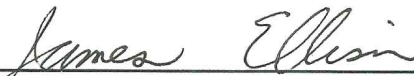
Prof. Edl Schamiloglu



Prof. C. Jerald Buchenauer



Prof. James Ellison



Dr. Kenneth F. McDonald



# **Electromagnetic Pulse Technology: Biological and Terahertz Applications**

by

**Prashanth Kumar**

B.E., University of Madras, 2003  
M.S., University of New Mexico, 2007

DISSERTATION

Submitted in Partial Fulfillment of the  
Requirements for the Degree of

Doctor of Philosophy  
Engineering

The University of New Mexico  
Albuquerque, New Mexico

May, 2011

©2011, Prashanth Kumar

# Dedication

*To my mentor and friend, Dr. Carl E. Baum.*

# Acknowledgments

First and foremost I owe my sincerest gratitude to my research advisor, Dr. Carl E. Baum, for having motivated and challenged me throughout my research. His patience, guidance and insight were invaluable. I could not have imagined having a better advisor and mentor. His untimely demise in December 2010 has left me feeling fortunate for having worked with this gentle giant of electromagnetics.

I would like to express the deepest appreciation to my academic advisor, Dr. Christos Christodoulou. I am extremely grateful for his guidance, advice and encouragement in this endeavor.

My sincere thanks also goes to my co-advisor, Dr. Edl Schamiloglu, for his assistance, recommendations and personal contacts pertaining to this work. I am also thankful to Dr. Jerald Buchenauer for his help with the experiments and the many valuable discussions we had.

Last but not least, I am greatly indebted to my friend and colleague, Dr. Serhat Altunc, whose immense help gave me confidence and helped accelerate the research.

# Electromagnetic Pulse Technology: Biological and Terahertz Applications

by

**Prashanth Kumar**

ABSTRACT OF DISSERTATION

Submitted in Partial Fulfillment of the  
Requirements for the Degree of

Doctor of Philosophy  
Engineering

The University of New Mexico

Albuquerque, New Mexico

May, 2011

# Electromagnetic Pulse Technology: Biological and Terahertz Applications

by

**Prashanth Kumar**

B.E., University of Madras, 2003

M.S., University of New Mexico, 2007

Ph.D., Engineering, University of New Mexico, 2011

## Abstract

Since the mid-1970s, the field of Electromagnetic Pulse (EMP) technology has extended to include High-Power Electromagnetic (HPE) sources/antennas. Two such EMP/HPE antennas, designed to address unique applications, are presented in this dissertation.

The first is the Prolate-Spheroidal Impulse-Radiating Antenna (PSIRA). Such an antenna uses a prolate-spheroidal reflector and has two foci. A fast ( $\leq 100$  ps), high-voltage ( $> 100$  kV) pulse launched from the first focal point is focused into a target located at the second focal point (near-field). It has been found that these pulses are useful for a variety of biological applications, such as accelerated wound healing and skin cancer (melanoma) treatment. Two lens designs for the PSIRA are explored. The first lens, called the focusing lens, is used at the second focal point of the PSIRA to better match the focused pulses into the (biological) target medium.



Analytical calculations, numerical simulations and experimental results on a five-layer, hemispherical, dielectric focusing lens are detailed. The second lens, called the launching lens, is used at the first focal point of the PSIRA. For input voltages of 100 kV or more, a switch system, i.e., switch cones, pressure vessel, hydrogen chamber and launching lens, are required to effectively launch a spherical TEM wave from the first focal point. Various switch configurations are explored. It is shown that the pressure vessel can also serve as the launching lens, which considerably simplifies the design of the switch system. Spherical and cylindrical pressure vessel designs are investigated.

The second is the Switched Oscillator (SwO) antenna. A SwO is essentially an electrical, shock-excited resonant structure. The SwO is adopted as a high-power antenna to radiate high-energy pulses in the terahertz frequency range. The primary focus is to use these pulses for secure communications. Analytical calculations for the SwO are detailed. Numerical simulations are used to optimize and more thoroughly study the antenna. Various characteristic relations obtained are used to provide a deeper insight into the working of the SwO radiator.

# Contents

<b>List of Figures</b>	<b>xiv</b>
<b>List of Tables</b>	<b>xxi</b>
<b>1 Introduction</b>	<b>1</b>
<b>2 The Prolate-Spheroidal Impulse-Radiating Antenna</b>	<b>4</b>
2.1 Prolate-Spheroidal reflector . . . . .	8
2.2 Focal waveform . . . . .	9
2.3 Optimization of the reflector dimensions . . . . .	9
<b>3 Design of the Focusing Lens</b>	<b>12</b>
3.1 Scaling Relationships . . . . .	15
3.1.1 Ideal Scaling Relationships at Focus . . . . .	18
3.2 Matching from Focus Medium to Target Medium . . . . .	20
3.3 Numerical Simulations . . . . .	23

*Contents*

3.3.1	Simulation Setup . . . . .	23
3.3.2	Electric and magnetic field responses at the focal point . . . . .	24
3.3.3	Comparison of spot size in air and inside lens . . . . .	26
<b>4</b>	<b>Experimental Measurements on a Five-Layer Focusing Lens</b>	<b>29</b>
4.1	Tiny Fast-Pulse D-Dot Sensor Design in Dielectric Media . . . . .	30
4.1.1	Practical Considerations . . . . .	33
4.1.2	Comments Concerning Calibration . . . . .	33
4.2	Experimental Setup . . . . .	34
4.2.1	D-dot sensor . . . . .	36
4.2.2	100 ps Filter . . . . .	36
4.3	Focal Waveform and Beam Width in Air . . . . .	38
4.3.1	Calibration of the D-dot Probe in Air . . . . .	38
4.3.2	Focal Impulse Waveform . . . . .	40
4.3.3	Beam width (Spot size) . . . . .	43
4.4	Focal Waveform and Beam Width in the Focusing Lens . . . . .	44
4.4.1	Calibration of the D-dot Probe in the Target Medium . . . . .	45
4.4.2	Focal impulse waveform . . . . .	50
4.4.3	The focusing lens as a bandpass filter . . . . .	54
4.4.4	Beam width (Spot size) . . . . .	55
4.5	Comparison of Measurements with and without the 100 ps Filter . . . . .	61

*Contents*

4.6	Accuracy of Measurements with D-dot Probe . . . . .	63
4.7	Summary . . . . .	64
<b>5</b>	<b>Switch System and Launching Lens Designs</b>	<b>66</b>
5.1	Initial Launching Lens Designs . . . . .	67
5.1.1	Uniform lens design . . . . .	68
5.1.2	Non-uniform lens design . . . . .	68
5.2	Investigation of Various Switch Configurations . . . . .	69
5.3	Pressure Vessel Designs . . . . .	73
5.3.1	T4FASC with a Spherical Pressure Vessel and Spherical Hydrogen Chamber (T4FASC-SPVSHC) . . . . .	73
5.3.2	T4FASC with a Cylindrical Pressure Vessel and Cylindrical Hydrogen Chamber (T4FASC-CPVCHC) . . . . .	77
5.4	Optimization of Switch System Components . . . . .	84
5.5	Comparison of electromagnetic parameters for the T4FASC-SPVSHC and T4FASC-CPVCHC configurations with the focusing lens . . . . .	85
5.6	Discussion . . . . .	88
<b>6</b>	<b>The Switched Oscillator as a THz Antenna</b>	<b>92</b>
6.1	Frequencies for Atmospheric Transmission . . . . .	94
6.2	Desired Properties of the Photoconductive Switch Material . . . . .	95
6.3	The Switched Oscillator as a Terahertz Radiator . . . . .	96

*Contents*

6.4	Maximizing Energy in Terahertz Pulse Radiation from a Switched Oscillator . . . . .	99
6.4.1	Maximizing the Stored Energy . . . . .	101
6.4.2	Ideal Radiation Characteristics . . . . .	104
6.4.3	Matching to Electric Dipoles . . . . .	110
6.4.4	Effect of Dielectrics . . . . .	113
6.4.5	Skin-Effect Losses . . . . .	114
6.4.6	Switch Losses . . . . .	114
6.5	Discussion . . . . .	116
<b>7</b>	<b>Parameter Study of the SwO Antenna</b>	<b>117</b>
7.1	Validation of CST MWS® . . . . .	118
7.1.1	Determination of the Input Waveform for the 5-10-5 MAX1 Antenna . . . . .	118
7.1.2	Results . . . . .	121
7.2	Determination of the Input Waveform for the SwO Antenna . . . . .	123
7.3	Simulation Setup . . . . .	124
7.4	Investigation of the Skin-Effect Losses in a Copper SwO Antenna Above a Copper Ground Plane . . . . .	125
7.5	$Q$ and $f_0$ as a function of $h$ . . . . .	126
7.6	$Q$ and $f_0$ as a function of $\epsilon_{rs}$ . . . . .	128

*Contents*

7.7	$Q$ and $f_0$ as a function of $l_s$ . . . . .	130
7.8	$Q$ and $f_0$ as a function of $w$ . . . . .	132
7.9	Summary . . . . .	134
7.10	Future Work . . . . .	136
<b>8</b>	<b>Conclusions</b>	<b>138</b>

# List of Figures

2.1	Concept of treatment of cancerous tissue inside the body. For imaging a second, identical IRA in a confocal arrangement could be used as receiver. . . . .	6
2.2	Side and front views of the prolate-spheroidal reflector. . . . .	8
2.3	Idealized electric field waveform at the second focal point. . . . .	9
3.1	Prolate-spheroidal impulse radiating antenna and lens system to focus and match into (biological) target medium [1]. . . . .	13
3.2	Lens concentrating an inward-propagating spherical pulse . . . . .	16
3.3	Simulation setup of system with a prolate-spheroidal reflector, four feed-arms at $60^\circ$ , the hemispherical 5-layer focusing lens and a slab ( $\epsilon_r = 9.0$ ). . . . .	24
3.4	Comparison of electric field focal waveforms, at second focal point, with and without focusing lens . . . . .	25
3.5	Comparison of magnetic field focal waveforms, at second focal point, with and without focusing lens . . . . .	25

*List of Figures*

3.6	Peak electric field as a function of distance, along the $x$ -axis, with and without focusing lens. The focal point is at $x = 0$ cm. . . . .	27
3.7	Peak magnetic field as a function of distance, along the $x$ -axis, with and without focusing lens. The focal point is at $x = 0$ cm. . . . .	27
4.1	Small D-Dot Sensors [2]. . . . .	32
4.2	Experiment setup of $60^\circ$ four feed arm PSIRA with focusing lens, target and D-dot probe. . . . .	35
4.3	Block diagram of the experimental setup. . . . .	35
4.4	D-dot probe to measure electric field inside target medium. . . . .	37
4.5	Comparison of pulser waveforms with and without filter. . . . .	38
4.6	Electric field focal waveform in air with 100 ps filter. . . . .	40
4.7	“Zoomed-in” view of electric field impulse at second focal point in air with 100 ps filter. . . . .	42
4.8	Beam width in air and Gaussian curve fit. . . . .	43
4.9	Comparison of spot size obtained from experiment and numerical simulation. . . . .	44
4.10	Slit cut in target medium/slab into which the handmade D-dot probe is inserted. . . . .	46
4.11	Setup to calibrate D-dot probe inside dielectric medium. . . . .	46
4.12	Schematic to calibrate D-dot probe. . . . .	48



*List of Figures*

4.13	Electric field measured by D-dot probe inside slab (top); “zoomed-in” prepulse used for calibrating D-dot probe inside target medium (bottom). . . . .	49
4.14	Electric field focal waveform in lens with 100 ps filter. . . . .	50
4.15	“Zoomed-in” view of electric field impulse at second focal point in lens with 100 ps filter. . . . .	52
4.16	Comparison of focal impulse waveforms, at the second focal point, in air and inside the lens, with the 100 ps filter. . . . .	53
4.17	Ratio of magnitude of Fourier transform of the focal impulse waveform from experiments. . . . .	54
4.18	Ratio of magnitude of Fourier transform of the focal impulse waveform, from simulations, for an input pulse with 100 ps rise time. The dotted gray line is 1.77, the electric enhancement obtained with the lens. . . . .	55
4.19	Comparison of experimental results of beam width in air and in lens. . . . .	56
4.20	Comparison of simulation and experiment results of beam width in air. . . . .	57
4.21	Comparison of simulation and experiment results of beam width in lens. . . . .	57
4.22	Comparison of experimental results of beam width in air and in lens. . . . .	59
4.23	Comparison of numerical simulation and experimental results of beam width in air. . . . .	59
4.24	Comparison of numerical simulation and experimental results of beam width in lens. . . . .	60

*List of Figures*

4.25	Method used to rescale the experimental focal impulse waveform in air [1]. . . . .	61
4.26	Comparison of the electric field focal impulse waveforms with and without the 100 ps filter. The analytical prepulse (-0.7 V) is plotted for reference. . . . .	62
4.27	Metal tape covering gap between probe edge and ground plane to reduce leaking of electric fields through the gap. . . . .	64
5.1	Schematic of launching lens and switch system. The feed point (switch center) and first focal point ( $-z_0$ ) are spatially isolated. [3].	67
5.2	Four feed arms with switch cones (4FASC) [4]. . . . .	70
5.3	Truncated four feed arms with switch cones (T4FASC) [4]. . . . .	70
5.4	Vertical Bicone Switch (VBCS) [5]. . . . .	71
5.5	Slanted Four-Cone Feed Arms (S4CFA) [4]. . . . .	72
5.6	Side view of the T4FASC configuration with a spherical pressure vessel and spherical hydrogen chamber. . . . .	74
5.7	Normalized $E_\theta$ and $E_\phi$ components of the responses from the electric field probes on the $xy$ , $-yz$ and $-zx$ planes for the T4FASC-SPV configuration. . . . .	75
5.8	Electric field focal impulse waveform for the T4FASC-SPV configuration. . . . .	76
5.9	Spot size for the T4FASC-SPV configuration. . . . .	76
5.10	Diagram for cylindrical pressure vessel and launching lens calculations.	78

*List of Figures*

5.11	Cylindrical pressure vessel showing the need for a cylindrical guiding structure on top of the switch cones. . . . .	81
5.12	Side view of the T4FASC configuration with a cylindrical pressure vessel and cylindrical hydrogen chamber. . . . .	82
5.13	Electric field focal impulse waveform for the T4FASC-CPV configuration. . . . .	83
5.14	Spot size for the T4FASC-CPV configuration. . . . .	83
6.1	Schematic diagram of THz generation using a photoconductive switch and an (dipole) antenna. . . . .	95
6.2	Schematic of a SwO mounted over a substrate. . . . .	97
6.3	Electric field response and its Fourier transform. . . . .	98
6.4	Electric field radiation patterns from SwO at the resonant frequency, 0.4 THz. . . . .	99
6.5	THz radiator. (a) Side view and (b) Front view. . . . .	100
6.6	Equivalent transmission-line model of antenna with switch. . . . .	115
7.1	Comparison of the analytical excitation published in [6] and the RSEE with a $t_{mr}$ of 0.5 ps. . . . .	119
7.2	Shape of radiated electric field and its Fourier transform. . . . .	120
7.3	Comparison of the normalized analytical and numerical simulations results for the electric field ( $E_y$ ). . . . .	122

*List of Figures*

7.4	Comparison of the normalized analytical and numerical simulations results for the electric field ( $E_y$ ) in the frequency domain (FFT of Fig. 7.3). . . . .	122
7.5	Logisitic input voltage waveform, with a $t_{mr}$ of 0.5 ps, for the SwO antenna. . . . .	123
7.6	Comparison of the quality factors as a function of the SwO height above the ground plane for PEC and copper. . . . .	126
7.7	Comparison of quality factors ( $Q$ ), as a function of the SwO height above the ground plane, with and without the polyethylene substrate medium. A function is fit to the results, with the substrate, to obtain an empirical relation between $Q$ and $h$ . . . . .	127
7.8	The resonant frequency, $f_0$ , as a function of the relative permittivity of the substrate medium, $\epsilon_{rs}$ . A function is fit to the results to obtain an empirical relation between $f_0$ and $\epsilon_{rs}$ . . . . .	129
7.9	The quality factor, $Q$ , as a function of the switch length, $l_s$ . A function is fit to the results to obtain an empirical relation between $Q$ and $l_s$ . . . . .	131
7.10	The resonant frequency, $f_0$ , as a function of the switch length, $l_s$ . A function is fit to the results to obtain an empirical relation between $f_0$ and $l_s$ . . . . .	131
7.11	The quality factor, $Q$ , as a function of the switch length, $w$ . A function is fit to the results to obtain an empirical relation between $Q$ and $w$ . . . . .	133

*List of Figures*

7.12	The resonant frequency, $f_0$ , as a function of the antenna width, $w$ . A function is fit to the results to obtain an empirical relation between $f_0$ and $w$ . . . . .	133
7.13	Comparison of the quality factor and the peak radiated power density (at $r = 1$ m) as a function of the antenna width. . . . .	134

# List of Tables

3.1	Analytical electromagnetic parameters at lens focus . . . . .	20
3.2	Example focal spot dimensions . . . . .	20
3.3	Total Parameter Enhancement Including Mismatch into Target . . .	22
3.4	Electric and magnetic field information, at the second focal point, in air and with the focusing lens from Fig. 3.4 and Fig. 3.5 . . . . .	26
3.5	Spot diameter of E and H field with and without the focusing lens from Fig. 3.6 and Fig. 3.7 . . . . .	28
4.1	Asymptotic Cone Angles . . . . .	33
4.2	Beam width of electric field in air and with focusing lens from Fig. 4.19 and Fig. 4.20 . . . . .	58
4.3	Beam width of electric field in air and with focusing lens from Fig. 4.23 and Fig. 4.24 . . . . .	60
4.4	Comparison of focal waveforms and beam widths with and without the 100 ps filter in the focusing lens . . . . .	63

*List of Tables*

5.1	Peak focal impulse amplitude and beam width for various switch configurations. . . . .	72
5.2	Dimensions of switch system components for the T4FASC-SPVSHC design. . . . .	74
5.3	Dimensions of switch system components for the T4FASC-CPVCHC design. . . . .	82
5.4	Comparison of the electric and magnetic field information, for the 4FA, T4FASC-CSS-SPVSHC, T4FASC-CSS-CPVCHC configurations, at focal point, in air and with focusing lens (FL) . . . . .	86
5.5	Comparison of spot size for E and H field, for the 4FA, T4FASC-CSS-SPVSHC, T4FASC-CSS-CPVCHC configurations, with and without the focusing lens (FL) . . . . .	87
5.6	Parameters expected from the PSIRA by ODU. . . . .	88
6.1	Attenuation of the Electromagnetic Waves at favorable frequencies .	94
6.2	Parameters of Cr-doped SI-GaAs. . . . .	96
7.1	Dimensions of a “reference” copper SwO above a copper ground plane with a (lossless) polyethylene substrate medium. . . . .	124
7.2	Summary of parametric study of the SwO. . . . .	135

# Chapter 1

## Introduction

*“Since figures and pictures strike the imagination of the reader much better, all dissertations should be published in cartoon form to reach a larger publicum.”*

The history of Electromagnetic Pulse (EMP) technology began in 1945 with the first nuclear event. Since the mid-1970's however, it has spawned some related areas which, in recent years, have come to be identified with High-Power Electromagnetics (HPE). Such areas include EMP simulators, transient (broad-band) electromagnetic sensors and techniques, high-power pulse radiators, transient radars, etc. [7]. This dissertation presents two EMP/HPE devices designed to address unique applications.

The first device is a reflector antenna called the Prolate-Spheroidal Impulse-Radiating Antenna (PSIRA). Such an antenna uses a prolate-spheroidal reflector to focus a fast ( $\leq 100$  ps), high-voltage ( $> 100$  kV) impulse onto a target located in the near field. It has been found that such pulses are useful for a variety of biological applications, such as accelerated wound healing and skin cancer (melanoma) treatment [8, 9]. The PSIRA has been extensively studied in [10]. In this dissertation the focus is on the design of two lenses for the PSIRA. The first lens, called the focusing lens, is used to better match the focused pulses into the biological target medium.



## *Chapter 1. Introduction*

Chapters 2-4 present the analytical, numerical and experimental results for such a lens. The second lens, called the launching lens, is used to aid in the launching of fast, high-voltage, spherical TEM pulses from the switch center. Chapter 5 details the design of the switch system and the launching lens. Indeed, one can consider Ch. 2-5 as a continuation of [10].

While the electromagnetics associated with the PSIRA is mostly in the time domain (broad-band), the second device, the Switched Oscillator (SwO), is concerned with the frequency domain (narrow-band) applications of an electromagnetic pulse. A SwO is essentially an electrical, shock-excited resonant structure (e.g., a transmission line). The SwO is adopted as a high-power antenna to radiate high-energy pulses in the terahertz frequency range. The primary aim is to use these pulses for secure communications. Chapters 6-7 present the analytical design and numerical optimizations of such a device.

BIOLOGICAL APPLICATION  
PSIRA

## Chapter 2

# The Prolate-Spheroidal Impulse-Radiating Antenna

*“No, no, you’re not thinking, you’re just being logical.”*

*- Niels Bohr*

The effect of high-intensity nanosecond electrical pulses on biological cells and tissue has received considerable attention by the scientific community, particularly in the past five years and has led to the establishment of a new research field: bioelectrics [11]. In the time domain below approximately 100 ns, the rise time of the pulse is faster than the charging time of the plasma membrane of most mammalian cells, meaning that the field will pass through the membrane into the cytoplasm. High-voltage pulses in the nanosecond range have been shown to penetrate into living cells to permeabilize intracellular organelles, and release  $\text{Ca}^{2+}$  from the endoplasmic reticulum. They provide a new approach for physically targeting intracellular organelles with many applications including activation of platelets and release of growth factors for accelerated wound healing [9] and precise control of programmed cell death (apoptosis) which has been shown to cause complete elimination of melanoma tumors

[8]. The pulses were in this case delivered by needle-electrodes to the tumors.

The bioelectric effects of ultrashort, square wave pulses were shown to follow the scaling law [12]

$$S = S(E\tau N^{1/2}), \quad (2.1)$$

with  $S$  being a quantity which describes the intensity of the observable bioelectric effect,  $E$  the electric field amplitude,  $\tau$  the pulse duration and  $N$  the number of pulses. This law, which was shown to hold for nanosecond pulses, indicates that for picosecond (ps) pulses to achieve similar effects the electric field will need to be much higher than for nanosecond pulses. However, there are two reasons to enter the ps-pulsed electric field range. The first one is that for extremely short pulses, the permittivity of the various cell components, rather than their resistivity, determines the electric field distribution in the cell [13]. The electric field then acts directly on membrane proteins, rather than causing charging of the membrane, and, if sufficiently strong, can cause direct and instant conformational changes. Subnanosecond pulses (200 ps) were found to alter the cell membrane conductance and unrectifying channels are formed when cells are exposed to electric field strengths on the order of 20 kV/cm [14] for 2000 pulses. The disruption of the membrane integrity may lead to the change of physiological conditions of the cell and cause cell death.

Second, besides providing the opportunity to explore a new field of electric field-cell interactions, subnanosecond pulses will ultimately allow medical applications for delivery of pulsed electric fields without invasive electrodes, using antennas instead. A possible configuration that allows us to generate very high electric fields uses a focusing antenna [15, 16] and may be able to induce apoptosis in tissue without using needles as the delivery system for electric pulses, Fig. 2.1. Lenses used in combination with the reflector of such an antenna allow one to achieve a higher spatial resolution [1, 17].

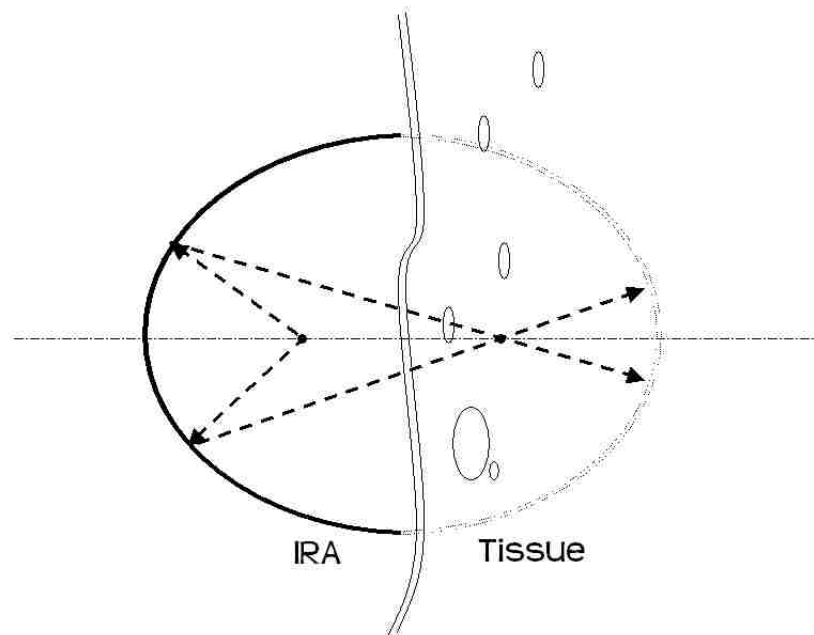


Figure 2.1: Concept of treatment of cancerous tissue inside the body. For imaging a second, identical IRA in a confocal arrangement could be used as receiver.

Besides using ultrashort (10 ns) electrical pulses for medical therapies [18], the pulsed radiation may lead to medical imaging methods. Imaging is based on the measurement of changes in the complex permittivity of tissue, and may complement other methods based on the measurement of other physical parameters, such as X-Ray Computed Tomography (CT), magnetic resonance imaging (MRI) and ultrasound. Generally, the resolution is limited by the diffraction time, which restricts the detectable target size to larger than the pulse width. For example, a spatial resolution in the centimeter range is expected if the pulse is near 100 ps. In such an imaging system, the electromagnetic waves are focused on a target inside the body. The scattered signal contains information on the dielectric properties and the geometry of the target and allows its identification through an inverse scattering method. 3D scanning allows us to obtain the dielectric profile of the tissue and to detect any abnormality in a uniform background.

Research on the use of impulse radiating antennas for medical applications re-

quires, in addition to the development of focusing antennas, research on the biological effect of subnanosecond pulses. Experimental studies with 800 ps long pulses with electric field amplitudes of up to 1 MV/cm applied to melanoma (B16) cells have provided information on the pulse parameters required to induce cell death [13]. Studies with 200 ps long pulses are underway. First results indicate that cell death requires a large number of pulses ( $> 10^6$ ) at moderate electric field intensities of 20 kV/cm [14]. However, synergistic effects such as caused by local tissue heating might allow us to reduce the pulse number considerably, and to establish impulse radiating antennas as a new tool in treatment of cancer.

The Impulse Radiating Antenna (IRA) is a focused aperture hyperband<sup>1</sup> antenna suited for radiating very fast, high-voltage ( $> 100$  kV) pulses in a narrow beam [21]. A fast-rising step-like input into the antenna gives an approximate delta-function response. IRAs thus provide an attractive means to deliver electric pulses to induce apoptosis in tissue cells without using needles.

This dissertation presents the design and experimentation on a Prolate-Spheroidal reflector IRA (PSIRA) and focusing lens system. Numerical simulation and experimental results for the focusing lens are detailed. The design of a switch system to launch high-voltage ( $\geq 100$  kV) spherical TEM pulses for such an antenna is described. The treatment of skin cancer (melanoma) is used as an illustrative example. As mentioned above, currently, needle arrays are used for treating melanoma tumors. This approach is invasive and often results in discomfort to the patient. The PSIRA has the advantage of non-invasively delivering the required pulsed electric fields to melanoma tissues. By directly focusing on the target cells it reduces damage to the tissue layers surrounding the target and skin.

---

<sup>1</sup>The term hyperband refers to a band ratio (not band width) greater than one decade [19]. It is a well established IEC standard (61000-2-13) [20].

## 2.1 Prolate-Spheroidal reflector

IRAs are composed of two main parts, a conical TEM transmission line, called the feed arms, and a focusing optic which is usually a reflector or a lens. Paraboloidal reflector IRAs, where the radiated impulse is focused at infinity, are by far the most common as they have been used in a variety of applications such as transient radars, buried target identification, etc. However, for use in the biological application described above, where electric fields need to be focused onto a target in the near field, a prolate-spheroidal reflector must be used [15, 22].

The front and side views of a four feed-arm Prolate-Spheroidal IRA (PSIRA) are shown in Fig. 2.2. The feed-arms are oriented at  $60^\circ$  as this amplifies the field intensity by a factor of 1.606 compared to the two-arm configuration [10]. The dimensions of the feed arms are determined by their  $200 \Omega$  pulse impedances.

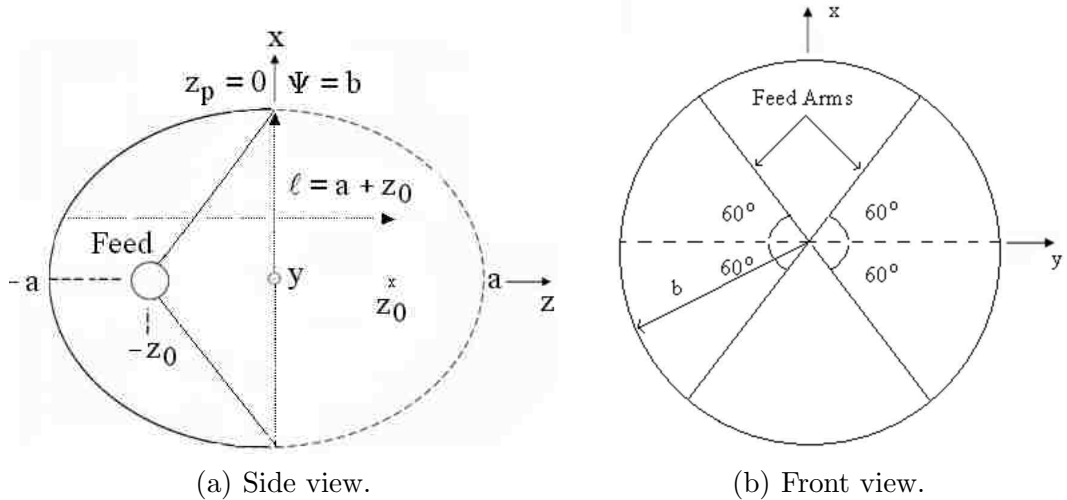


Figure 2.2: Side and front views of the prolate-spheroidal reflector. .

The PSIRA system has two foci. An inhomogeneous spherical TEM wave launched on guiding conical conductors from one focus ( $-z_0$ ) is converted, by a double stereographic transformation, to a second (reflected) inhomogeneous spherical TEM wave propagating toward the second focus ( $z_0$ ) [23].

## 2.2 Focal waveform

For an ideal step input, the electric field waveform at the second focal point is shown in Fig. 2.3. The waveform has three main parts: the pre-pulse, the impulse, and the post-pulse. The pre-pulse is the direct radiation from the feed. It has a low magnitude and lasts for a long duration. The impulse is due to the fields from the reflector converging at the focal point. It lasts for a short time and has a large amplitude. The post-pulse is mostly due to diffraction effects and the fields outside the aperture. The pre-pulse and impulse dominate the early-time (high frequency) behavior of the IRAs while the post-pulse provides information on the late-time (low frequency) behavior. The prolate-spheroidal reflector differentiates the input; the derivative of the step input thus results in the impulsive part of the waveform. It is the impulse that induces electroporation or apoptosis in the cells and therefore must be maximized.

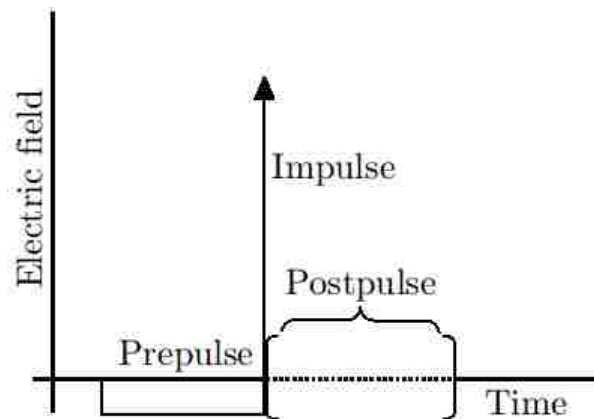


Figure 2.3: Idealized electric field waveform at the second focal point.

## 2.3 Optimization of the reflector dimensions

The pre-pulse reduces the amplitude of the impulse. It is therefore desirable to have as small a pre-pulse as possible. The magnitude of the pre-pulse is solely determined



by the size of the reflector [22, 23]. The reflector geometry and position of the truncation plane,  $z_p$ , are optimized to obtain an acceptable compromise between the physical dimensions of the reflector and the pre-pulse amplitude.

After investigation of various electromagnetic parameters, the following dimensions were found to be most suitable [15, 22],

$$z_p = 0, \quad a = 0.625 \text{ m}, \quad b = \Psi = 0.5 \text{ m}, \quad z_0 = 0.375 \text{ m}, \quad l = 1 \text{ m}, \quad (2.2)$$

where,

$z_p = z$  – coordinate of the truncation plane,

$a, b$  = radii of the prolate-spheroid,

$z_0 = (a^2 - b^2)^{1/2}$  = focal distance,

$l = a + z_0$  = distance used for normalization,

$\Psi$  = radial coordinate,

as shown in Fig. 2.2(a). For the values in (2.2), the reflector can be easily fabricated. Also, the symmetry of the geometry greatly simplifies the problem.

A pulse width of 100 ps is used to validate the applicability of the PSIRA to deliver pulses in the picosecond regime. A 100 ps pulse duration leads to a reflector with practically acceptable dimensions. For pulses less than 100 ps, the reflector can be made smaller. For pulse widths greater than 100 ps, a larger system is required. However, using the PSIRA system for pulses with durations much greater than 100 ps, e.g.  $> 500$  ps, is not recommended, as the size of the system may not be very practical. The reflector dimensions in (2.2) were optimized for a 100 ps ramp rising input.

CST Microwave Studio®<sup>2</sup>, a three dimensional, finite integral time domain (FITD), commercially available software, was used for all the PSIRA simulations in this

---

<sup>2</sup><http://cst.com/>

*Chapter 2. The Prolate-Spheroidal Impulse-Radiating Antenna*

dissertation. A 1V, 100 ps ramp rising step input and a frequency range of 0-10 GHz was used in all simulations.

# Chapter 3

## Design of the Focusing Lens

*“Any sufficiently analyzed magic is indistinguishable from science”*

*- Agatha Heterodyne/Cinderella*

The previous chapter considered the design of a prolate-spheroidal reflector for concentrating a pulse, in the near field, from one of the foci onto a target at the second focus. The idea is to get a very fast, very intense electromagnetic pulse to illuminate the target (e.g., a tumor). By very fast we mean fast enough to get the spot diameter (beam width) at the focus down to the target size, or as close to this as technology allows. At the same time a small spot size also implies large fields [24].

One problem with placing fields on the target concerns the dielectric properties of the target medium and its surroundings. If the wave incident on the target is in air, but the target medium has a large relative permittivity (say about 81 for water), then there will be a significant reflection of the pulse, leading to a smaller field in the target medium [24]. This chapter discusses the addition of a lens, called the focusing lens, to better match the wave to the target, and to reduce spot size, thereby increasing the field on the target. A schematic of the PSIRA and focusing lens system is shown in Fig. 3.1.

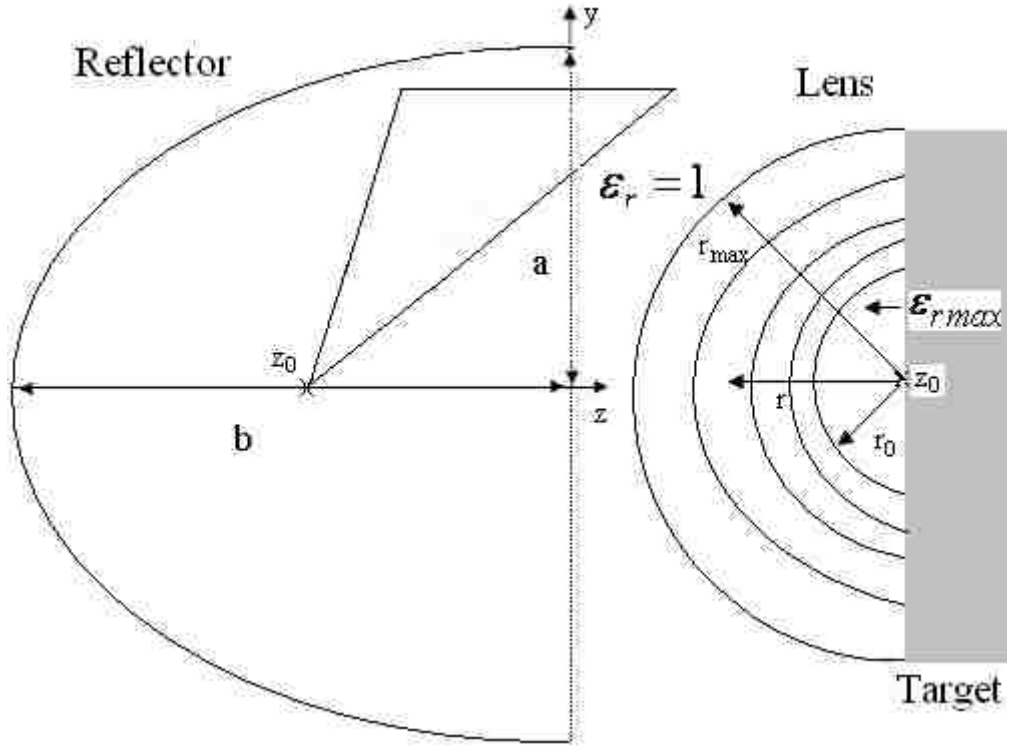


Figure 3.1: Prolate-spheroidal impulse radiating antenna and lens system to focus and match into (biological) target medium [1].

The PSIRA and lens system can deliver hundred-picosecond electric field pulses with a spatial resolution in the millimeter range. While our experiments, described in the next chapter, use 10 V, 45 ps rising signals, the design is for 100 kV or greater to achieve the desired field strengths with 100 ps rising pulses.

Only a brief summary of the design and analytical formulations of a spatially limited, graded focusing lens, as discussed in [17], are provided in this chapter. The electromagnetic techniques in [17] are an extension of the original work in [25]. The design of the lens consists of two parts. The first, is determination of the minimum dimension of the lens. This is accomplished by minimizing the pulse droop in an equivalent transmission line model with an exponentially tapered impedance profile. The second, is determination of the optimum number of layers of the lens. This is calculated by considering the transmission coefficient of an equivalent transmission

line model.

An exponentially tapered lens has a minimized droop and optimal transfer for the case of uniform propagation speed [26]. When adapted to the dielectric focusing lens under consideration, a 1D wave equation is obtained in a transformed coordinate  $\zeta$ . In the  $\zeta$  coordinate system, the wave propagates with a constant velocity and has an exponential wave impedance variation through the lens. A solution to the transmission line equations in [26] yields the transit, normalized and droop time parameters as [17],

$$\begin{aligned} t_{\zeta_{\max}} &\equiv \zeta_{\max}/c, & \text{transit time through lens,} \\ \tau &\equiv t/t_{\zeta}, & \text{normalized time,} \\ \tau_d = 2 \ln^{-2}(g) = t_d/t_{\zeta_{\max}}, & & \text{normalized droop time,} \end{aligned} \quad (3.1)$$

where  $t_d$  is the droop time and  $g$  is the high frequency gain defined in [26] as

$$g = e^G = \sqrt{Z_2/Z_1} = \epsilon_r^{-1/4}. \quad (3.2)$$

Note that a plane wave approximation is used in this analysis. For a given dielectric target permittivity,  $\epsilon_{r_{\max}}$ , droop time and gain, the maximum dimension of the lens,  $z_{\max}$ , is [17]

$$z_{\max} = \frac{ct_d \ln^2(g)}{\ln(\epsilon_{r_{\max}})} [1 - \epsilon_{r_{\max}}] \text{ meters.} \quad (3.3)$$

As an example, for  $\epsilon_{r_{\max}} = 81$  (water, a typical biological target medium) and  $t_d = 1$  ns,  $z_{\max} = 7.3$  cm.

The hemispherical focusing lens is designed such that  $r/\lambda$  is not a function of  $r$ , i.e.,

$$\begin{aligned} \epsilon_r(r) &= (r_{\max}/r)^2 & r \geq r_0, \\ \epsilon_{r_{\max}} &\equiv (r_{\max}/r_0)^2 & r \leq r_0, \end{aligned} \quad (3.4)$$

where  $r$  is the radius of the lens and  $r_0$  is a constant center radius. For a given  $\epsilon_{r_{\max}}$ ,  $r_0$  is

$$r_0 = \frac{\nu c \Delta t}{\epsilon_{r_{\max}}^{1/2}}, \quad (3.5)$$

where  $\nu$  is the number of pulse widths in a dielectric sphere of constant radius  $r$  [27]. A value of  $\nu = 5$  was chosen for the construction of the focusing lens; based on loss and dispersion considerations [17]. For  $\nu = 5$ ,  $N = 5$  layers, and  $\epsilon_{r_{\max}} = 9.0$  the radius of the lens is  $r_{\max} = 15.0$  cm.

For a graded,  $N$  layer focusing lens, the ratio of the dielectric constants between subsequent layers is constrained to be the same, i.e.,

$$\epsilon_{\text{ratio}} = \epsilon_{r_{n+1}} / \epsilon_{r_n}. \quad (3.6)$$

The above equation implies that all layers have the same electrical width [1].

The total transmission coefficient for an  $N$  layer, graded dielectric lens is [17]

$$T_{\text{total}} = \left( \frac{2 \left( \epsilon_{r_{\max}}^{1/N} \right)^{-1/2}}{1 + \left( \epsilon_{r_{\max}}^{1/N} \right)^{-1/2}} \right)^N. \quad (3.7)$$

The above approximate formula is valid for a large number of wavelengths or pulse widths,  $\nu$ , across the beam. Based on numerical simulations,  $5 < \nu < 8$  was determined in [17]. Not much amplification is obtained for  $\nu > 10$ .

### 3.1 Scaling Relationships

Figure 3.2 shows the lens geometry, An incoming spherical electromagnetic pulse is incident on the lens at the outer radius  $r_{\max}$ . It propagates through a smoothly varying  $\epsilon_r(r)$  beginning at  $\epsilon_r(r_{\max}) = 1$  to a larger  $\epsilon_r(r_{\min}) = \epsilon_{r_{\max}}$ . The wave is

assumed short enough in time  $t_\delta$  (rise time) so that the droop in the pulse  $t_d$  is [3]

$$0 < t_\delta \ll t_d, \quad (3.8)$$

and can be neglected. In addition, it is assumed that the steps in  $\epsilon_r(r)$  as  $r$  is decreased are small enough that a set of spherical layers has enough layers to approximate the continuous case [3].

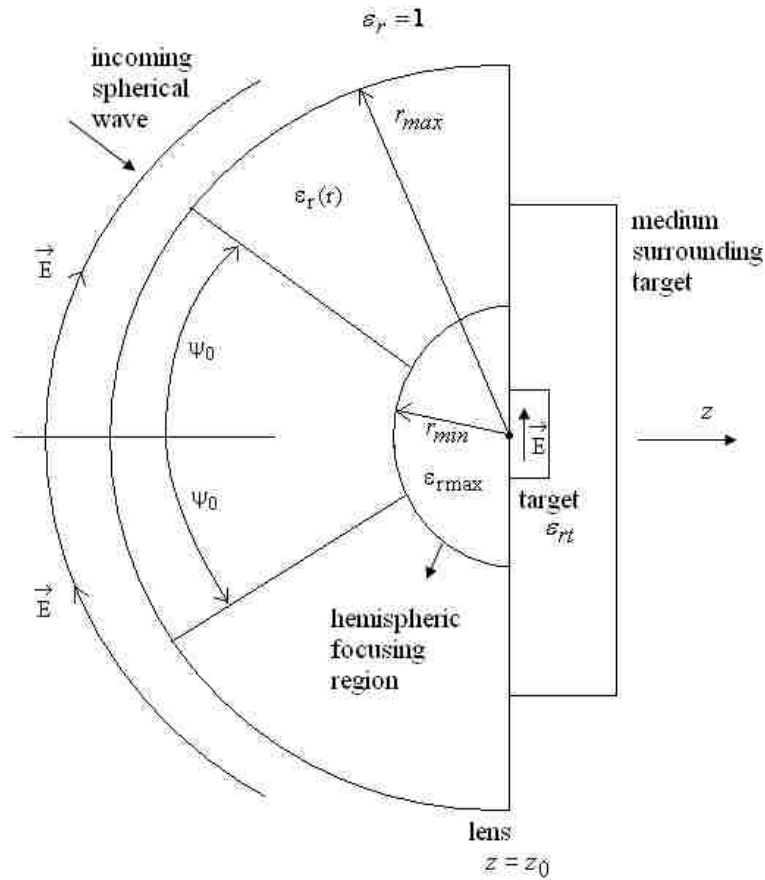


Figure 3.2: Lens concentrating an inward-propagating spherical pulse

A fundamental approximation concerns the number of spatial pulse widths in the dielectric along a sphere of constant radius  $r$ . As in Fig. 3.2, let the significant portion of the incident wave be concentrated on a circular cone of angle  $\Psi_0$  from the axis. In this region we need many pulse widths (like wavelengths if we are dealing with single frequency) extending over this domain of angular diameter  $2\Psi_0$ . In this

Chapter 3. Design of the Focusing Lens

case we can calculate the wave propagation into smaller  $r$  as though it were a plane wave. Another way to look at this is as power conservation as the wave enters a smaller and smaller cross section (diameter  $\equiv 2r\Psi_0$ ) or area  $\equiv \pi(r\Psi_0)^2$ . We are, of course, assuming negligible loss and dispersion in the dielectric for these calculations to apply.

The functional form of  $\epsilon_r$  is,

$$\epsilon_r = \frac{r_{\max}}{r}, \quad r_{\min} \leq r \leq r_{\max}, \quad (3.9)$$

$$\epsilon_{r_{\max}} = \frac{r_{\max}}{r_{\min}}, \quad 0 \leq r \leq r_{\min}, \quad (3.10)$$

in its continuous form. On leaving  $r_{\max}$  into the focusing region the pulse goes into a minimum spot size which we can estimate from [3]. The radius before inserting the lens is

$$\Delta\Psi_0 = \frac{a}{2b}ct_\Psi = \frac{a}{b}ct_\delta, \quad (3.11)$$

where  $a$  and  $b$  are the radii of the prolate-spheroid ( $a < b$ ),  $c$  is the speed of light in free space, and  $t_\Psi$  is the pulse width with respect to  $\Psi$ . For reference we can have an example [22],

$$\begin{aligned} \frac{a}{b} &= \frac{5}{4} = 1.25, \\ t_\delta &= 100 \text{ ps}, \quad t_\Psi = 2t_\delta = 200 \text{ ps}, \\ \Delta\Psi_0 &= 3.75 \text{ cm}. \end{aligned} \quad (3.12)$$

We have a scaling parameter as  $\epsilon_{r_{\max}}^{-1/2}$  for the spot size. Note that at a given  $r$  the number of pulse widths is given by

$$\frac{\nu}{\nu_0} \cong r\epsilon_r(r)^{-1/2} \cong 1, \quad (3.13)$$

where  $\nu_0 \equiv$  number of pulse widths at  $r_{\max}$ .



### 3.1.1 Ideal Scaling Relationships at Focus

We can now give several scaling relationships for the various electromagnetic parameters in summary form.

#### 3.1.1.1 Spot Radius

$$\frac{\Delta\Psi(\text{min})}{\Delta\Psi(\text{no lens})} = \frac{r_{\text{min}}}{r_{\text{max}}} = \epsilon_{r_{\text{max}}}^{-1/2} \quad (3.14)$$

#### 3.1.1.2 Spot Area

$$\frac{A(r_{\text{min}})}{A(\text{no lens})} = \left(\frac{r_{\text{min}}}{r_{\text{max}}}\right)^2 = \epsilon_{r_{\text{max}}}^{-1} \quad (3.15)$$

#### 3.1.1.3 Power density in spot

$$\frac{P(r_{\text{min}})}{P(r_{\text{max}})} = \frac{A(r_{\text{min}})}{A(r_{\text{max}})} = \epsilon_{r_{\text{max}}} \quad (3.16)$$

$$\begin{aligned} -\vec{1}_r \times \vec{E}(r) &= Z_w \vec{H}(r) \\ E(r) &= \sqrt{\frac{\mu}{\epsilon(r)}} H(r) = \epsilon(r)^{-1/2} Z_0 H(r) \\ P(r) &= -\vec{1}_r \cdot (\vec{E}(r) \times \vec{h}(r)) \\ &= E(r) H(r) = \epsilon(r)^{-1/2} Z_0 H(r)^2 \\ &= \frac{\epsilon(r)^{1/2}}{Z_0} E(r)^2 \end{aligned}$$

$$\frac{P(r_{\text{min}})}{P(r_{\text{max}})} = \epsilon_{r_{\text{max}}}^{1/2} \frac{E(r_{\text{min}})^2}{E(r_{\text{max}})^2} = \epsilon_{r_{\text{max}}}^{-1/2} \frac{H(r_{\text{min}})^2}{H(r_{\text{max}})^2} \quad (3.17)$$

**3.1.1.4 Electric field enhancement**

$$\frac{E(r_{\min})}{E(r_{\max})} = \epsilon_{r_{\max}}^{1/4} \quad (3.18)$$

**3.1.1.5 Displacement (electric flux density) enhancement**

$$\frac{D(r_{\min})}{D(r_{\max})} = \epsilon_r \frac{E(r_{\min})}{E(r_{\max})} = \epsilon_{r_{\max}}^{5/4} \quad (3.19)$$

**3.1.1.6 Magnetic field enhancement**

$$\frac{H(r_{\min})}{H(r_{\max})} = \epsilon_{r_{\max}}^{3/4} \quad (3.20)$$

**3.1.1.7 Magnetic flux density enhancement**

$$\frac{B(r_{\min})}{B(r_{\max})} = \epsilon_{r_{\max}}^{3/4} \quad (3.21)$$

**3.1.1.8 Some implications**

What we can see here is the great increase in the displacement associated with  $\epsilon_r$ . The time derivative of this is a current density inside the lens and the tissue. So the incident wave gives the electromagnetic parameters at the focus and they are presented in table 3.1.

Chapter 3. Design of the Focusing Lens

Table 3.1: Analytical electromagnetic parameters at lens focus

$\epsilon_r$	9.0	81.0
electric enhancement	1.73	3.0
displacement enhancement	15.6	243.0
magnetic enhancement	5.2	27.0
relative wave impedance	1/3	1/9
relative spot size at focus	1/3	1/9
relative spot area at focus	1/9	1/81

For  $\Delta\Psi_0 = 3.75$  cm,

Table 3.2: Example focal spot dimensions

$\epsilon_r$	1.0	9.0	81.0
$\Delta\Psi$ (spot radius) (cm)	3.75	1.25	0.42
$\pi\Delta\Psi^2$ (spot area) (cm <sup>2</sup> )	44.2	4.9	0.55

## 3.2 Matching from Focus Medium to Target Medium

As discussed in [28], as the waves go from the focus region to the target there may be a discontinuity in  $\epsilon_r$ . There is a transmission coefficient which expresses the change of the fields (up or down) in crossing this boundary. We estimate this based on

plane-wave formulae. If

$$\epsilon_{r_{\max}} = \epsilon_{rt} \quad (3.22)$$

where  $\epsilon_{rt}$  is relative permittivity of the target medium, then, the results in the previous section can be directly applied.

The electric field transmission coefficient is

$$T_{et} = \frac{2\epsilon_{rt}^{-1/2}}{\epsilon_{rt}^{-1/2} + \epsilon_{r_{\max}}^{-1/2}} = \frac{2}{1 + \left(\frac{\epsilon_{rt}}{\epsilon_{r_{\max}}}\right)^{1/2}}. \quad (3.23)$$

The displacement current density is then

$$T_{dt} = \frac{\epsilon_{rt}}{\epsilon_{r_{\max}}} T_{et} = \frac{\epsilon_{rt}}{\epsilon_{r_{\max}}} \frac{2}{1 + \left(\frac{\epsilon_{rt}}{\epsilon_{r_{\max}}}\right)^{1/2}}. \quad (3.24)$$

The magnetic transmission is

$$\begin{aligned} T_{ht} = T_{bt} &= \frac{Z_{wt}}{Z_{w\max}} T_{et} = \sqrt{\frac{\epsilon_{r_{\max}}}{\epsilon_{rt}}} T_{et} \\ &= \sqrt{\frac{\epsilon_{r_{\max}}}{\epsilon_{rt}}} \frac{2}{1 + \left(\frac{\epsilon_{rt}}{\epsilon_{r_{\max}}}\right)^{1/2}}. \end{aligned} \quad (3.25)$$

Combining these factors gives Table 3.3. As we can see, there is a large increase in the displacement current density.

The graded lens design assumes that the biological target is placed in direct contact with the last layer. Some preliminary considerations regarding the problems and design options for focusing more deeply buried targets are presented in [29]. The focal spot size will be affected if the lens is used on an uneven surface as the rays arrive at the focal point at different times. For such uneven surfaces, more innovative techniques for using the lens are currently being explored.

Table 3.3: Total Parameter Enhancement Including Mismatch into Target

$\epsilon_{rt}$ (target)	40.5		81		
$\epsilon_{\text{rmax}}$ (lens)	9	81	9	81	
$\frac{E(r_{\text{min}})}{E(r_{\text{max}})}$	1.73	3	1.73	3	in focal region
$\frac{D(r_{\text{min}})}{D(r_{\text{max}})}$	15.6	243	15.6	243	of lens
$\frac{H(r_{\text{min}})}{H(r_{\text{max}})} = \frac{B(r_{\text{min}})}{B(r_{\text{max}})}$	5.2	27	5.2	27	
$T_{et}$	0.32	1.17	0.5	1	transmission to
$T_{dt}$	1.44	0.59	4.5	1	target medium
$T_{ht}$	1.36	0.83	1.5	1	
$\frac{E_t}{E(r_{\text{max}})}$	0.55	3.51	0.87	3	in target
$\frac{D_t}{D(r_{\text{max}})}$	22.5	143	70	243	medium
$\frac{H_t}{H(r_{\text{max}})} = \frac{B_t}{B(r_{\text{max}})}$	7.1	22.4	7.8	27	

### 3.3 Numerical Simulations

The scaling relationships presented above are based on a simple model with a step rising input, i.e., the input has 0 rise time. The model does not take into account the sphericity of the hemispherical focusing lens and the number of feed arms. In our experiments, the 60° four feed arm configuration is used due to the higher electric fields obtained at the focus, compared to the two arm and 45° four arm cases [30, 31]. The scaling relationships in Sec. 3.1 and Sec. 3.2 provide insight into the scaling of fields at the focal point but are not applicable for distances away from the focal point. Also, results in the previous section do not provide information on the beam width (spot size). Numerical simulations with less assumptions, which take into account the complete problem, are required to provide more realistic and accurate results. CST Microwave Studio®<sup>®</sup>, a three dimensional, finite integral time domain (FITD), commercially available software, was used for our simulations.

#### 3.3.1 Simulation Setup

The simulation setup is shown in Fig. 3.3. It consists of a prolate-spheroidal reflector and four feed-arms at 60°. The hemispherical 5-layer focusing lens has its center at the second focal point. The radii and relative dielectric constants of the layers were obtained from [17] for  $\nu = 5$ . The dielectric slab,  $\epsilon_r = 9$ , in front of the focusing lens is used as a target medium to impedance match the spherical wave converging at the second focal point in the lens. The slab is included to replicate the experimental setup used to make measurements. The reflector and feed arms are assumed to be perfect electric conductors (PECs); the focusing lens and slab (dielectric media) are assumed to be lossless and dispersionless. A differential input of 1 V is applied between a 1 cm gap in the feed arms. The input is a ramp rising step with a 100 ps rise time. The setup to obtain electric and magnetic field spot sizes in air is identical

to Fig. 3.3, but without the focusing lens and the slab.

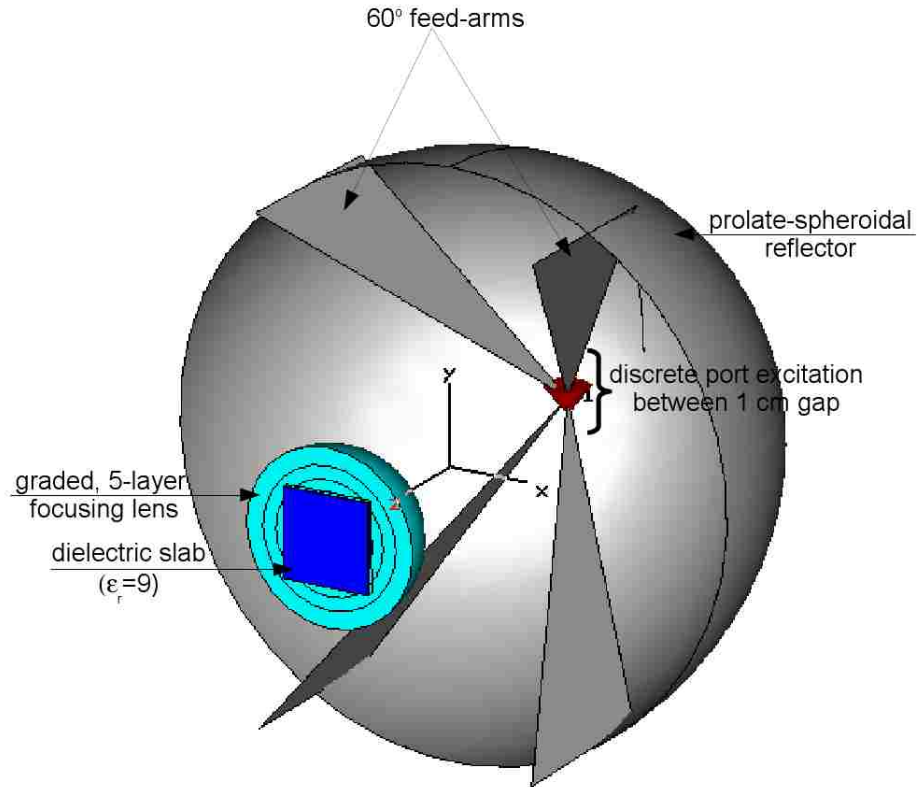


Figure 3.3: Simulation setup of system with a prolate-spheroidal reflector, four feed-arms at  $60^\circ$ , the hemispherical 5-layer focusing lens and a slab ( $\epsilon_r = 9.0$ ).

### 3.3.2 Electric and magnetic field responses at the focal point

The pre-pulse, impulse and post-pulse responses at the second focal point, for the electric and magnetic fields in air and with the lens, are shown in Fig. 3.4 and Fig. 3.5. One notes that the prepulse is dispersed due to the focusing lens.

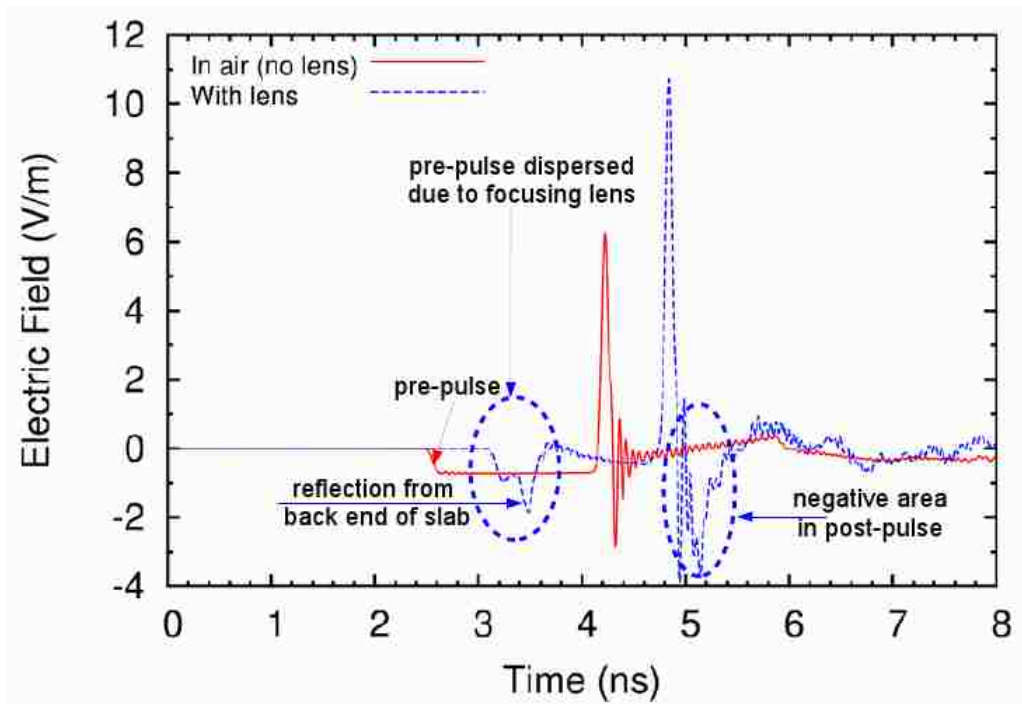


Figure 3.4: Comparison of electric field focal waveforms, at second focal point, with and without focusing lens

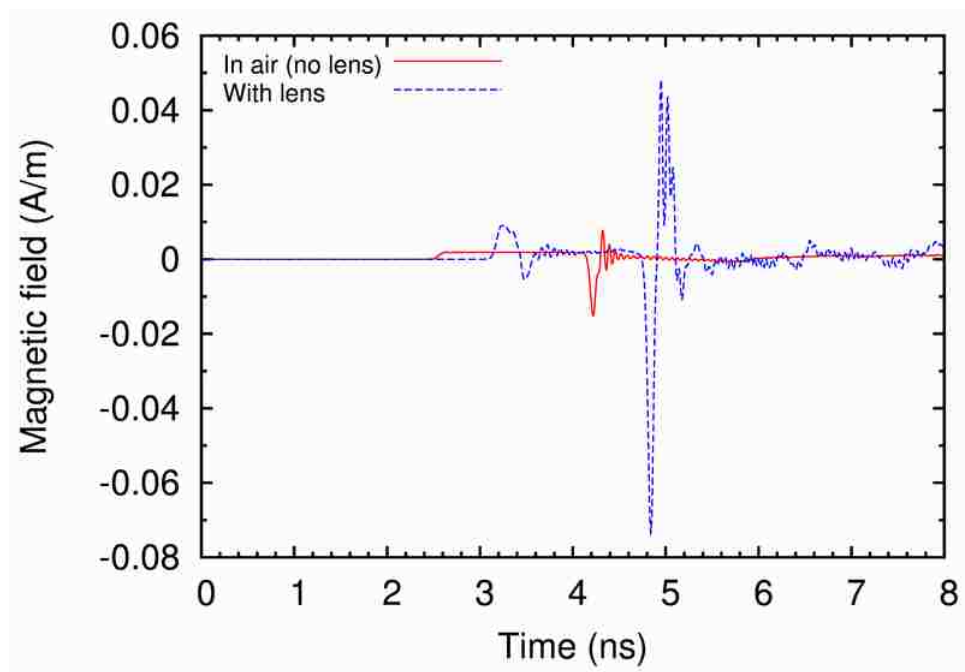


Figure 3.5: Comparison of magnetic field focal waveforms, at second focal point, with and without focusing lens



Important observations from the figures are summarized in Table. 3.4. As expected from Sec. 3.1.1, the electric enhancement is approximately  $1.717 \approx \epsilon_{r_{\max}}^{1/4} = 9.0^{1/4}$  and the magnetic enhancement is  $4.85 \approx \epsilon_{r_{\max}}^{3/4} = 9.0^{3/4}$ . The impedance in air,  $Z_{\text{air}} = 412.836 \Omega$ , is in good agreement with the  $408 \Omega$  obtained from previous experiments [10]. The impedance inside the lens is reduced to  $Z_{\text{lens}} = 146.139 \Omega$ .

Table 3.4: Electric and magnetic field information, at the second focal point, in air and with the focusing lens from Fig. 3.4 and Fig. 3.5

Parameter	Value
Peak electric field without lens	$E_{\max}^{\text{NL}} = 6.247 \text{ (V/m)}$
Peak magnetic field without lens	$H_{\max}^{\text{NL}} = 0.0151 \text{ (A/m)}$
Peak electric field with lens	$E_{\max}^{\text{WL}} = 10.725 \text{ (V/m)}$
Peak magnetic field with lens	$H_{\max}^{\text{WL}} = 0.0734 \text{ (A/m)}$
Relative impedance without lens	$Z_{\text{NL}} = E_{\max}^{\text{NL}}/H_{\max}^{\text{NL}} = 412.836 \Omega$
Relative impedance with lens	$Z_{\text{WL}} = E_{\max}^{\text{WL}}/H_{\max}^{\text{WL}} = 146.139 \Omega$
Electric enhancement	$E_{\max}^{\text{WL}}/E_{\max}^{\text{NL}} = 1.717$
Magnetic enhancement	$H_{\max}^{\text{WL}}/H_{\max}^{\text{NL}} = 4.850$

### 3.3.3 Comparison of spot size in air and inside lens

Figure 3.6 and Fig. 3.7 compare the peak electric and magnetic fields, in air and with the lens, as a function of distance along the  $x$ -axis (see Fig. 3.3 for the coordinate system). The focal point is at  $x = 0$  cm. The spot diameter is calculated as the half-power width of the curves.

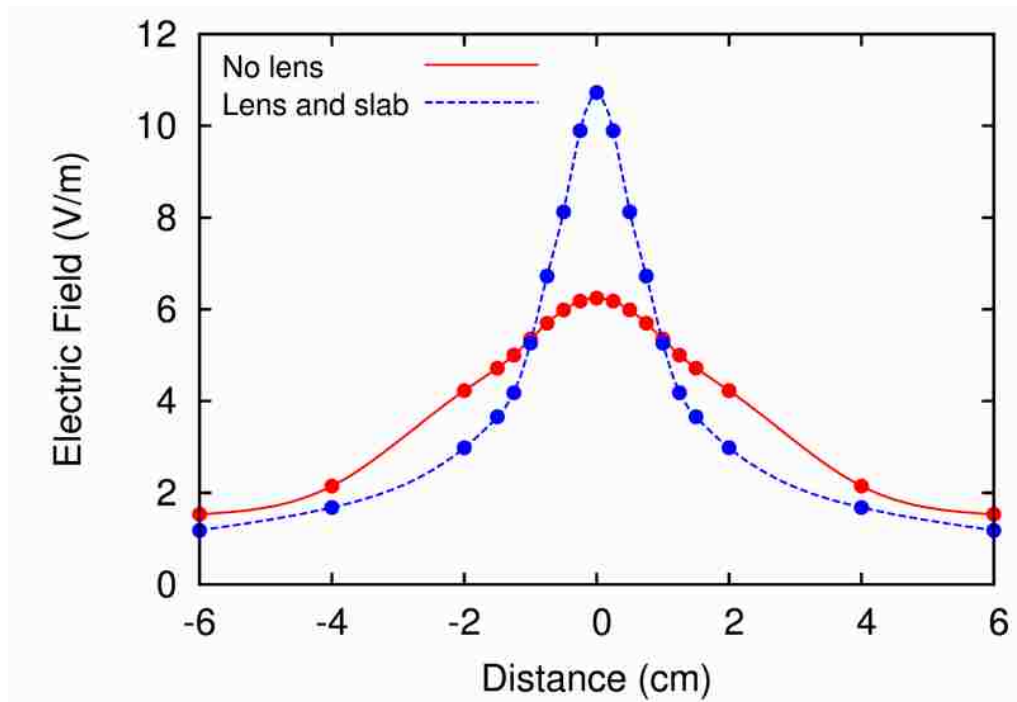


Figure 3.6: Peak electric field as a function of distance, along the  $x$ -axis, with and without focusing lens. The focal point is at  $x = 0$  cm.

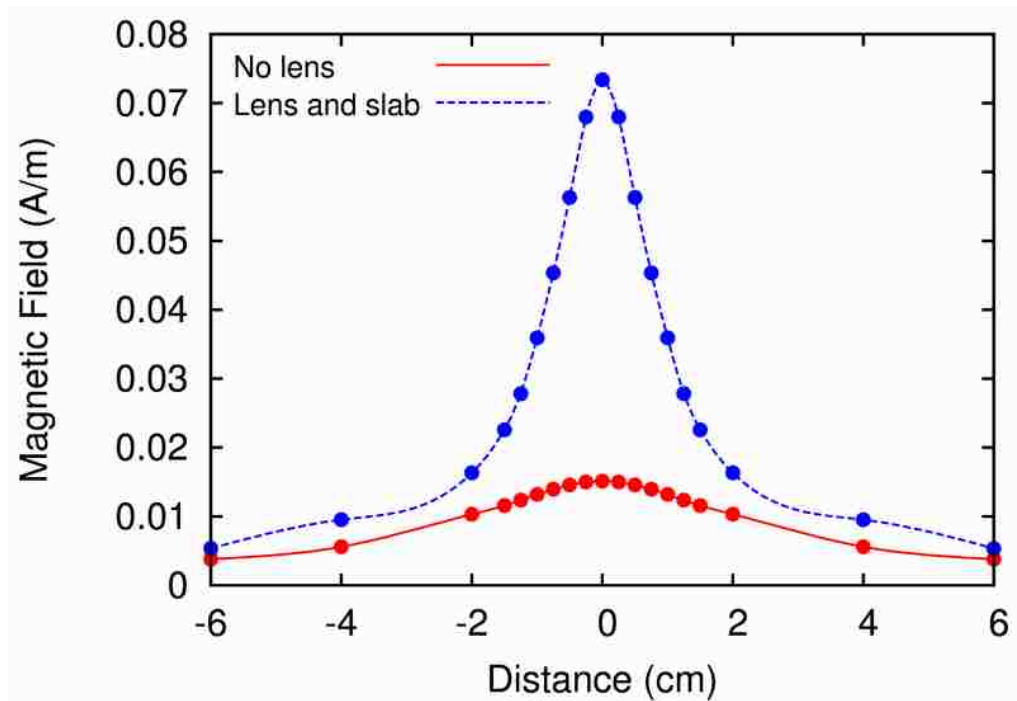


Figure 3.7: Peak magnetic field as a function of distance, along the  $x$ -axis, with and without focusing lens. The focal point is at  $x = 0$  cm.

Chapter 3. Design of the Focusing Lens

Table 3.5 summarizes important observations from Fig. 3.6 and Fig. 3.7. The ratio of the electric field spot size with and without the lens is  $EFSS_{NL}/EFSS_{WL} = 3.61/1.187 = 3.042 \approx \sqrt{\epsilon_{r_{max}}} = \sqrt{9.0}$ . For the magnetic field,  $HFSS_{NL}/HFSS_{WL} = 3.65/1.195 = 3.054 \approx 3.0$ . These results are in good agreement with analytical expectations.

Table 3.5: Spot diameter of E and H field with and without the focusing lens from Fig. 3.6 and Fig. 3.7

Field parameter	Spot diameter (cm)
E-Field No Lens	$EFSS_{NL} = 3.610$
H-Field No Lens	$HFSS_{NL} = 3.650$
E-Field With Lens	$EFSS_{WL} = 1.187$
H-Field With Lens	$HFSS_{WL} = 1.195$

## Chapter 4

# Experimental Measurements on a Five-Layer Focusing Lens

*“Never replicate a successful experiment.”*

*- Fett’s law*

This chapter presents experimental results for the focal waveform and beam width in a five-layer electromagnetic focusing lens. As explained in Ch. 3, this lens is used to reduce the impedance mismatch between the surrounding dielectric media and the biological target at the second focal point. The lens also helps obtain better focusing characteristics such as field amplification and spot size reduction. A five-layer lens, as opposed to a ten-layer lens, is used to validate our design and observe the characteristics of the lens materials, such as loss and dispersion, in the timescales of interest ( $\leq 100$  ps).

## 4.1 Tiny Fast-Pulse D-Dot Sensor Design in Dielectric Media

The measurement of fast ( $\leq$  hundred-picosecond) electromagnetic pulses inside a high-permittivity medium presents some challenges. These are especially associated with the shorter wavelengths and the contact of the D-dot antenna with the medium. This section discusses some techniques to mitigate these problems to some degree [2]. For a more general discussion see [32].

For tests in HEMP (high-altitude electromagnetic pulse) simulators (such as for in-flight missiles and aircraft) the requirements become significantly easier. This is associated with the relaxation of the source-region requirements to a situation where the D-dot (and B-dot sensors) are located in benign one-atmosphere (absolute) pressure air [17, 22, 33]. We are now faced with another problem as we extend our measurements into high-relative-dielectric-constant ( $\epsilon_r$ ) media which require a high-frequency response and we are mostly concerned with hundred picoseconds and below.

When optimized for air, ACD (asymptotic conical dipole) sensors have large bandwidths with rise times of the order of  $2h/c$ . Here  $h$  is the physical height of the ground-plane version (single-ended),  $2h$  is the full height of the differential version and  $c$  is the wave velocity in air [34, 35].

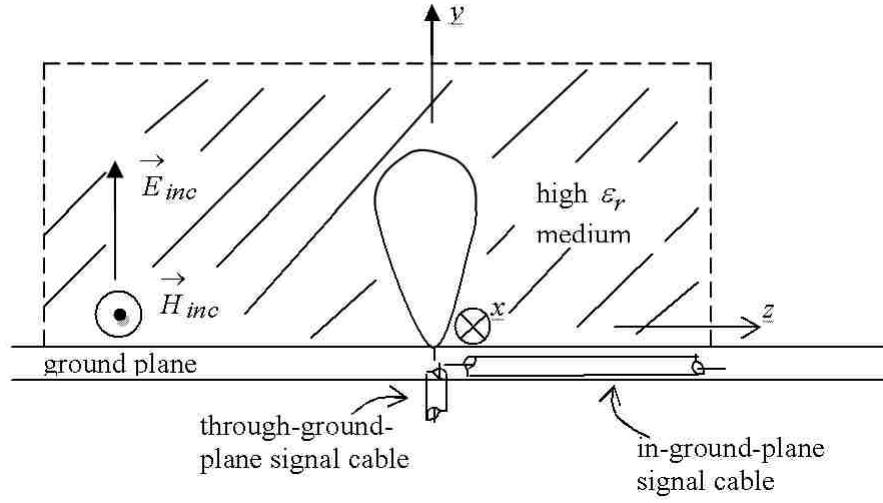
For ACD-type D-dot sensors, the continuity from the conducting antenna element to the high  $\epsilon_r$  medium is very important. Its fundamental operation is in a quasi-static sense in which radian wavelengths,  $\lambda$ , in the medium are large compared to  $h$ , the electrode length. As such, the sensor high-frequency response is reduced from the free-space case, roughly like  $\epsilon_r^{-1/2}$ , for a given  $h$ . There is also the question of adjusting the sensor geometry to match the medium to the sensor output impedance.

Concerning the importance of contact to the medium, one can think of this by imagining different cases of contact of the electrode with the high  $\epsilon_r$  (like high  $\sigma$ ) medium. If the contact is good only at the extreme end (or ends in the differential case) one is sampling a higher potential (voltage) than if one is only contacting the medium near the feed to the cable at the sensor output. If one is to think of the sensor calibration as though it were in free space, then the contact of the high  $\epsilon_r$  medium to the exposed sensor conductors must be the same as in the free-space case.

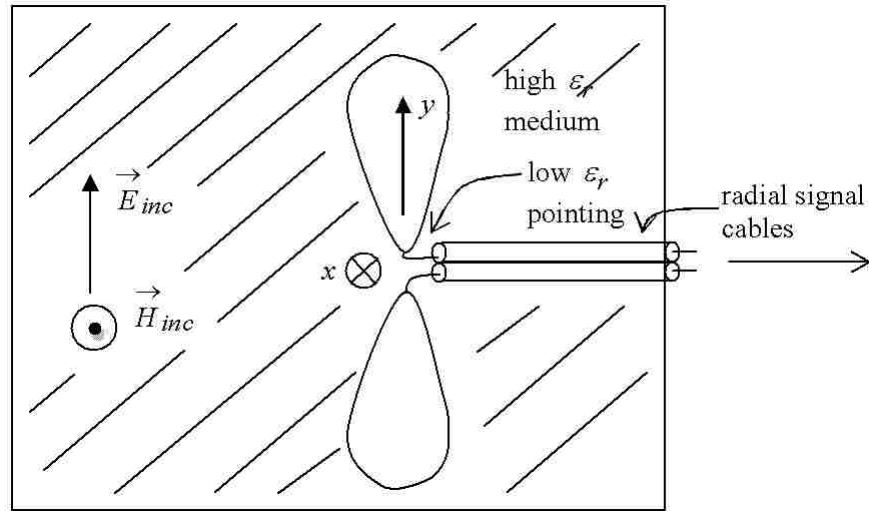
Fig. 4.1(a) shows a ground-plane version which senses the electric field normal to this plane. Also shown are two possible paths for the signal cable: through the ground plane (say with a connector there) which is an axial output, and in the ground plane which is a radial output.

Fig. 4.1(b) shows an example of how one might configure such a sensor away from a ground plane. In this case symmetry is very important. The output cable pair (bonded together or in an enclosing shield) should be truly radial ( $z$ -axis). Furthermore, it is important that the incident electric field have a negligible  $z$ -axis component, because any such component introduces a strong common-mode signal due to the antenna now being largely the signal-cable shields, not just the ACD conductors [36]. Note also the connections of the coax center conductors to the ACD conductors. There should be as little exposure of these conductors to the external medium as possible. They can also be coated in a low medium (e.g., polyethylene) to better maintain the cable characteristic  $\epsilon_r$  medium right up to the ACD conductors.

Noting the importance of the contact of the ACD conductors with the high  $\epsilon_r$  medium, we can now try to match the  $50\ \Omega$  load (or  $100\ \Omega$  differential). This changes the shape of the ACD conductors as in [35, 37]. The asymptotic cone at the sensor base has a pulse impedance of [38]



(a) Ground-plane version



(b) In-medium version

Figure 4.1: Small D-Dot Sensors [2].

$$Z_a = \frac{Z_w}{2\pi} \ln \left[ \cot \left( \frac{\theta_0}{2} \right) \right] \quad (\text{single-ended form}),$$

$\theta_0$  = angle of cone surface from  $y$ -axis,

$$Z_w = \left[ \frac{\mu_0}{\epsilon} \right]^{1/2} = \epsilon_r^{-1/2} Z_0 = \text{wave impedance of medium}, \quad (4.1)$$

$$Z_0 = \left[ \frac{\mu_0}{\epsilon_0} \right]^{1/2} \approx 377 \, \Omega.$$

Stated another way we have

$$Z_a = 50 \Omega = 60\epsilon_r^{-1/2} \ln \left[ \cot \left( \frac{\theta_0}{2} \right) \right]. \quad (4.2)$$

From this we can construct Table 4.1. As we can see, as we go to higher  $\epsilon_r$ , the ACD sensor becomes thinner, approaching a needle, provided we match to  $50 \Omega$ .

Table 4.1: Asymptotic Cone Angles

$\epsilon_r$	$\theta_0$ (degrees)
1	46.98
3	26.57
9	9.39
27	1.51
81	0.06

### 4.1.1 Practical Considerations

For such tiny (mm) sensors it has been found to be more practical to replace a body of revolution (ACD) by a flat conical plate. This allows the electrode to penetrate the dielectric medium with minimum perturbation, assuring more reliable contact with the medium.

### 4.1.2 Comments Concerning Calibration

With sensors embedded in the high  $\epsilon_r$  medium one needs to know their accuracy. As previously discussed, the contact of the electrode with the medium is critical. How



does one know how well contact has been made? Is the contact continuous over all the electrode, or just in spots? If one inserts the electrode in the medium, removes it, and reinserts it, is the contact the same?

One check might be to measure the capacitance of the electrode to the ground plane (single ended sensor), or between the two electrodes (differential sensor). Using known ACD formulae and the value of  $\epsilon_r$ , the capacitance can be calculated [35, 37], and compared to the measured value. A measured capacitance less than the theoretical value indicates some lack of contact with the medium.

As one can see, measurements of pulsed electromagnetic fields with hundred picoseconds and below resolution in high  $\epsilon_r$  media presents some considerable challenges. It is not just the speed involved. It includes the shorter wavelengths in the high  $\epsilon_r$  medium and the contact of the sensor with the medium (especially for the ACD).

## 4.2 Experimental Setup

Figure 4.2 shows the experimental setup. A block diagram of the setup is shown in Fig. 4.3. It consists of a prolate-spheroidal reflector and two feed arms with a ground plane, i.e., a four feed arm PSIRA configuration. A 10 V, 45 ps ramp-rising signal, generated by a Picosecond Pulse Labs<sup>1</sup> pulse generator, is used as a source at the first focal point. The lens and target medium (slab) are placed at the second focal point. A handmade, fast D-dot sensor is placed inside the target medium. A 100 ps filter is placed between the D-dot probe and the sampler. The signal from the D-dot probe is measured using a Tektronix TDS 8000B digital sampling oscilloscope.

---

<sup>1</sup>2500 55th Street Boulder, Colorado 80301, USA. <http://www.picosecond.com/>

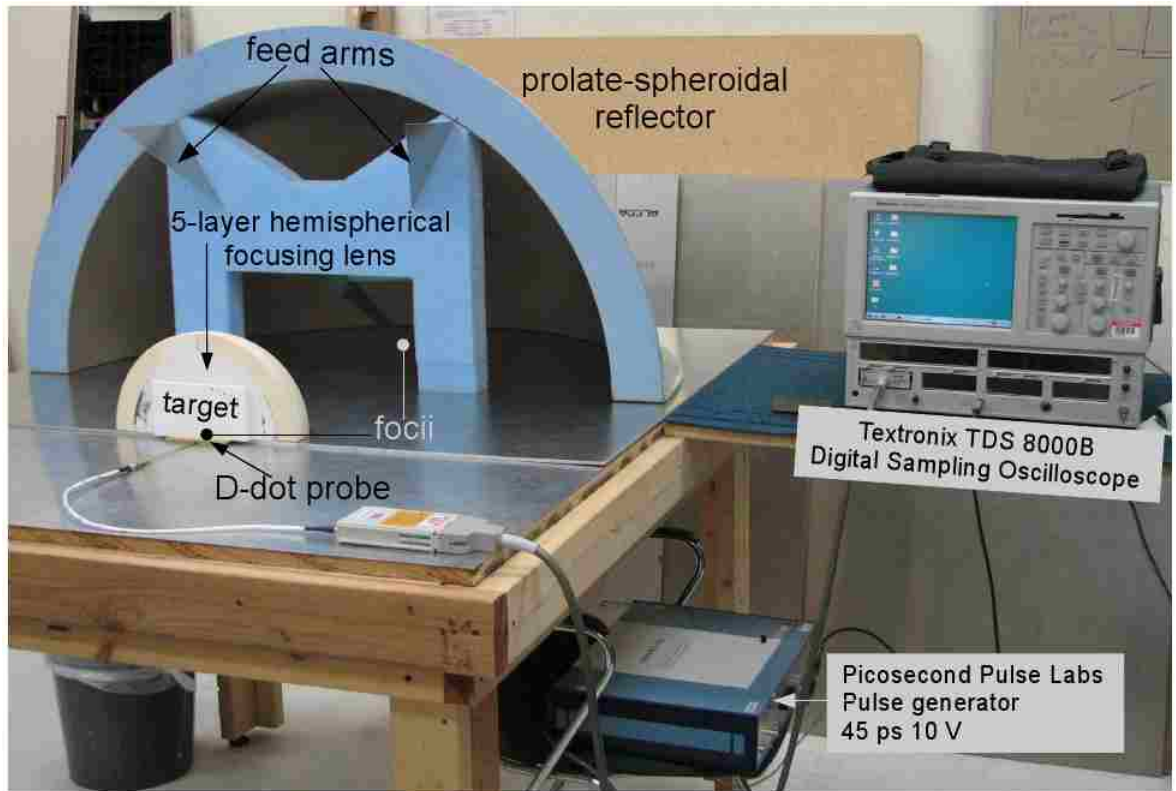


Figure 4.2: Experiment setup of  $60^\circ$  four feed arm PSIRA with focusing lens, target and D-dot probe.

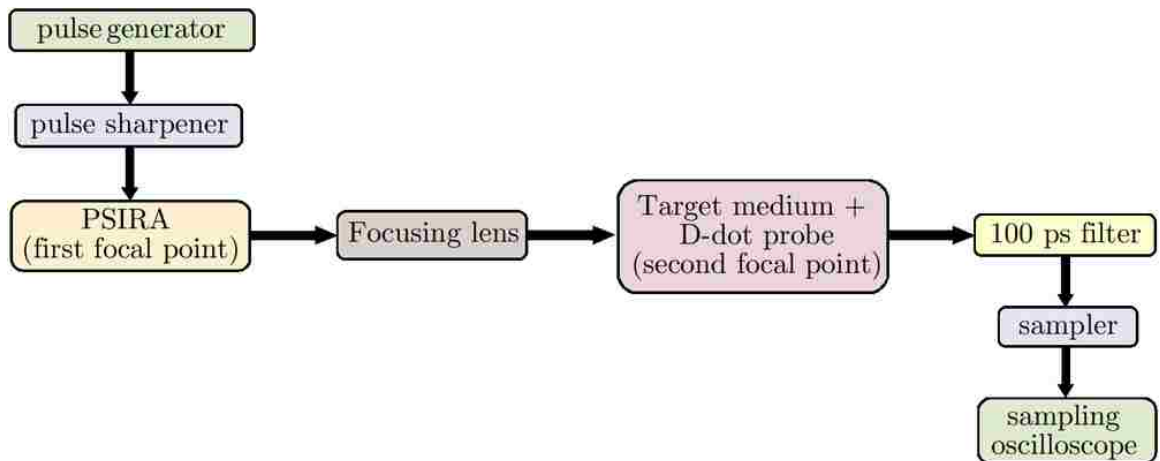


Figure 4.3: Block diagram of the experimental setup.

The 5-layer hemispherical focusing lens and target were made to our specifications by TPL Inc.<sup>2</sup>. The nano-composite dielectric material developed by TPL Inc. is ideal for the fabrication of our multi-layer lens since desired (arbitrary) dielectric constants can be achieved. The slab, placed in front of the lens, is used to simulate the target medium.

### 4.2.1 D-dot sensor

The handmade D-dot probe used to measure electric fields inside the target medium is shown in Fig. 4.4. The probe was constructed with a 47-mil-diameter (1.2 mm) PE-047SR semi-rigid coaxial cable that emerged at the surface of the measurement ground-plane. The cable center wire attached to a 3-mm-high, two-dimensional, teardrop-shaped electrode. The initial wedge angle of the electrode was 58 degrees (half angle  $\theta_0 = 29^\circ$ ), which matched the 50-ohm line impedance when immersed in the dielectric. (Note that (4.2) is for a three-dimensional cone. The formula to determine the impedance of the electrode, two-dimensional cone, is involved and is derived in [39–42].) The thin foil electrode was then inserted into an expanded vertical cut in the elastic dielectric material, which was then squeezed closed to provide a snug fit around the probe.

### 4.2.2 100 ps Filter

The rise time of the pulser is 45 ps. However, our analytical calculations and numerical simulations, Ch. 3, assume an input with a 100 ps rise. Therefore, a low-pass filter, custom designed by Picosecond Pulse Labs, is used to stretch the 45 ps pulse to a pulse with a 100 ps rise time while maintaining the same peak amplitude ( $\pm$  few mV).

---

<sup>2</sup>3921 Academy Parkway North NE, Albuquerque, NM 87109, <http://www.tplinc.com/>

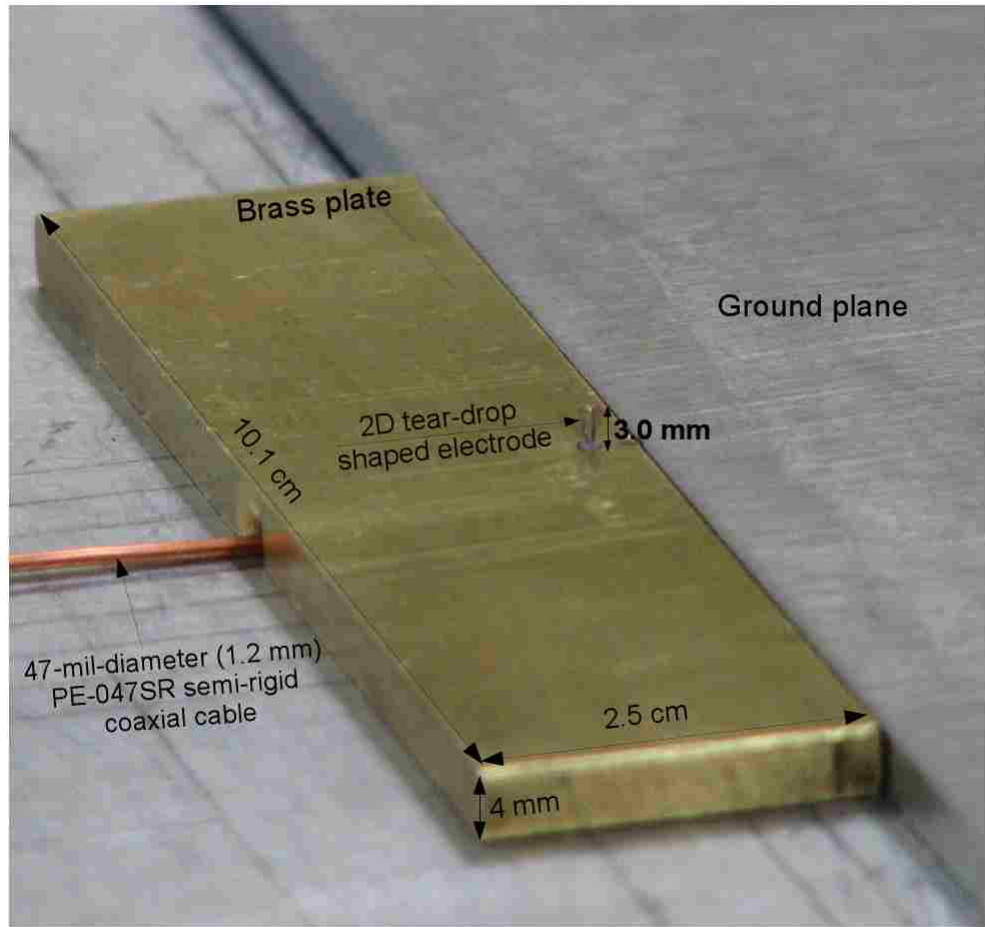


Figure 4.4: D-dot probe to measure electric field inside target medium.

Fig. 4.5 compares the waveforms from the pulser with and without the filter. The waveform with the filter has the same shape (compared to that without the filter) and a peak amplitude of approximately 10 V. The maximum rate of rise,  $t_{mr}$ , of the filter, as determined from Fig. 4.5, is 100.83 ps. The filter is completely characterized in [43].

In theory, the filter can be placed anywhere in the setup since the system is linear. However, in our experimental setup, placing the filter at the first focal point was difficult. The setup in Fig. 4.3 was found to minimally perturb the measurements.

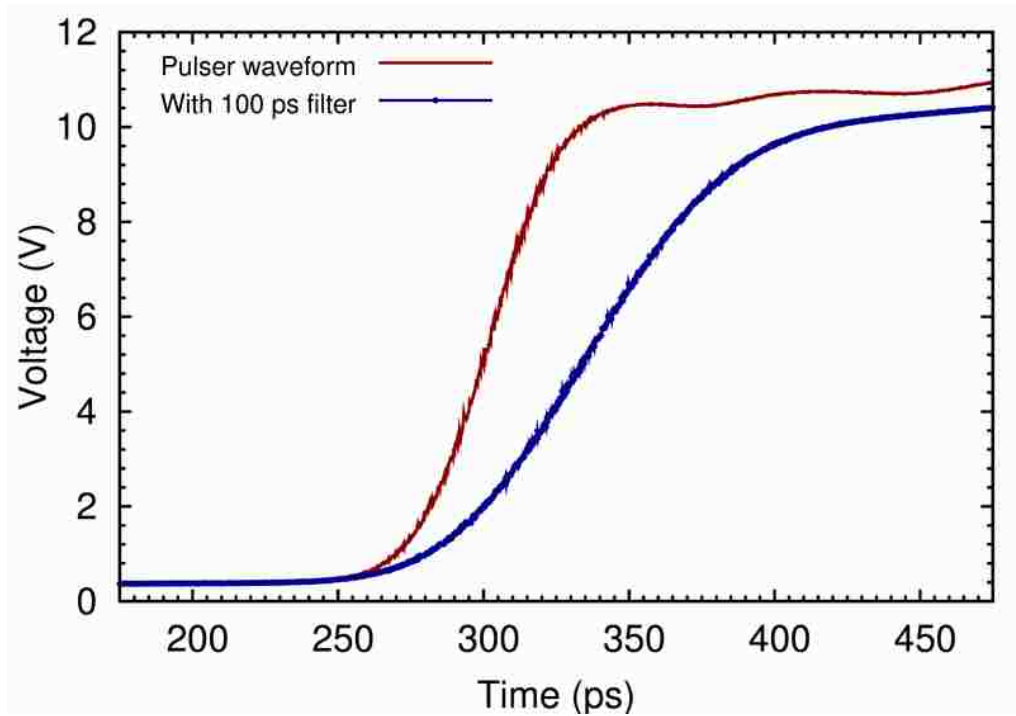


Figure 4.5: Comparison of pulser waveforms with and without filter.

### 4.3 Focal Waveform and Beam Width in Air

The focal waveform and beam width in air are required to determine the electromagnetic enhancements, as calculated in Ch. 3, inside the focusing lens. Before proceeding to present these results, the calibration of the D-dot probe in air is detailed as this is not obvious [43].

#### 4.3.1 Calibration of the D-dot Probe in Air

The D-dot probe is calibrated in air (i.e., without the focusing lens), at the second focal point, using the prepulse. The electric field is obtained from the voltage response of the probe as follows.

The current,  $I$ , measured by the D-dot probe is related to its equivalent area,

$A_{eq}$ , and voltage,  $V$ , as

$$I = \frac{V}{Z_c} = A_{eq} \frac{dD}{dt}, \quad (4.3)$$

where  $Z_c = 50 \Omega$  is the characteristic impedance of the cable connecting the probe to the sampling oscilloscope. Given  $dD/dt$ , the electric field can be calculated as

$$E = \frac{1}{\epsilon Z_c A_{eq}} \int_{-\infty}^t V(t') dt', \quad (4.4)$$

where  $\epsilon = \epsilon_0 \epsilon_r$  is the relative permittivity of the medium surrounding the probe. For air,  $\epsilon_r = 1$ . Since the experiments use a four feed-arm PSIRA over a ground plane, the feed arm impedance is  $100 \Omega$ . The voltage transmitted to the feed arms from the pulse generator is,

$$V = TV_0, \quad T = \text{transmission coefficient} = \frac{2Z_l}{Z_l + Z_c} = \frac{2(100)}{100 + 50} = 1.33. \quad (4.5)$$

The electric field measured by the D-dot probe is normalized to a 1 V input as

$$E_N = \frac{1}{20T \epsilon Z_c A_{eq}} \int_{-\infty}^t V(t') dt'. \quad (4.6)$$

The theoretical value of the prepulse in air is  $E_{pa} = -0.7$  V. The prepulse measured by the probe, normalized to a 1 V input is,

$$E_{pa}^{\text{measured}} = \frac{1}{20T \epsilon_0 Z_c A_{eq}} \int_{-\infty}^t V(t') dt', \quad (4.7)$$

where  $T = 1.33$ ,  $Z_c = 50 \Omega$  and  $A_{eq} = 10^{-4} \text{m}^2$ . We require that the measured prepulse be  $E_{pa}$ . For this we multiply the measured electric field by the calibration factor  $C_a$ , where

$$C_a = \frac{E_{pa}}{E_{pa}^{\text{measured}}}. \quad (4.8)$$

### 4.3.2 Focal Impulse Waveform

The electric field impulse waveform, at the second focal point, is shown in Fig. 4.6. One observes that the shape and magnitudes of the prepulse, impulse and postpulse are similar to the numerical simulation results in Ch. 3.

The distance between the geometrical focal points is 75 cm. The tip of the D-dot probe on the brass mount, Fig. 4.4, is at  $z = +3$  mm from the second focal point, i.e., the D-dot probe is at a distance of 75.3 cm ( $75 + z$ ) from the (geometrical) first focal point [44]. The time taken for the wave to travel from the first focal point to the probe tip is

$$\frac{75.3 \text{ cm}}{3 \times 10^8 \text{ cm/s}} \approx 2.51 \text{ ns.} \quad (4.9)$$

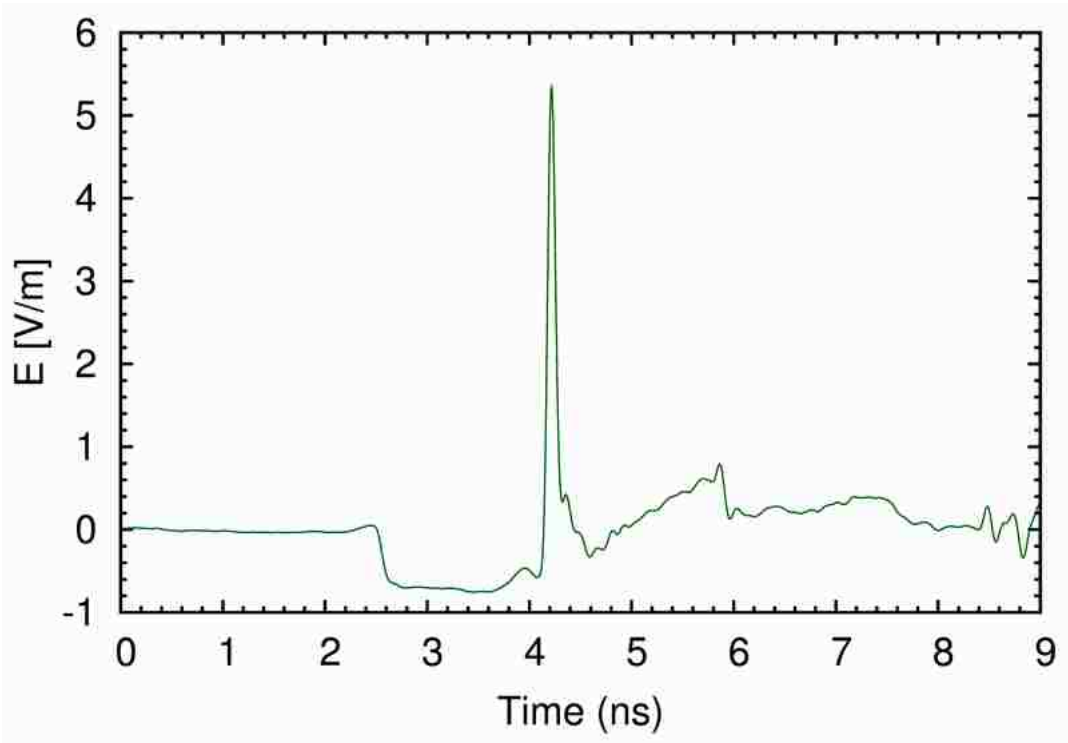


Figure 4.6: Electric field focal waveform in air with 100 ps filter.

In the experiments, the time at which the prepulse is registered by the oscilloscope is not what one would expect from (4.9) as there is no fixed time of reference. A more

accurate method of making the measurements is to place a second D-dot probe at the first focal point. The second D-dot probe can be used to determine the relative time of arrival of the electric fields measured by the D-dot probe at the second focal point. One should also note that the cables connecting the D-dot probe to the oscilloscope introduce a time lag in the data measured by the probe. This time lag is not accurately known and would also introduce time shifts in the fields measured by the probe. Therefore, the waveform in Fig. 4.6 is shifted so that the prepulse starts at 2.51 ns.

The “zoomed-in” view of the impulse is shown in Fig. 4.7. The peak electric field amplitude is  $E_{\max} = 5.34$  V/m. The prepulse, impulse and postpulse are considered as three separate events, i.e., the impulse can be considered to be super-imposed on the prepulse. Therefore, the amplitude of the impulse,  $E^I$ , is calculated with respect to the average of the start and end of the impulse event;  $E_s^i = -0.6$  V/m and  $E_e^i = 0.4$  V/m, as shown in Fig. 4.7, i.e.,

$$\Upsilon = \left| \frac{E_s^i + E_e^i}{2} \right| = 0.1 \text{ V/m}, \quad (4.10)$$

and

$$E^I = E_{\max} + \Upsilon = 5.44 \text{ V/m}. \quad (4.11)$$

The FWHM of the impulse is 85 ps, as shown in Fig. 4.7. One would expect the FWHM to be identical to the  $t_{\text{mr}}$  of the input pulse ( $t_{\text{mr}} = 100$  ps). The reason for this discrepancy is that the higher frequencies in the input pulse are better focused than the lower frequencies, i.e., the focusing action itself filters out lower frequency content in the focused waveform. Similar results observed in simulations corroborate this explanation.



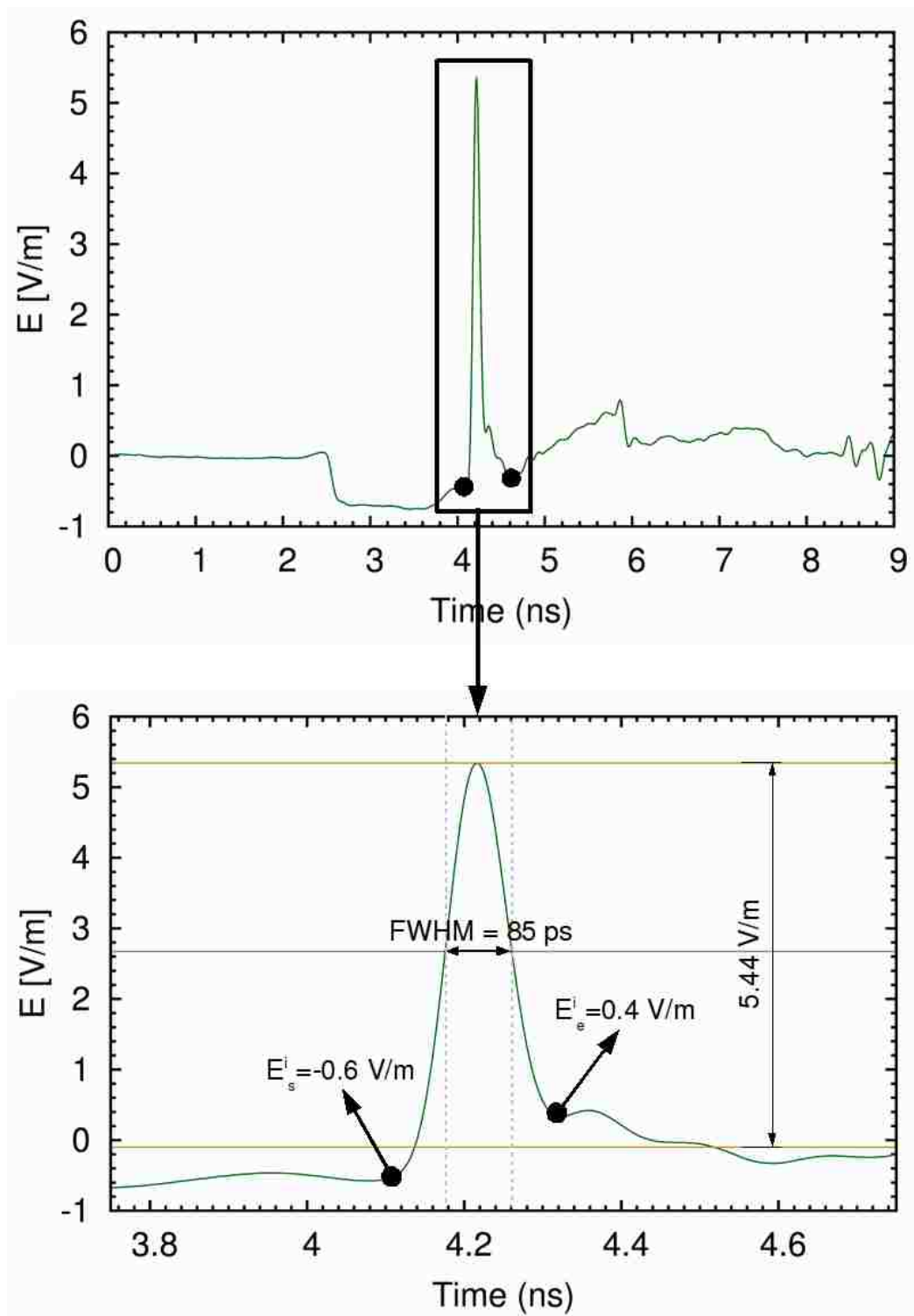


Figure 4.7: “Zoomed-in” view of electric field impulse at second focal point in air with 100 ps filter.

### 4.3.3 Beam width (Spot size)

The beam width (spot diameter) is shown in Fig. 4.8. The error in measurement is approximately  $\pm 5\%$ . The data points do not lie along a smooth curve and this makes it difficult to determine the spot size. Therefore, a Gaussian curve of the form

$$f(x) = ae^{-b(x+c)^2+d} + e, \quad (4.12)$$

was fit to the data, where  $x$  is the distance along the  $x$ -axis (see Fig. 3.3 for the coordinate system) from the focal point. The fit parameters are  $a = 0.839$ ,  $b = 0.106$ ,  $c = 0.213$ ,  $d = 1.525$ ,  $e = 1.439$ . The spot diameter, as determined from the fit, is 4.397 cm.

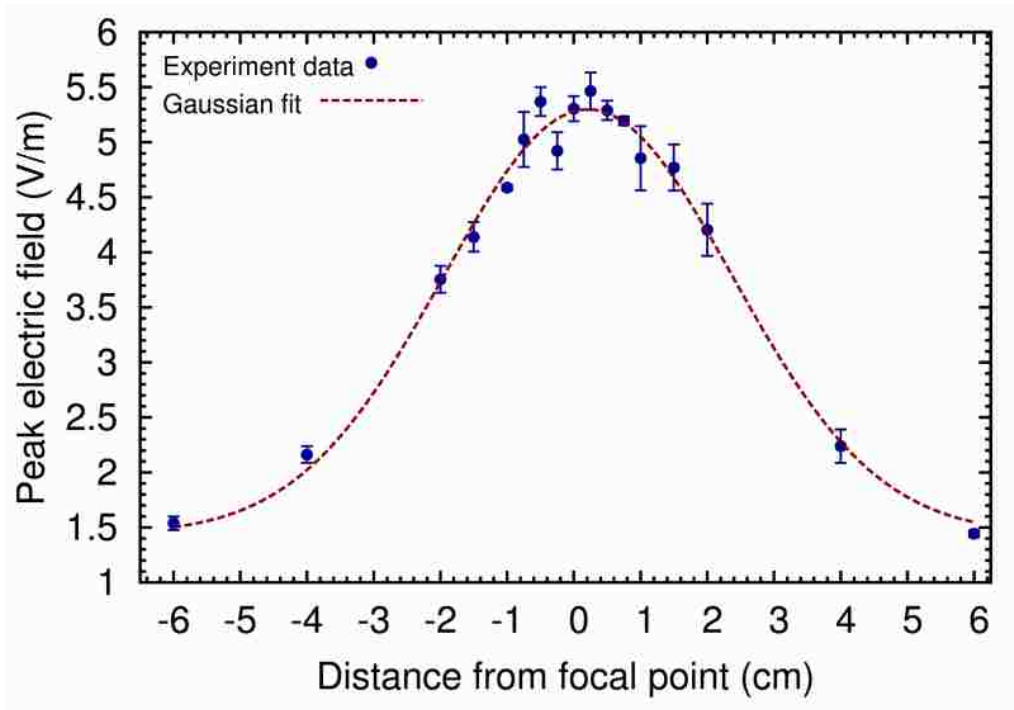


Figure 4.8: Beam width in air and Gaussian curve fit.

The beam width from experiments is compared to that obtained from numerical simulations in Fig. 4.9. One observes that the geometrical focal point in the experiments is shifted by approximately  $x = +0.25$  cm. This is most likely due to the misalignment of the reflector. The spot diameter in the numerical simulations

was 3.610 cm, Ch. 3, i.e., the experimental beam width is 22% greater than that in the simulation.

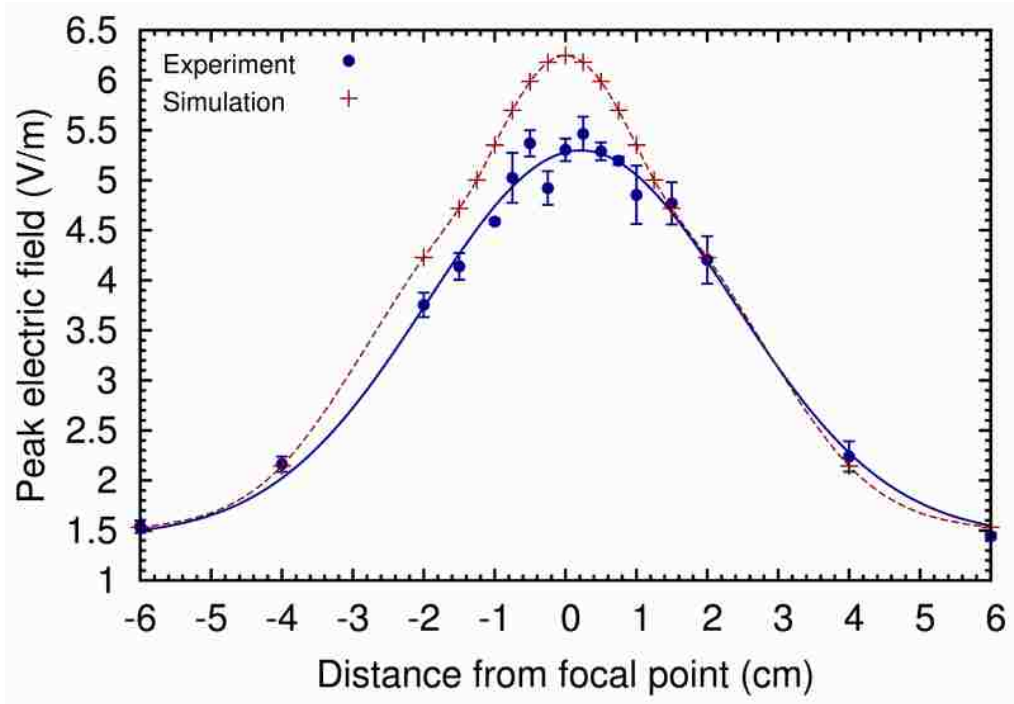


Figure 4.9: Comparison of spot size obtained from experiment and numerical simulation.

## 4.4 Focal Waveform and Beam Width in the Focusing Lens

As might be expected, measurements in the focusing lens are more complicated than those in air. The D-dot probe must be calibrated in the target medium. From Ch. 3, one expects an electric field enhancement of  $\epsilon_{rt}^{1/4} = 1.73$  in the focal waveform and a reduction of  $\epsilon_{rt}^{1/2} = 3$  in the spot size. A comparison of the focal waveforms in air and in the target medium, in the spectral domain, also provides insight into the losses in the lens materials [44].

#### 4.4.1 Calibration of the D-dot Probe in the Target Medium

The calibration of the D-dot probe in the target medium is more complicated as an “infinitely” large sample is not available. The probe is calibrated in the target medium using only the slab for measurement as shown in Fig. 4.11. The probe is inserted between a slit cut in the slab, Fig. 4.10. The relative permittivity of the target medium is known from previous measurements,  $\epsilon_{rt} = 8.2$  [45].

The theoretical value of the prepulse inside the target medium is

$$E_{pt} = TE_{pa}, \quad (4.13)$$

where  $T$  is the transmission coefficient from air into the target medium,

$$T = \frac{2}{1 + \sqrt{\epsilon_{rt}}}, \quad (4.14)$$

and  $\epsilon_{rt}$  is the relative permittivity of the target medium. The prepulse measured by the probe, normalized to a 1 V input, is

$$E_{pt}^{\text{measured}} = \frac{1}{20T\epsilon_0\epsilon_{rt}Z_cA_{eq}} \int_{-\infty}^t V(t')dt'. \quad (4.15)$$

We require that the measured prepulse be  $E_{pt} = TE_{pa}$ . For this we multiply the measured electric field by the calibration factor  $\mathcal{C}_t$ , where

$$\mathcal{C}_t = \frac{E_{pt}}{E_{pt}^{\text{measured}}} = \left( \frac{2}{1 + \sqrt{\epsilon_{rt}}} \right) \frac{E_{pa}}{E_{pt}^{\text{measured}}}, \quad (4.16)$$

and  $E_{pa} = -0.7$  V/m is the analytical value of the prepulse in air.

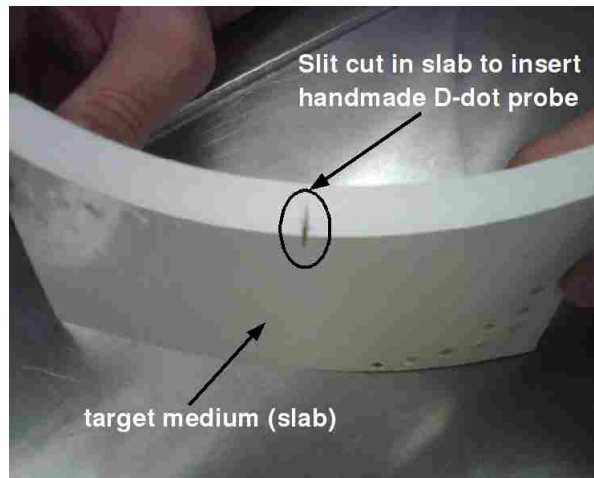


Figure 4.10: Slit cut in target medium/slab into which the handmade D-dot probe is inserted.

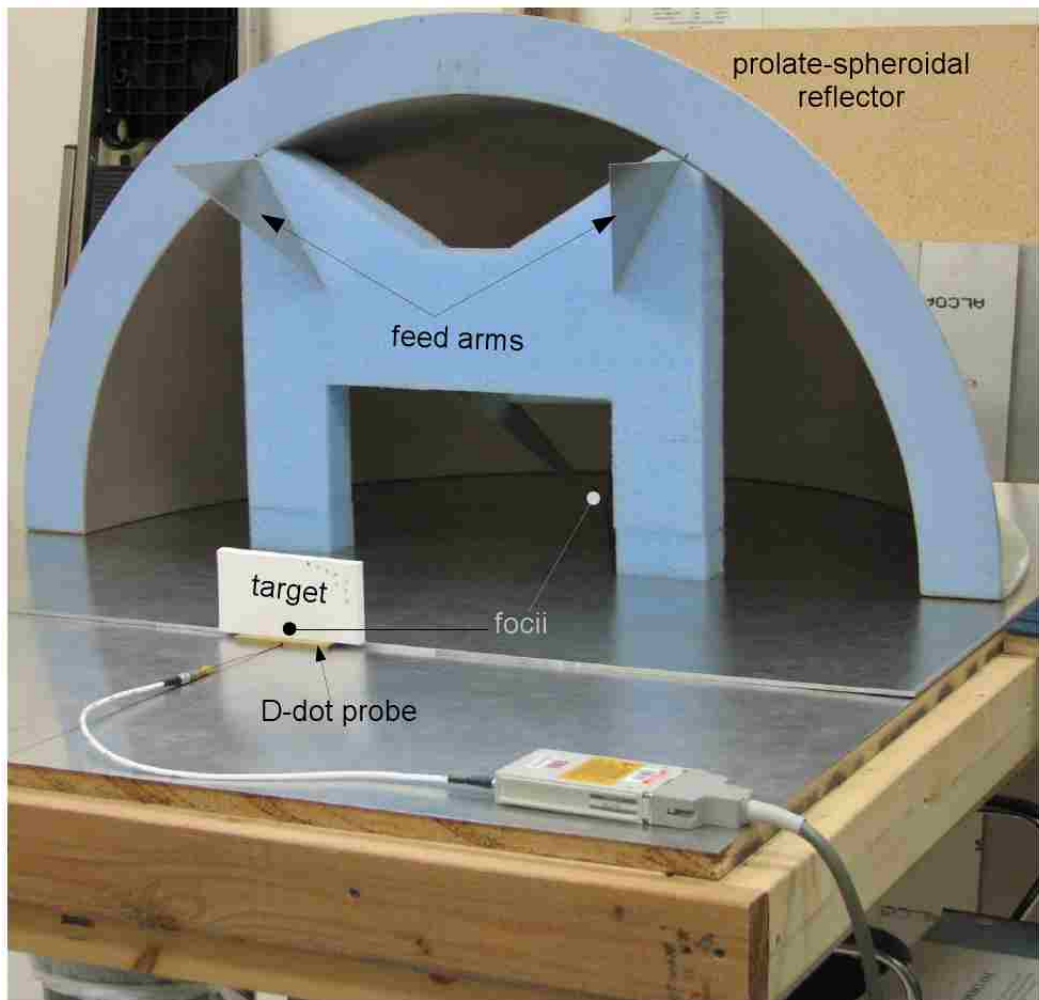


Figure 4.11: Setup to calibrate D-dot probe inside dielectric medium.

Figure 4.12 shows the schematic to calibrate the probe inside the target medium (slab). The width of the slab is  $d_t$  cm. Consequently, the prepulse inside the slab,  $E_{pt} = TE_{pa}$ , undergoes reflections at the slab boundary. The reflected wave,  $E_{pt}^r = \Gamma E_{pt}$ , interferes with the direct wave,  $E_{pt}$ , after the round trip time  $t_p$ ;  $\Gamma$  is the reflection coefficient. Therefore, for times  $t > t_p$ ,  $E_{pt}$  cannot be used to calibrate the probe as the analytical value of the prepulse is not known. In Fig. 4.12,  $d'$  is the distance between the probe tip, on the surface of the brass mount, and geometrical second focal point. The round trip time of the reflected wave is

$$t_p = \frac{2(d_t - d')\sqrt{\epsilon_{rt}}}{c}, \quad (4.17)$$

where  $c$  is the speed of light in vacuum.

Given that  $d' \approx 0.3$  cm and  $d_t \approx 1.27$  cm  $\Rightarrow t_p \approx 187.42$  ps, i.e., only the first  $\approx 200$  ps of the prepulse inside the slab can be used to calibrate the D-dot probe. The electric field response and the “zoomed-in” prepulse are shown in Fig. 4.13.

When the probe is inside the target medium, the time taken for the wave to reach the probe tip is

$$\frac{75 \text{ cm}}{3 \times 10^8 \text{ cm/s}} + \frac{(0.3 \text{ cm}) \sqrt{8.4}}{3 \times 10^8 \text{ cm/s}} \approx 2.53 \text{ ns}. \quad (4.18)$$

As for the measurements in air, the focal waveform in Fig. 4.13 is time-shifted so that the prepulse starts at 2.53 ns.

The D-dot probe is designed to have a pulse impedance of  $50 \Omega$  in the dielectric medium, i.e.,  $150 \Omega$  in air. The impedance mismatch between the probe tip and the input pulse, for the measurements in air, causes reflections. However, the probe, of height  $h = 3$  mm, is resonant at frequencies above

$$f \approx \frac{c}{h/4} = \frac{3 \times 10^{11} \text{ mm}}{0.75 \text{ mm}} = 0.4 \text{ THz}, \quad (4.19)$$

i.e., in a quasi-static sense, the measurements are valid over a very large frequency spectrum of the input pulse and are therefore considered to be sufficiently accurate.

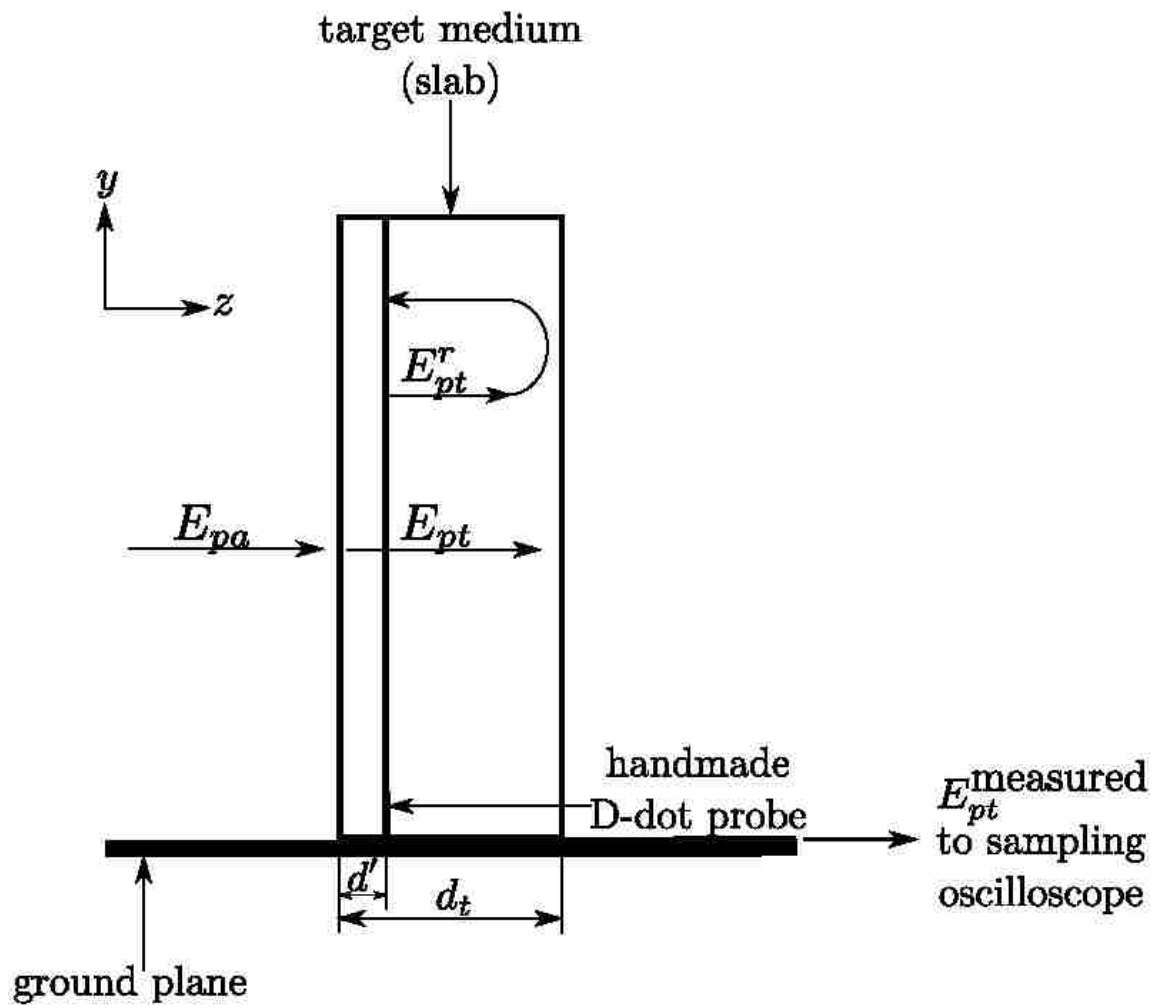


Figure 4.12: Schematic to calibrate D-dot probe.

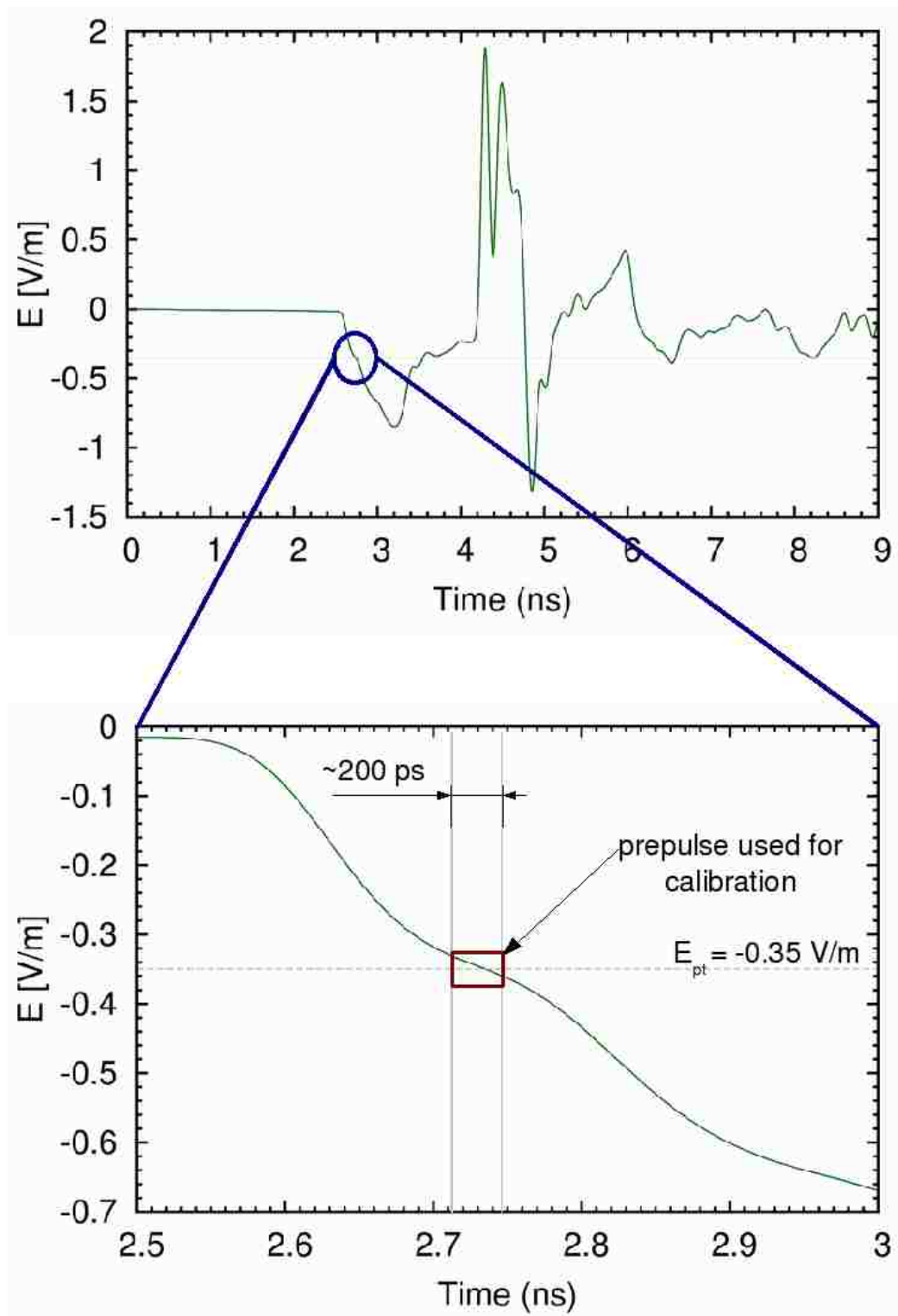


Figure 4.13: Electric field measured by D-dot probe inside slab (top); “zoomed-in” prepulse used for calibrating D-dot probe inside target medium (bottom).



### 4.4.2 Focal impulse waveform

The electric field impulse waveform, at the second focal point, in the focusing lens, is shown in Fig. 4.14. As with the numerical simulation results in Ch. 3, one observes the prepulse is dispersed, as the lens is not designed to focus this part of the waveform. This is advantageous as it increases the amplitude of the impulse. One also notes the large negative area in the post pulse (low frequencies). The lower frequencies in the input pulse are filtered due to the geometry of the lens.

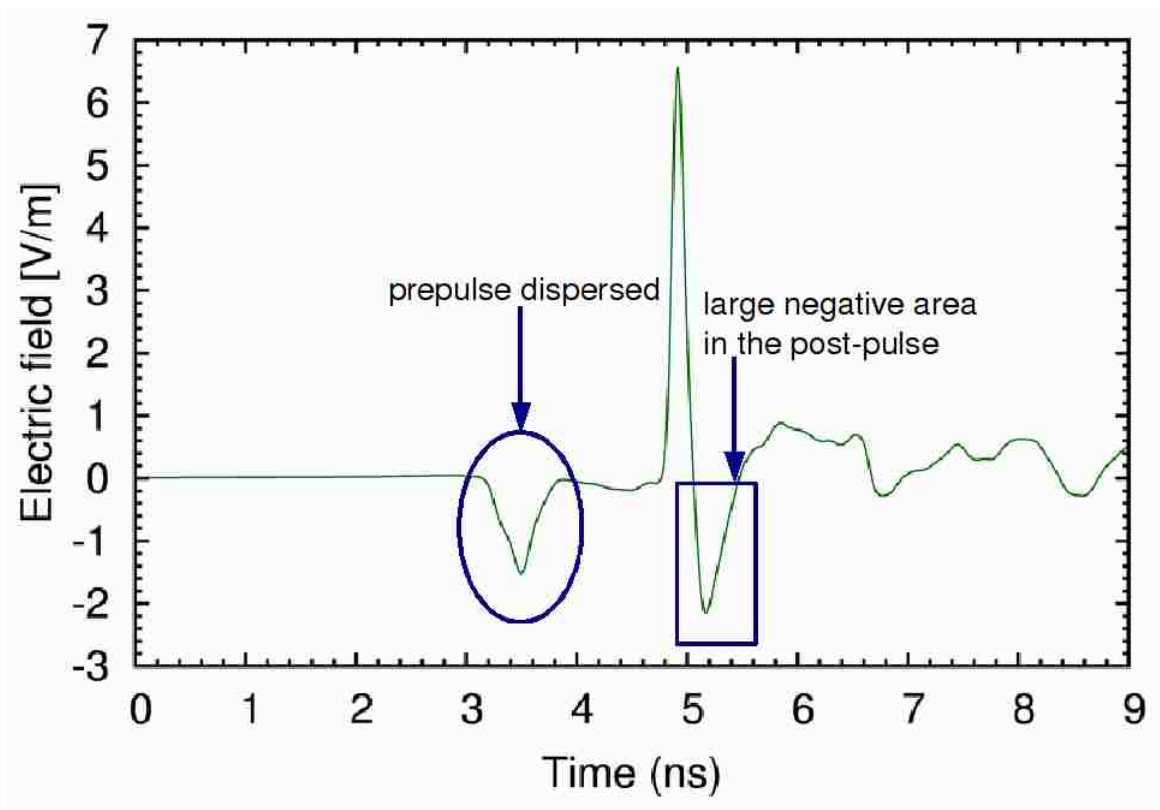


Figure 4.14: Electric field focal waveform in lens with 100 ps filter.

As for the focal waveform results in air in Sec. 4.3.2, the waveform in Fig. 4.14 is time-shifted so that the prepulse starts at 3.146 ns [44].

The “zoomed-in” view of the electric field impulse is shown in Fig. 4.15. The peak electric field amplitude is  $E_{\max} = 6.557$  V/m. As in Sec. 4.3.2, the pre-pulse, impulse and post-pulse are considered as three separate events, i.e., the impulse can be considered to be super-imposed on the pre-pulse. Therefore, the amplitude of the impulse,  $E^I$ , is calculated with respect to the average of the start and end of the impulse event;  $E_s^i = 0.0$  V/m and  $E_e^i = -2.2$  V/m, as shown in Fig. 4.15, i.e.,

$$\Upsilon = \left| \frac{E_s^i + E_e^i}{2} \right| = 1.1 \text{ V/m}, \quad (4.20)$$

and

$$E^I = E_{\max} + \Upsilon = 7.66 \text{ V/m}. \quad (4.21)$$

The FWHM is 127.5 ps, as shown in Fig. 4.15. The large FWHM is most likely due to loss and dispersion in the lens materials (without loss and dispersion the FWHM would be 100 ps).

Figure 4.16 compares the focal impulse waveforms in air and inside the focusing lens. One observes the enhancement inside the lens. Since the half-widths of the impulse responses in air and in the lens are not identical, the electric enhancement is given by the ratio of the areas,  $A = (\text{half-width})(\text{peak amplitude}) = \text{FWHM} \cdot E_{\max}$ , under the curves, i.e.,

$$A_{\text{impulse-air}} = (85 \text{ ps})(5.44 \text{ V/m}) = 462.4 \text{ ps V/m},$$

$$A_{\text{impulse-lens}} = (127.5 \text{ ps})(7.66 \text{ V/m}) = 976.65 \text{ ps V/m}.$$

The electric enhancement is  $A_{\text{impulse-lens}}/A_{\text{impulse-air}} \approx 2.11$ . This is much larger than the analytical estimate,  $\epsilon_r^{1/4} = 8.2^{1/4} \approx 1.69$ . The reason for this disagreement is due to the 85 ps FWHM of the impulse in air [43].

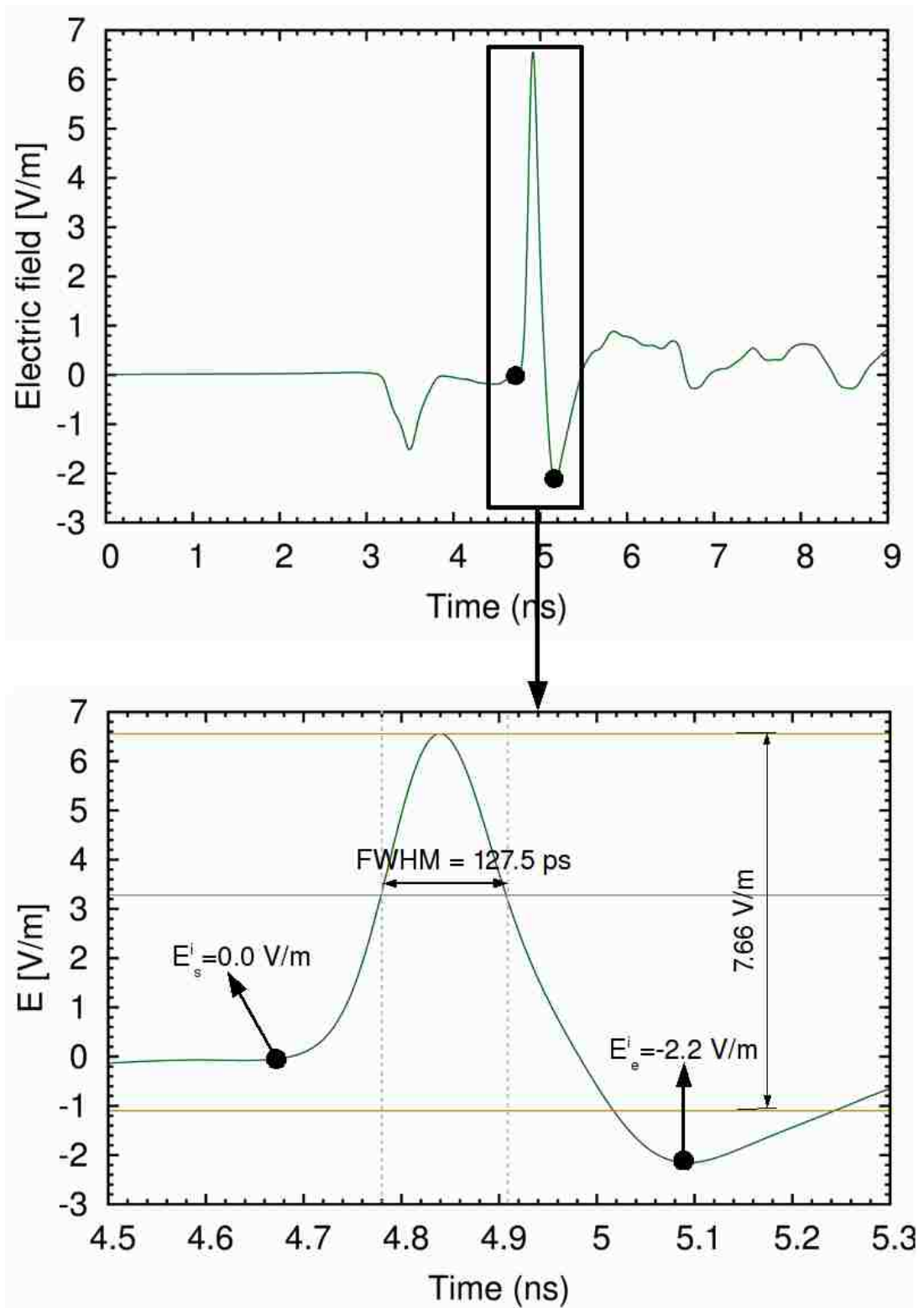


Figure 4.15: “Zoomed-in” view of electric field impulse at second focal point in lens with 100 ps filter.

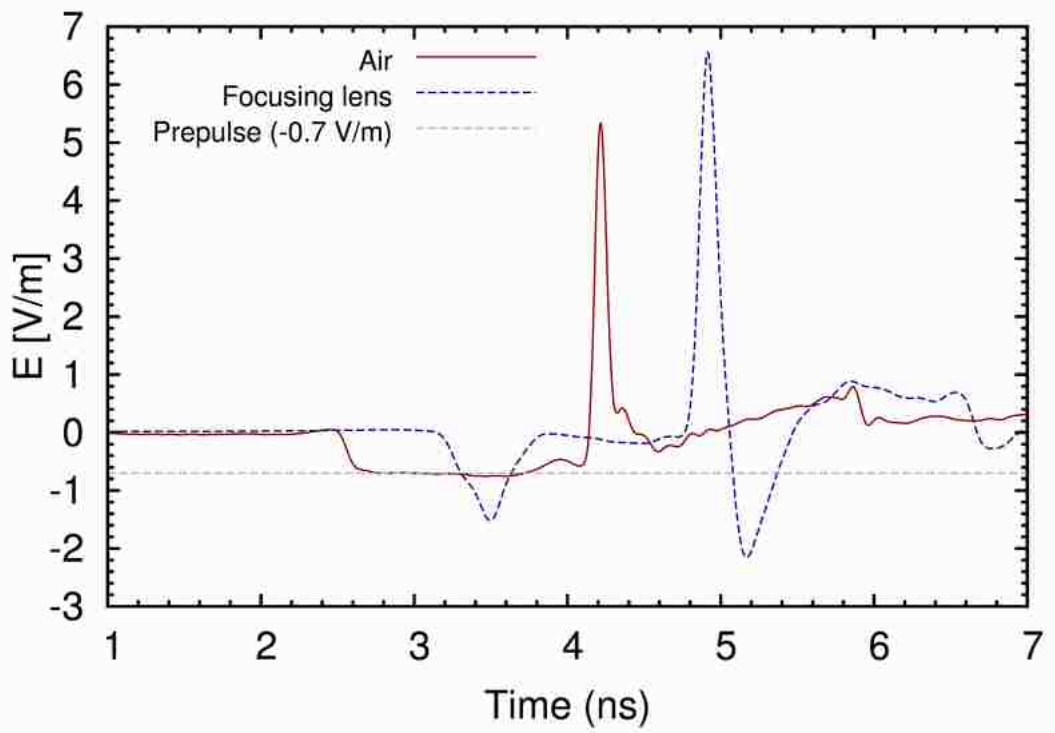


Figure 4.16: Comparison of focal impulse waveforms, at the second focal point, in air and inside the lens, with the 100 ps filter.

The analytical approximations do not consider the filtering of the lower frequencies due to the focusing of the wave, at the second focal point, in air. This results in a much higher electric enhancement as observed above. Of course, one could also simply examine the ratio of the peak electric fields inside the lens and in air, which is  $7.66/5.44 = 1.408$ .

The areas under the curves as obtained from numerical simulations are

$$A_{\text{impulse-air}} = (64.569 \text{ ps})(6.2466 \text{ V/m}) = 403.337 \text{ ps V/m},$$

$$A_{\text{impulse-lens}} = (70.233 \text{ ps})(10.7248 \text{ V/m}) = 753.235 \text{ ps V/m}.$$

The electric enhancement is  $A_{\text{impulse-lens}}/A_{\text{impulse-air}} \approx 1.868$ . This is also larger than that predicted analytically. The smaller FWHM in air and inside the lens indicates that the filtering of lower frequencies, due to the focusing of the wave at the second focal point, is taken into consideration in the numerical simulations.

The enhancement obtained from the ratio of the peak focal impulse electric fields is  $10.725/6.247 = 1.717$ .

### 4.4.3 The focusing lens as a bandpass filter

The ratio of the magnitudes of the Fourier transform of the impulse waveforms from experiments, in the lens and in air, is shown in Fig. 4.17. The bandwidth of the lens is approximately 3 GHz, from 0.4 GHz to 3.4 GHz. Above 3.5 GHz there is almost no electric field enhancement (analytical or experimental). The focusing lens thus acts as a bandpass filter, filtering frequencies below 0.4 GHz and above 3.4 GHz. The filtering of higher frequencies is due to losses occurring in the lens materials while the the lower frequencies are filtered due to the lens geometry.

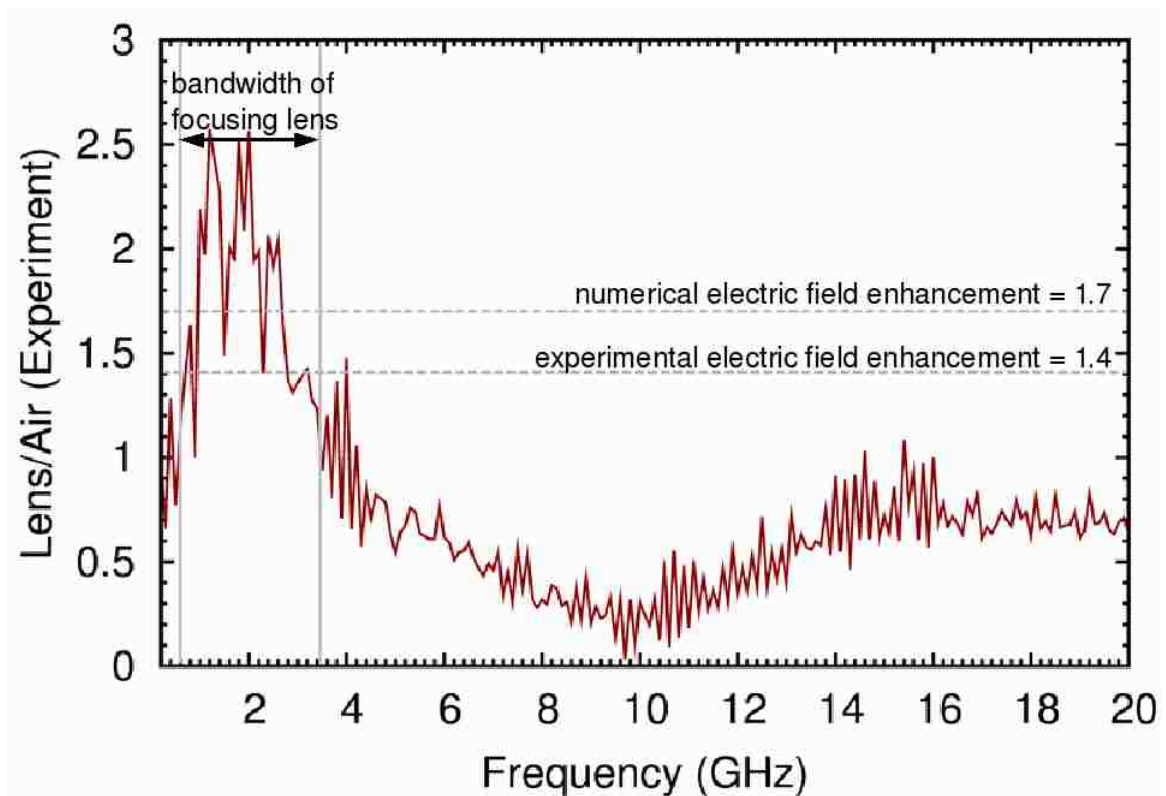


Figure 4.17: Ratio of magnitude of Fourier transform of the focal impulse waveform from experiments.

The curve in Fig. 4.17 is compared to similar results obtained from simulations in Fig. 4.18. The (average) amplification is approximately 1.77 (dotted gray line) upto a frequency of 10 GHz, as expected, since the lens materials are assumed lossless and dispersionless in the simulations. This is closer to that obtained from the ratio of the peak focal electric fields, i.e.,  $10.725/6.247 = 1.717$ . Therefore, the analogous experimental enhancement,  $7.66/5.44 = 1.408$ , is considered in Fig. 4.17.

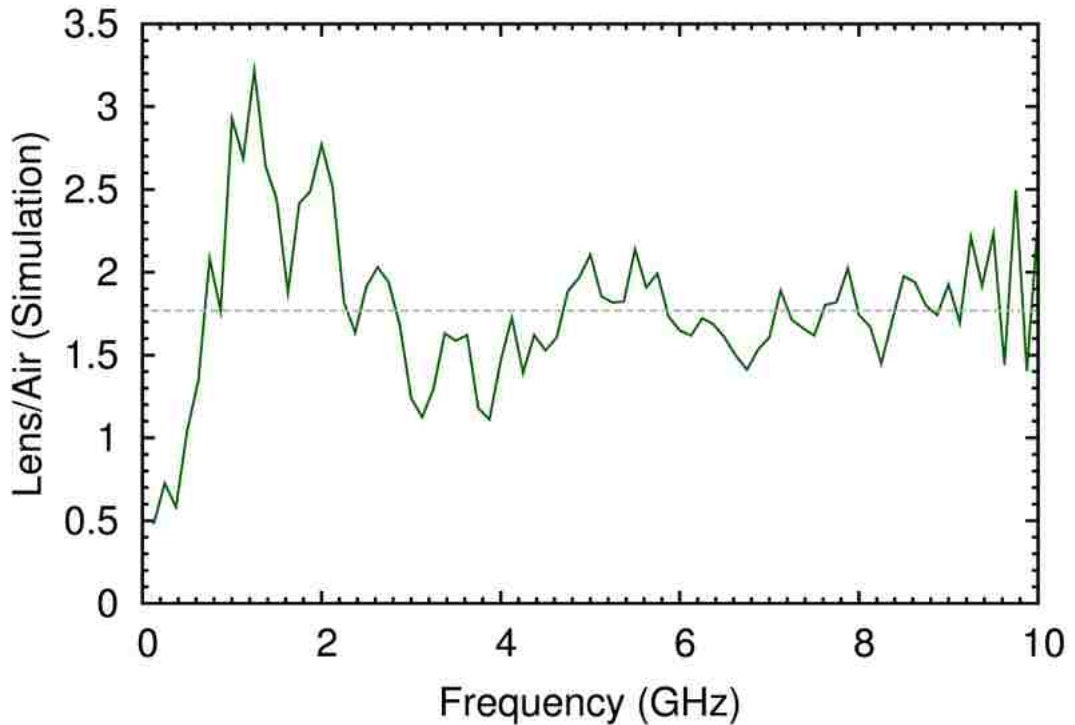


Figure 4.18: Ratio of magnitude of Fourier transform of the focal impulse waveform, from simulations, for an input pulse with 100 ps rise time. The dotted gray line is 1.77, the electric enhancement obtained with the lens.

#### 4.4.4 Beam width (Spot size)

As explained in Ch. 3, the lens reduces the beam width (spot diameter) by a factor of  $\epsilon_{rt}^{1/2} = 8.2^{1/2} = 2.86$  in the target medium. This is desirable in the treatment of skin cancer (melanoma). Figure 4.19 compares the experimental results of the beam width in air and in the lens. The half-power width in air is 4.397 cm and in the lens

it is 1.836 cm. Therefore, the spot size in the lens is reduced by a factor of  $4.397 \text{ cm}/1.836 \text{ cm} \approx 2.395 \approx \epsilon_{rt}^{1/2} = 8.2^{1/2}$  as obtained from numerical simulations.

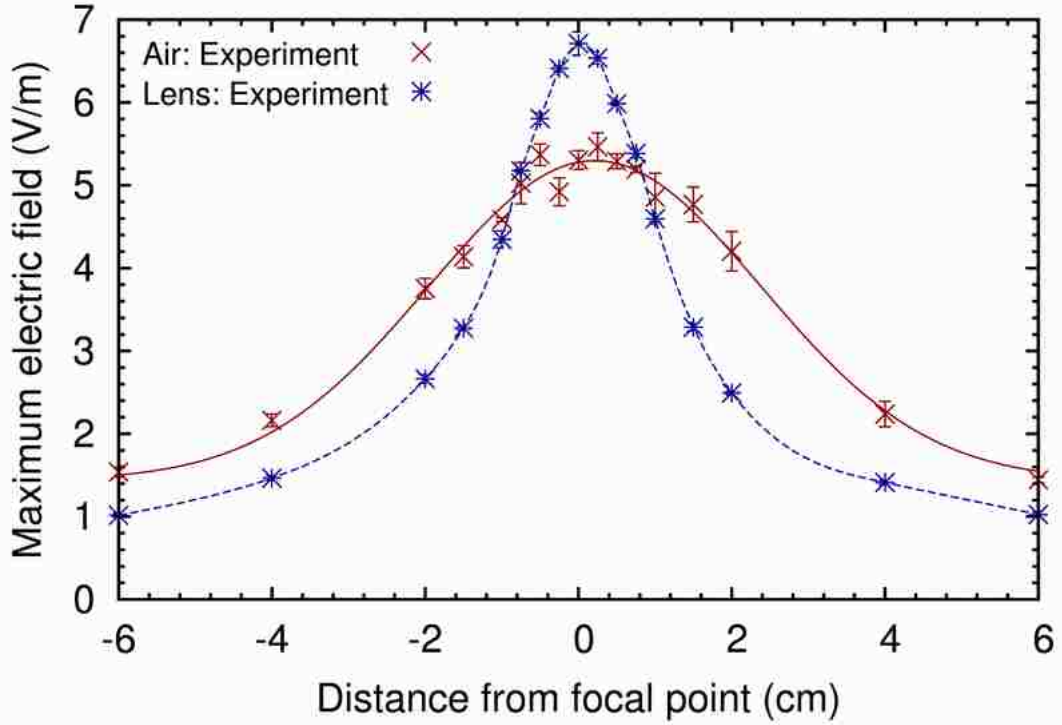


Figure 4.19: Comparison of experimental results of beam width in air and in lens.

Figure 4.20 and Fig. 4.21 compare simulation and experimental results of the beam width in air and in the lens. Errors in the experimental data are of the order of the spot size. As seen in Fig. 4.20, the simulation and experiment results of the spot size in air agree very well. One observes that the geometric focal point in the lens is shifted to the right by approximately  $x = +0.25 \text{ cm}$ . The discrepancy between the experimental and numerical results in Fig. 4.21 is due to losses occurring in the lens materials; the width of the pulse emerging from the lens is 127.5 ps which results in a larger spot size.

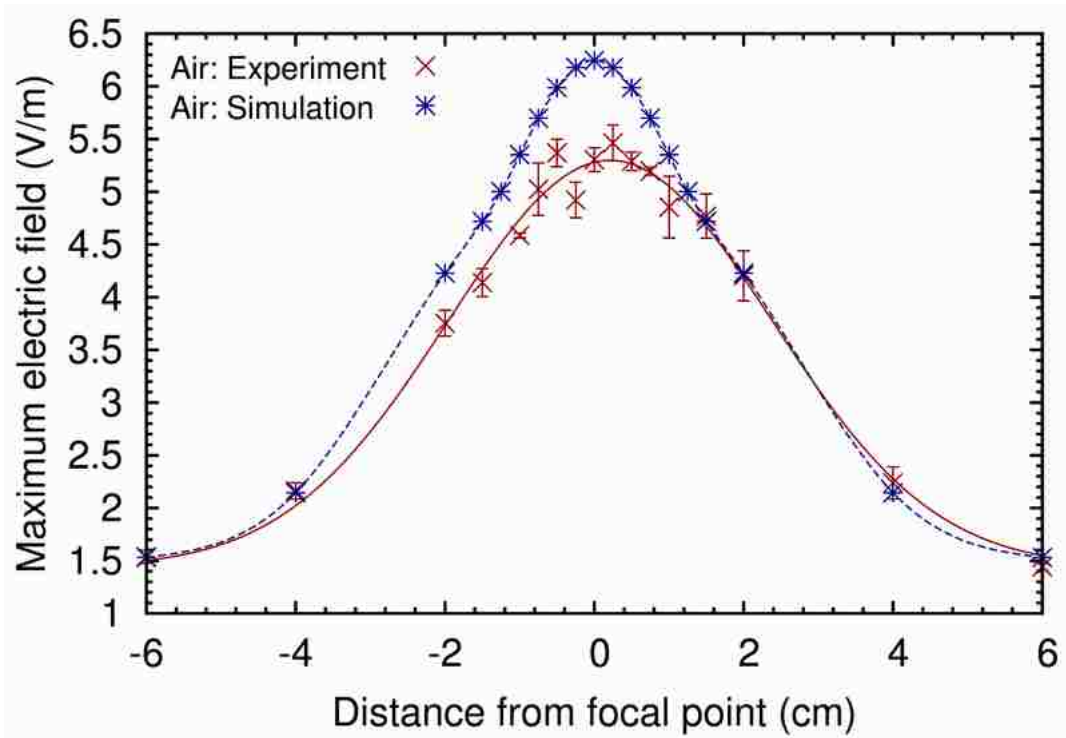


Figure 4.20: Comparison of simulation and experiment results of beam width in air.

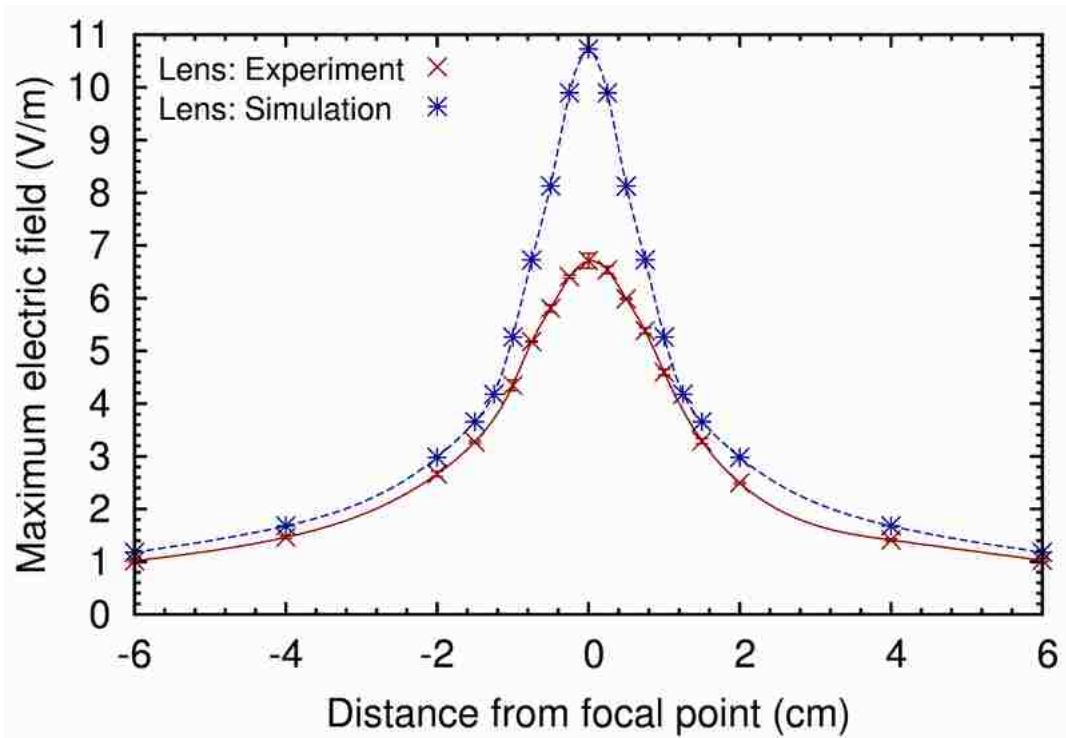


Figure 4.21: Comparison of simulation and experiment results of beam width in lens.



Table 4.2 summarizes and compares the spot sizes obtained from experiments and simulations.

Table 4.2: Beam width of electric field in air and with focusing lens from Fig. 4.19 and Fig. 4.20

	Simulation	Experiment
No lens (EFSS <sub>NL</sub> in cm)	3.61	4.397
With Lens (EFSS <sub>WL</sub> in cm)	1.19	1.836
EFSS <sub>WL</sub> /EFSS <sub>NL</sub>	3.04	2.395

The spot sizes in Fig. 4.19, Fig. 4.20 and Fig. 4.21 are obtained by taking the peak electric fields, of the focal waveforms, at the respective positions. As explained in the previous section, a more accurate measurement is to reference the peak impulse amplitude with respect to the start and end of the impulse event. This increases the peak amplitude by

$$\Upsilon = \left| \frac{E_s^i + E_e^i}{2} \right|. \quad (4.22)$$

To accurately determine the spot size,  $\Upsilon$  must be calculated for the impulse waveform at each position along  $x$ . However, as a first approximation, the  $\Upsilon$  for the impulse waveforms at all  $x$  positions may be assumed to be identical to that at the focal point. In Fig. 4.22, Fig. 4.23 and Fig. 4.24 the peak electric fields are increased by  $\Upsilon = 0.1$  V/m in air [43] and  $\Upsilon = 1.1$  V/m inside the lens.

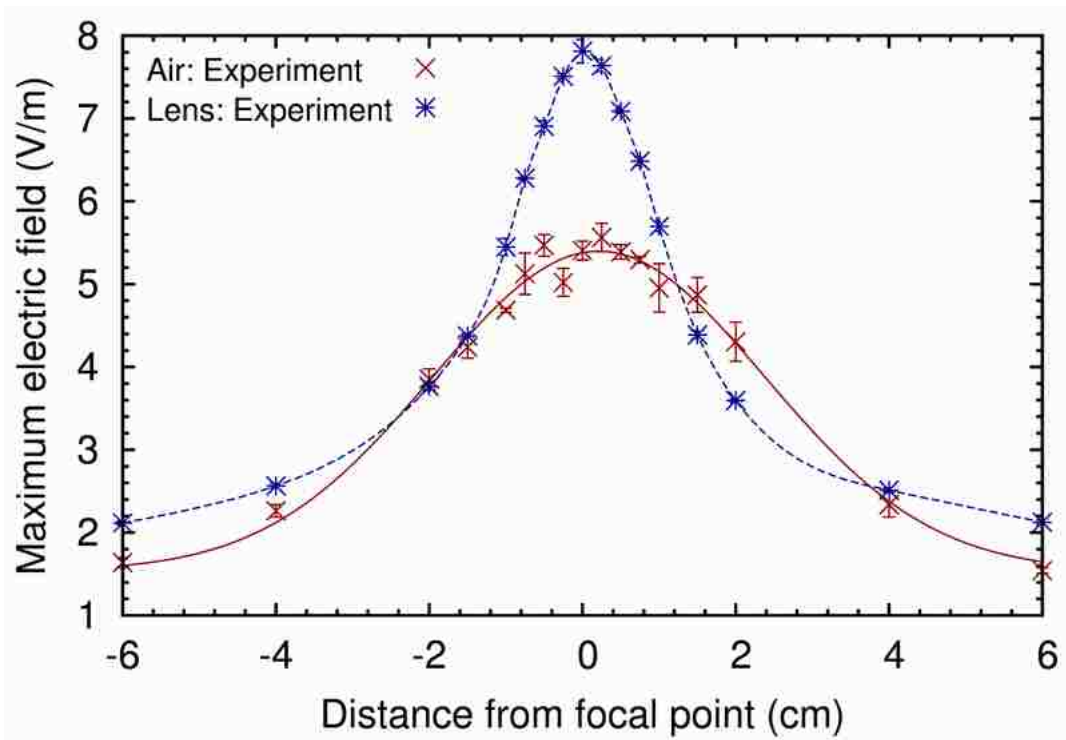


Figure 4.22: Comparison of experimental results of beam width in air and in lens.

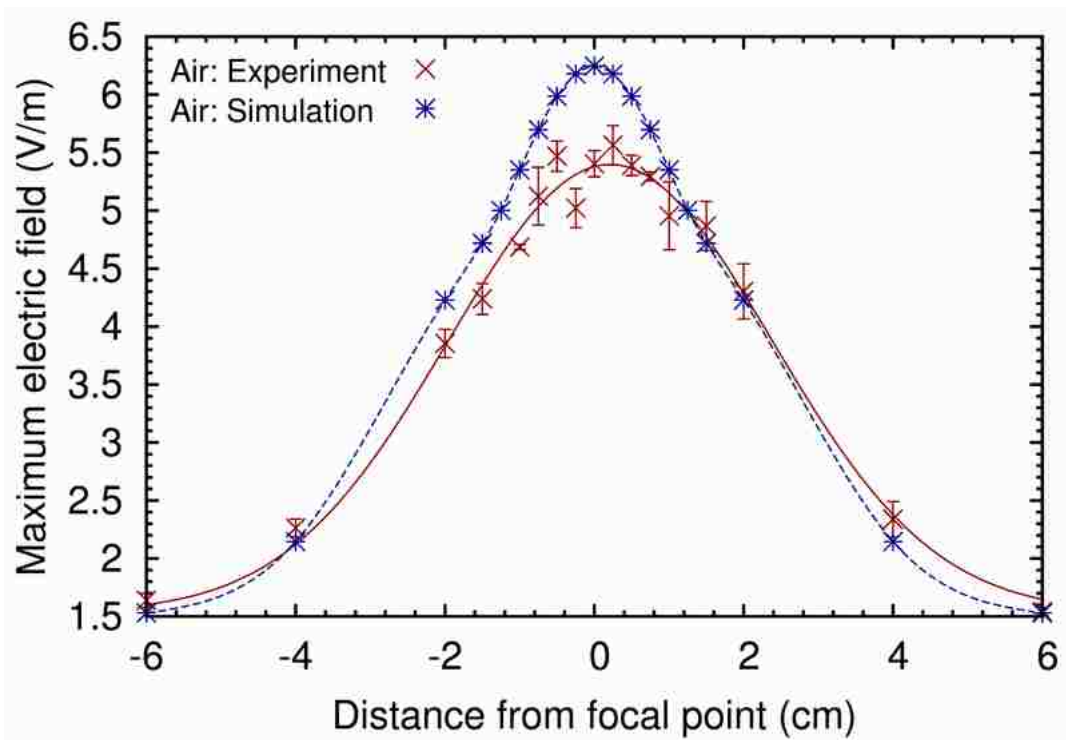


Figure 4.23: Comparison of numerical simulation and experimental results of beam width in air.

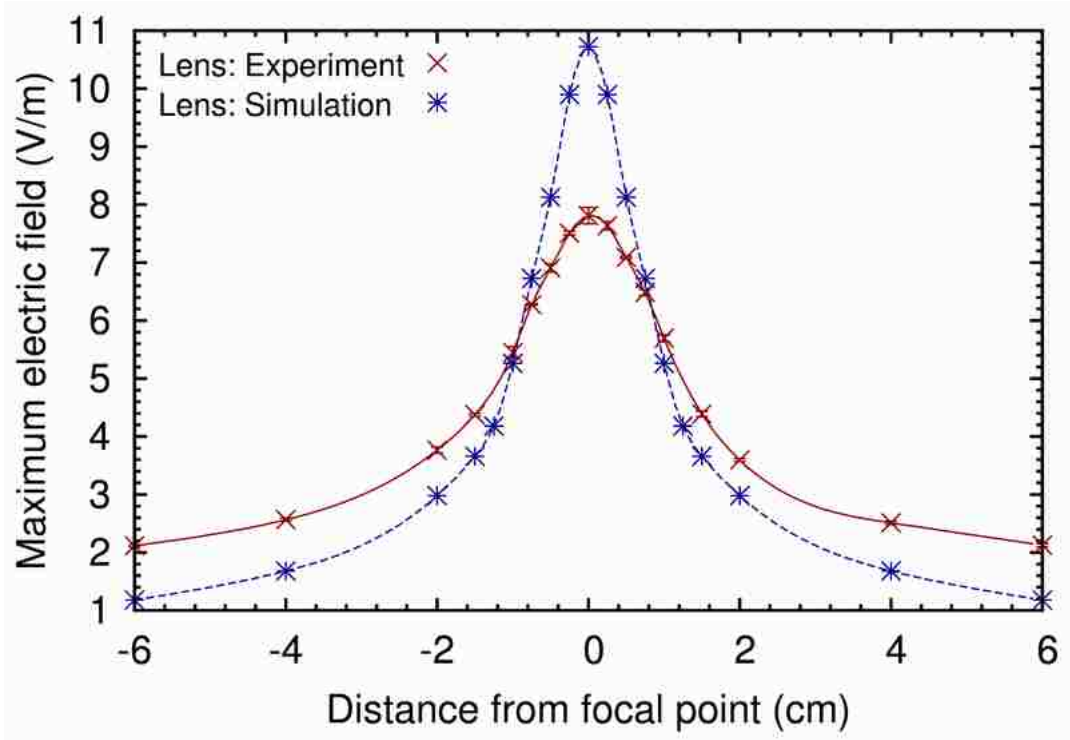


Figure 4.24: Comparison of numerical simulation and experimental results of beam width in lens.

Table 4.3 summarizes and compares the spot sizes obtained from experiments and simulations after the peak electric field amplitudes have been increased by  $E^I$ .

Table 4.3: Beam width of electric field in air and with focusing lens from Fig. 4.23 and Fig. 4.24

	Simulation	Experiment
No lens (EFSS <sub>NL</sub> in cm)	3.61	4.451
With Lens (EFSS <sub>WL</sub> in cm)	1.19	2.036
EFSS <sub>WL</sub> /EFSS <sub>NL</sub>	3.04	2.187

## 4.5 Comparison of Measurements with and without the 100 ps Filter

Initial experimental results were obtained without using the 100 ps filter [1]. To remain consistent with our analytical calculations and numerical simulations, which assume an input with a 100 ps rise, the experimental focal impulse waveform in air was rescaled so that its FWHM was 100 ps. Consequently, the beam width in air had to be rescaled in a similar manner.

The rescaling technique assumes that the experimental, Gaussian-shaped, impulsive part of the waveform can be analytically approximated by an ideal rectangular pulse, as shown in the sketch in Fig. 4.25 (the areas under all the curves are the same). The width of the rectangular pulse is identical to the FWHM of the impulse. Due to these inherent approximations, the rescaling method is accurate only to first order as it does not take into account all components of the response in the frequency spectrum.

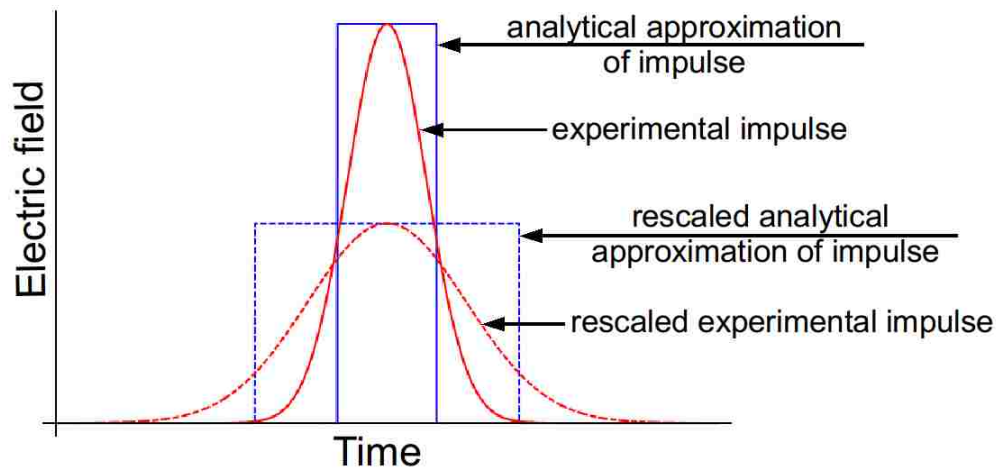


Figure 4.25: Method used to rescale the experimental focal impulse waveform in air [1].

Nevertheless, it is interesting to compare the rescaled focal waveform and the focal waveform in Sec. 4.3 (obtained using the 100 ps filter) in air. The electric field

focal waveform with the filter is compared to that without the filter ( $t_{\text{mr}} = 45$  ps) and the rescaled waveforms from [1] in Fig. 4.26. The plots have been time shifted for clarity. The peak focal impulse amplitude,  $E_{\text{max}}$ , without the filter is 11.33 V/m and that of the rescaled waveform is 5.67 V/m [ $11.33 \cdot (45 \text{ ps}/100 \text{ ps})$ ]. One notes that the peak impulse amplitude of the rescaled waveform and that obtained with the filter are almost the same.

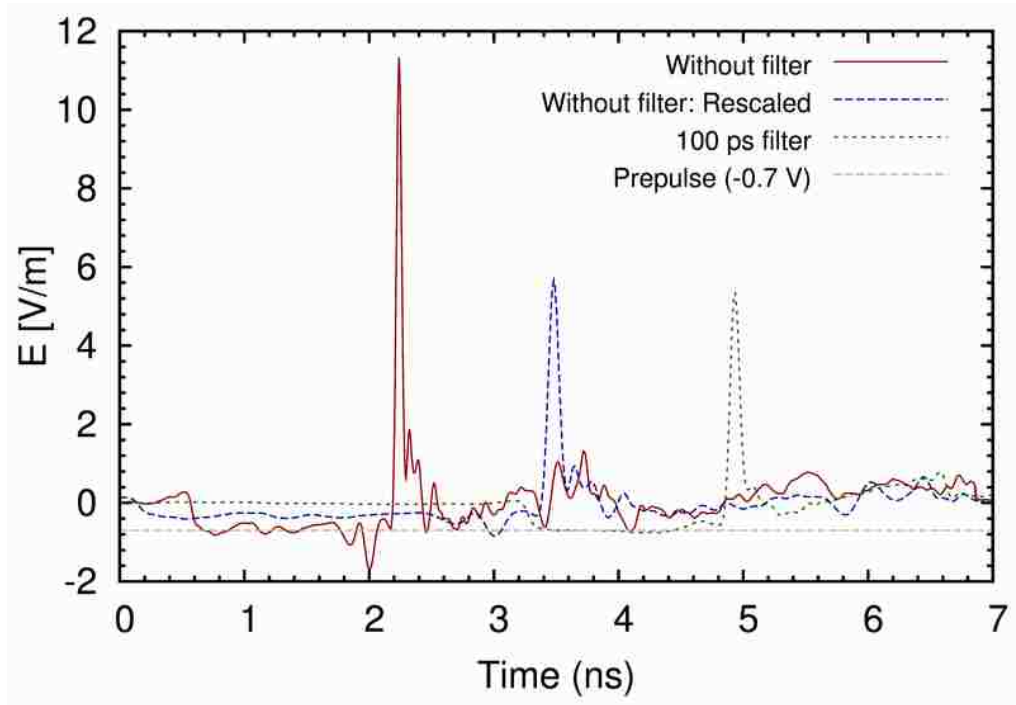


Figure 4.26: Comparison of the electric field focal impulse waveforms with and without the 100 ps filter. The analytical prepulse (-0.7 V) is plotted for reference.

Although the amplitudes of the waveforms with and without the filter are identical, Fig. 4.26 does not show the filtering of lower frequencies due to the focusing action of the lens. The FWHM of the rescaled waveform is assumed to be 100 ps. However, the lower FWHM of 85 ps obtained with the filter indicates that this assumption is not strictly valid.

Information on the focal waveforms and beam widths with and without the 100 ps filter in the focusing lens are compared in [1, 43] in Table. 4.4. The results are

almost identical.

Table 4.4: Comparison of focal waveforms and beam widths with and without the 100 ps filter in the focusing lens

	Without filter	With filter
Peak focal electric field ( $E_{\max}$ in V/m)	7.245	7.66
FWHM (ps)	130	127.5
Beam width (in cm)	1.83	1.836

## 4.6 Accuracy of Measurements with D-dot Probe

There is a small (air) gap between the edge of the ground plane and probe in Fig. 4.4 due to imperfect contact. Electric fields leaking through this gap reduce the voltage amplitude measured by the D-dot probe. One method to mitigate this problem is to cover the edge of the probe and ground plane with metal tape as shown in Fig. 4.27.

It was observed that the electric field amplitude with the tape is approximately 11% higher when compared to that without the tape [1]. The tape was not used in any of the measurements presented in this chapter. Errors in peak electric field amplitudes, in air and in the lens are therefore relative. The absolute values of the fields should be approximately 11% higher. The error bars in Fig. 4.19 indicate that the repeatability error in our experiments is less than 5%.

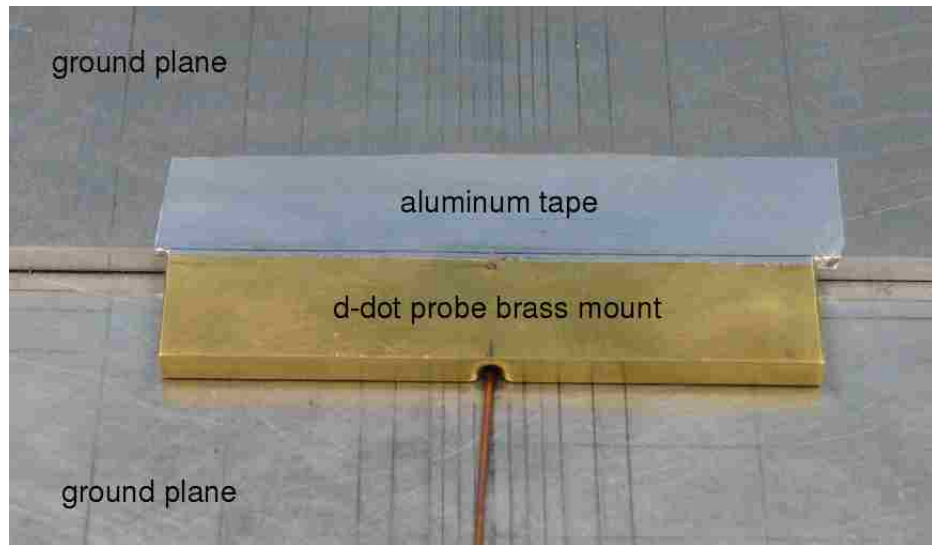


Figure 4.27: Metal tape covering gap between probe edge and ground plane to reduce leaking of electric fields through the gap.

## 4.7 Summary

The design, simulation and experiments of a PSIRA and focusing lens system have been presented. A 100 ps pulse, launched from the first focal point, is focused on to a biological target located at the second focal point. The focusing lens, a radially inhomogeneous, log-periodic, hemispherical, graded, dielectric lens, is used to better match the focused fields into the biological medium, for example, for melanoma treatment. This lens also increases the amplitude and reduces the spot size of the focused electric fields, both of which are desirable.

Electromagnetic scaling relationships presented in Ch. 3 extend the analytical considerations in [17]. Electric and magnetic enhancement factors are obtained in terms of the relative permittivity of the target medium,  $\epsilon_{rt}$ . It is found that the displacement enhancement varies as  $\epsilon_{rt}^{5/4}$ , which is extremely advantageous as it is the electric flux density that acts on the cancer cells. Scaling of electromagnetic parameters in results from numerical simulations agree very well with analytical calculations. As such, numerical simulations provide results which are otherwise

difficult to obtain analytically.

A D-dot probe, with a two-dimensional tear-drop shaped electrode, was used to make our measurements in the target medium and in air. The experimental focal waveforms and beam widths, in air and in the lens, at the second focal point, agree well with theory. However, losses in the lens materials reduce the amplitude and broaden the impulse which is undesirable. A comparison of numerical simulation and experimental results in the frequency domain reveals that the focusing lens acts as a bandpass filter from 0.4 GHz to 3.4 GHz.

Future work should primarily focus on testing and identifying materials with lower losses and dispersion, in the time scale of our interest ( $\leq 100$  ps), for use in the focusing lens. One method to improve the lens materials is to use an artificial dielectric consisting of a random array of short, thin wires ( $\epsilon_r \rightarrow \infty$ ) embedded in a relatively low dielectric medium [46]. This would enable one to obtain higher impulse amplitudes and smaller spot sizes, approaching the results obtained in our numerical simulations.

Ultimately we would like to use a 10 layer lens to match into a dielectric medium with  $\epsilon_r = 81$ . Lower loss and dispersion materials become even more important in this context. Moreover, measurements of fast pulses ( $\leq 100$  ps) in such high dielectric media will pose several new and interesting challenges. Little or no work has been previously done in this area with a focus on biological applications. A more in-depth study of lens materials and measurement techniques is therefore imperative before a working prototype can be deployed.



## Chapter 5

# Switch System and Launching Lens Designs

*“We haven’t got the money, so we’ve got to think!”*

*- Ernest Rutherford*

For input voltages of 100 kV or more, a switch system and “launching” lens are necessary to effectively launch a spherical TEM wave from the first focal point. The switch system consists of switch cones, a pressure vessel and a gas (typically hydrogen) chamber. The design and numerical simulations of such a switch system and launching lens are presented in this chapter. Although the input for the numerical simulations is only 1 V, analogous designs for the prototype IRA tested at high-voltages ( $> 100$  kV) [47] indicate that similar results can be expected for the switch system configurations in this chapter.

## 5.1 Initial Launching Lens Designs

The initial approach to the design of a launching lens followed methodologies similar to those used in the prototype IRA [48]. This approach assumes that the feed point (switch center) and the first focal point are spatially isolated, Fig. 5.1. The objective of the lens design is to ensure that within the lens a spherical TEM wave is centered on the feed point. However, outside the lens an approximate spherical TEM wave is centered at the first focal point. Uniform and non-uniform designs were explored and are summarized below.

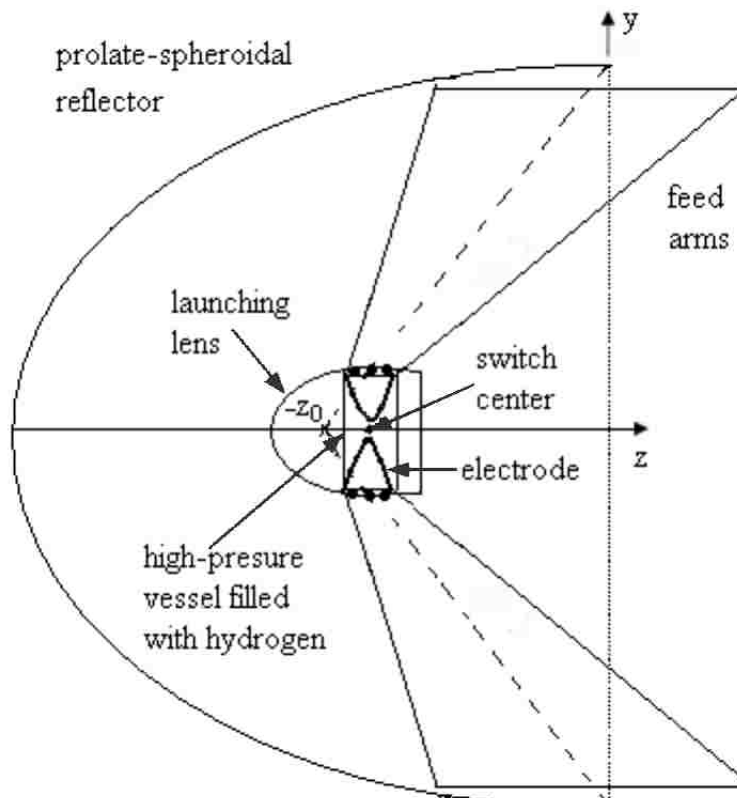


Figure 5.1: Schematic of launching lens and switch system. The feed point (switch center) and first focal point ( $-z_0$ ) are spatially isolated. [3].

### 5.1.1 Uniform lens design

Analytical calculations defining the boundary of a dielectric lens, with a fixed relative permittivity, are detailed in [49]. These equations are derived using high-frequency (optical) approximations. It is shown that the dielectric constant required for such a design must be greater than 25. This constraint is a serious drawback since materials with such high dielectric constants have a large loss and dispersion.

### 5.1.2 Non-uniform lens design

Lower dielectric constants can be obtained by designing a lens in which the  $\epsilon_r$  varies (discretely) across the lens boundary. To simplify the analysis, the lens is assumed to be a body-of-revolution. An analytically-aided-simulation approach is used; The lens boundary, dielectric constants of various layers and thicknesses of the layers are first estimated analytically. Simulations are then used to examine the time-of-arrival of electric fields on a spherical surface to ensure that a spherical TEM wave originates from the first focal point. This procedure is iterated until the design is achieved within the desired tolerance. Two designs are described below, the planar and the conical [50–53].

#### 5.1.2.1 Planar design

The planar lens is one in which the relative permittivity of the layers varies along the (rotational) axis of the lens. The design is log periodic, i.e., all layers have the same electrical width. 3-layer and 6-layer designs, where the  $\epsilon_r$  varied from 1.4 to 8.0 across the layers, were investigated. Simulations indicated that the time spread in the rays originating from the source was over 100 ps. This time spread is highly undesirable as it indicates that the spherical wavefront is distorted well beyond the

acceptable tolerance of 20 ps.

### 5.1.2.2 Conical design

In this design, the relative permittivity of the layers is a function of the polar angle,  $\theta$ . Simulation results from a 7-layer configuration, where the  $\epsilon_r$  varied from 2.25 to 6.25 across the layers, were almost identical to the planar design.

Due to the very large distortion of the spherical wave, the planar and conical designs were not iterated as this would have been too resource intensive. The large distortion in the spherical wavefront could be due to many reasons, such as the optical approximations breaking down at lower frequencies, reflections from inner layers etc. This approach was abandoned in favor of the simpler designs described in the following sections.

## 5.2 Investigation of Various Switch Configurations

In the design of the launching lens described above it was assumed that the feed point and first focal point were spatially isolated. This assumption imposed a severe constraint on the lens design. The problem is greatly simplified if the geometric center of the feed point is made to coincide with the first focal point. Before proceeding to the launching lens designs, various switch configurations are described where the geometric center of the switch cones is the first focal point. The focal impulse amplitude,  $E_{\max}$ , and beam width were compared for the following switch configurations [4],

1. Four Feed Arms with Switch Cones (4FASC): A  $200\ \Omega$  bicone switch, of height 1.0 cm, centered at the first focal point transitions to the feed-arms of the PSIRA, Fig. 5.2. The connection between the switch cone base and the feed-arms is called the loft connection.

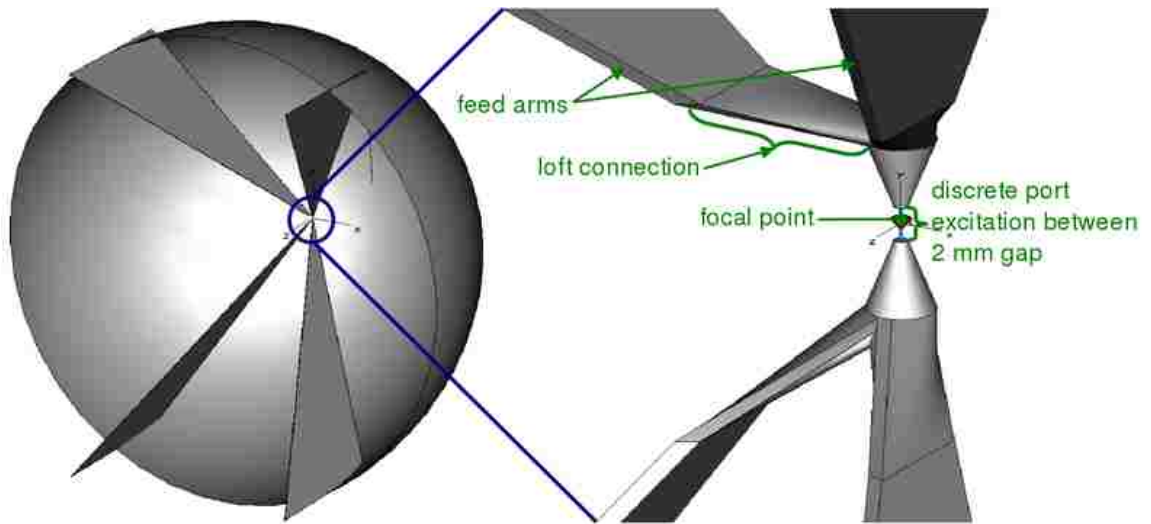


Figure 5.2: Four feed arms with switch cones (4FASC) [4].

2. Truncated Four Feed Arms with Switch Cones (T4FASC): This configuration is identical to the 4FASC except that the feed arms are truncated at a distance of 19 cm from the first focal point, Fig. 5.3.

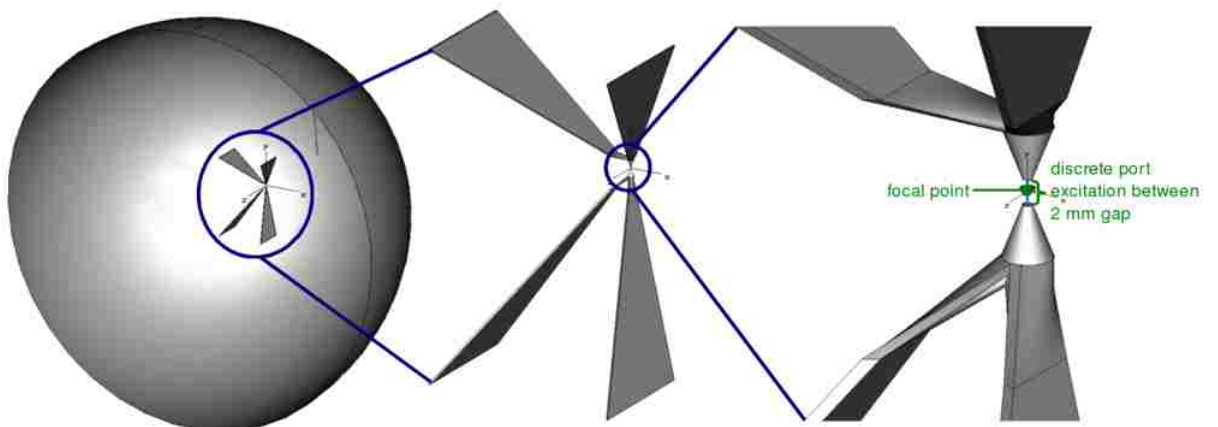


Figure 5.3: Truncated four feed arms with switch cones (T4FASC) [4].

One notes that the rise time of  $t_\delta = 100$  ps corresponds to a physical distance of  $ct_\delta = 3$  cm (in air). Therefore, a switch of appropriate dimensions can also serve as a guiding structure. Two such configurations were studied:

3. Vertical Bicone Switch (VBCS): A vertical bicone is used as the source where the height of each cone is 6.0 cm, Fig. 5.4. This structure also serves to guide the spherical TEM waves originating from the feed point. The impedance of the cones was varied.

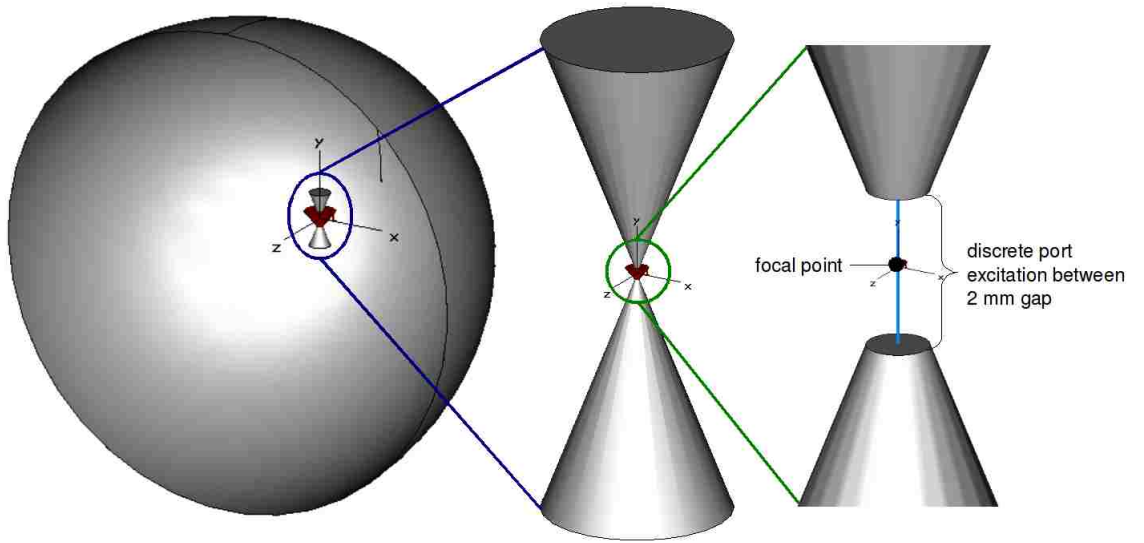


Figure 5.4: Vertical Bicone Switch (VBCS) [5].

4. Slanted Four-Cone Feed Arms (S4CFA): This structure is almost identical to the T4FASC except that the feed arms are replaced by  $200 \Omega$  cones, Fig. 5.5. Each cone is 6.0 cm in height.

For complete details of the geometry for the switch configurations the reader is directed to [4].

Results from numerical simulations for  $E_{\max}$  and the spot size, at the second focal point, for the various configurations are summarized in Table 5.1.

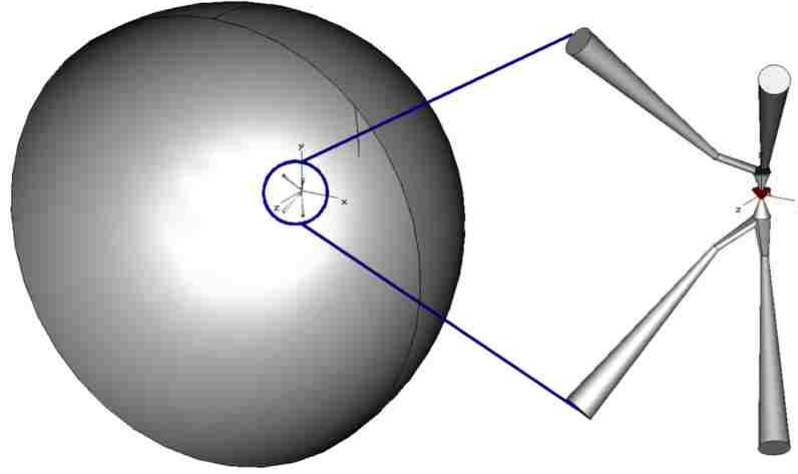


Figure 5.5: Slanted Four-Cone Feed Arms (S4CFA) [4].

Table 5.1: Peak focal impulse amplitude and beam width for various switch configurations.

Configuration	$E_{\max}$ (V/m)	Spot size (cm)
VBCS-50	8.117	3.737
<b>VBCS-75</b>	<b>6.727</b>	<b>3.894</b>
VBCS-100	5.619	4.065
VBCS-150	4.057	4.414
VBCS-200	3.144	4.455
4FASC	6.363	3.546
<b>T4FASC</b>	<b>7.217</b>	<b>3.889</b>
S4CFA	5.114	3.39

VBCS-Z denotes a vertical bicone switch with impedance  $2Z \Omega$ .

One finds the VBCS-75 and T4FASC designs to be the most promising. Both these configurations are easy to fabricate, yield a relatively high peak electric field and an acceptable spot size compared to the other configurations. Additionally, it is also found that the pre-pulse is shorter with these structures, compared to those in [1]. Therefore, these configurations are further considered for the launching lens designs in the following section.

## 5.3 Pressure Vessel Designs

The gas chamber, pressure vessel, and launching lens are necessary as, in the final experimental realization of the PSIRA, 100 kV or more will be applied across the switch gap. The gas chamber typically contains hydrogen or SF<sub>6</sub> under high pressure. In our designs, hydrogen is used as an example. As mentioned in the previous section, the location of the geometric center of the switch cones at the first focal point greatly simplifies the design. The design is further simplified if one considers the pressure vessel to serve the function of the launching lens. Then the switch system consists of only three components: 1) switch cones and guiding structures 2) hydrogen chamber (HC) and 3) pressure vessel (PV).

The pressure vessel may be cylindrical or spherical. The peak focal impulse amplitudes of the VBCS-75 configurations, with a spherical PV, were approximately 30% lower than the corresponding T4FASC designs. Therefore, numerical simulation results for only the T4FASC configuration with the spherical and cylindrical pressure vessel designs are presented here [54, 55].

### 5.3.1 T4FASC with a Spherical Pressure Vessel and Spherical Hydrogen Chamber (T4FASC-SPVSHC)

To provide structural support to the pressure vessel, a cylindrical support section (CSS), of height  $H_{\text{CSS}}$ , is added to the T4FASC design. The pressure vessel and the hydrogen chamber are spherical. The relative permittivity of the pressure vessel medium is assumed to be 3.7 [56, 57]. The impedance of the switch cones is 200  $\Omega$  in the pressure vessel medium, i.e., cone half-angle  $\theta = 45.58^\circ$ . A spherical container, with  $\epsilon_r = 2.25$  (transformer oil), surrounds the pressure vessel and is used to denote the oil “bath” that would be used in the final, practical design [54]. Fig. 5.6. shows



the side view of the various components of the switch system. Dimensions of these components are summarized in Table 5.2.

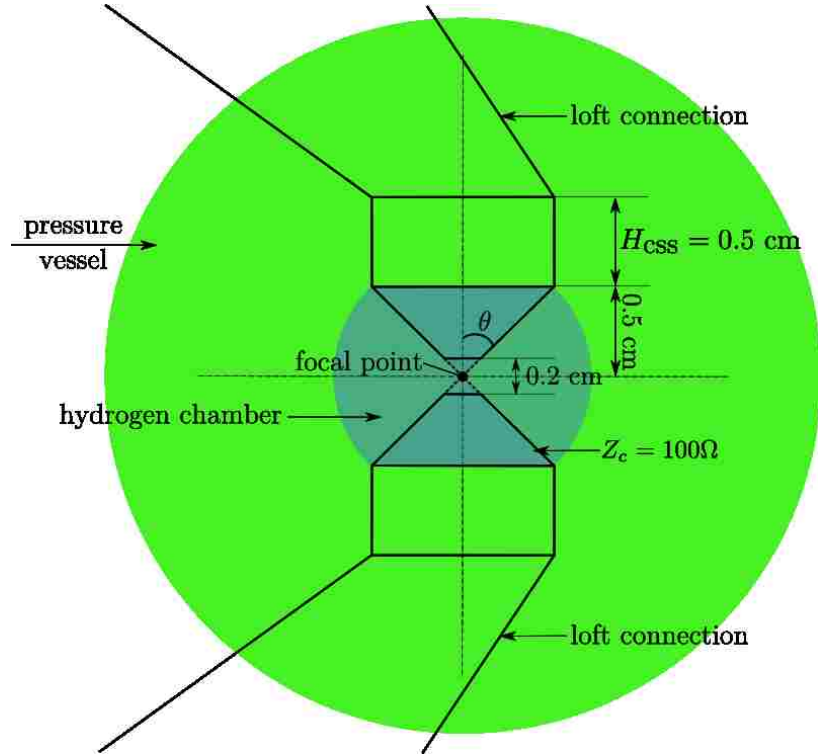


Figure 5.6: Side view of the T4FASC configuration with a spherical pressure vessel and spherical hydrogen chamber.

Table 5.2: Dimensions of switch system components for the T4FASC-SPVSHC design.

Component	Height (cm)	Radius (cm)
switch cone	$h = 0.5$	0.51
cylindrical support	$H_{\text{css}} = 0.5$	0.51
hydrogen chamber	—	0.71
pressure vessel	—	$r_{\text{pv}} = 2.0$
oil medium	—	$r_{\text{oil}} = 5.0$

Probes to monitor the time-of-arrival of electric fields were placed on a (virtual) sphere of radius 10 cm (near field). The normalized responses from these probes are shown in Fig. 5.7 (each response is normalized with respect to its maximum).

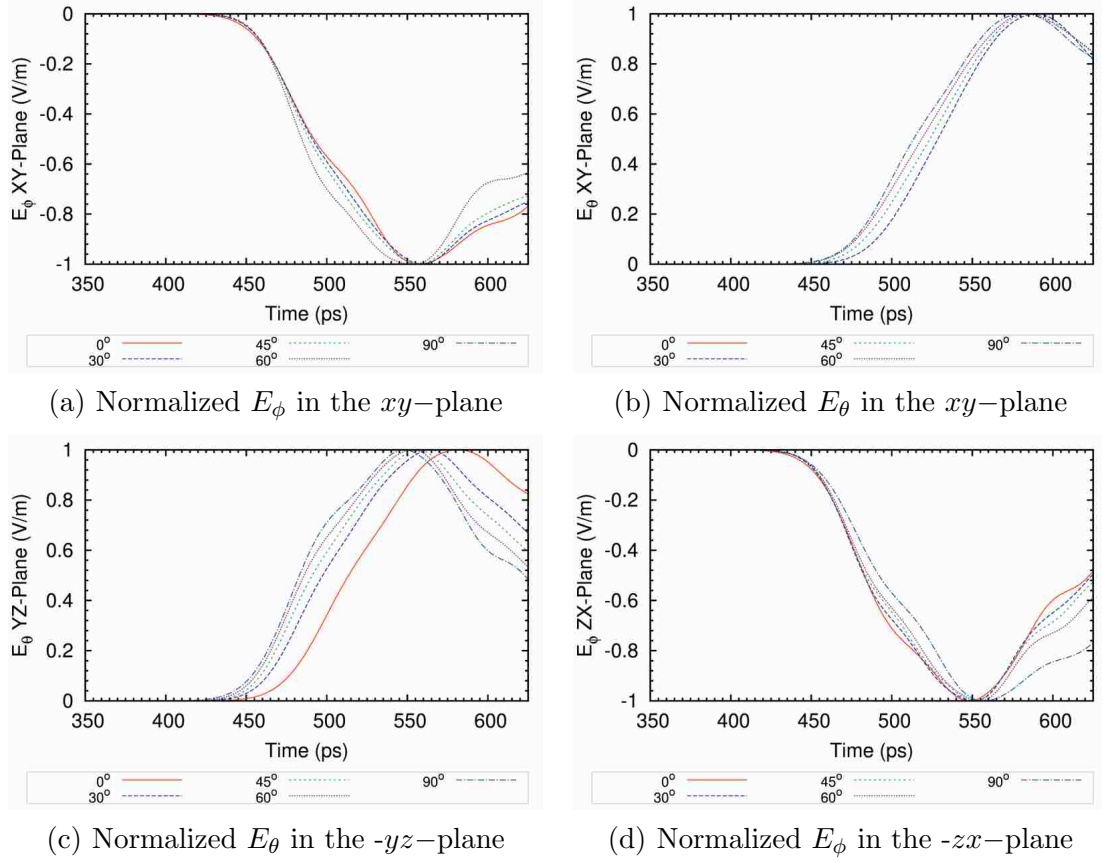


Figure 5.7: Normalized  $E_\theta$  and  $E_\phi$  components of the responses from the electric field probes on the  $xy$ ,  $-yz$  and  $-zx$  planes for the T4FASC-SPV configuration.

The  $E_\phi$  component in the  $-yz$ -plane and the  $E_\theta$  component in the  $-zx$ -plane are zero. The time spread in the electric fields is less than 20 ps, which is within the acceptable tolerance.

The focal waveform and spot size are shown in Fig. 5.8 and Fig. 5.9. These results indicate that the electric field is enhanced, compared to the T4FASC configuration in Table 5.1, with the pressure vessel by approximately 91%,  $E_{\max} = 13.76$  V/m, with a corresponding increase of only 19% in the spot diameter, beam width= 4.64 cm. The electric field is enhanced due propagation through the pressure vessel dielectric medium.

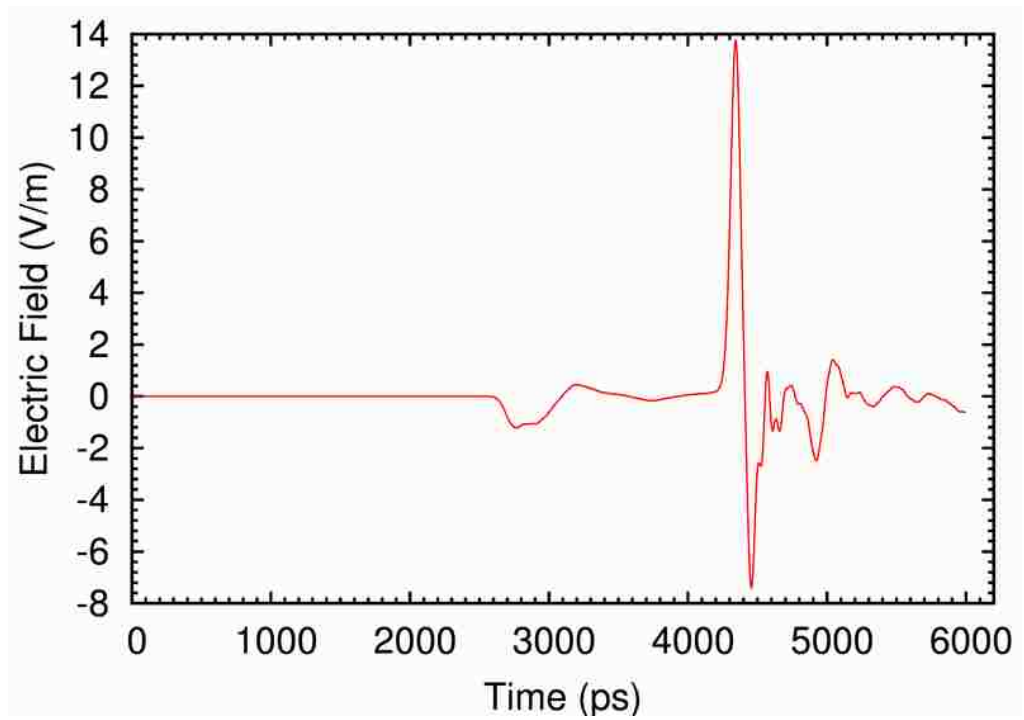


Figure 5.8: Electric field focal impulse waveform for the T4FASC-SPV configuration.

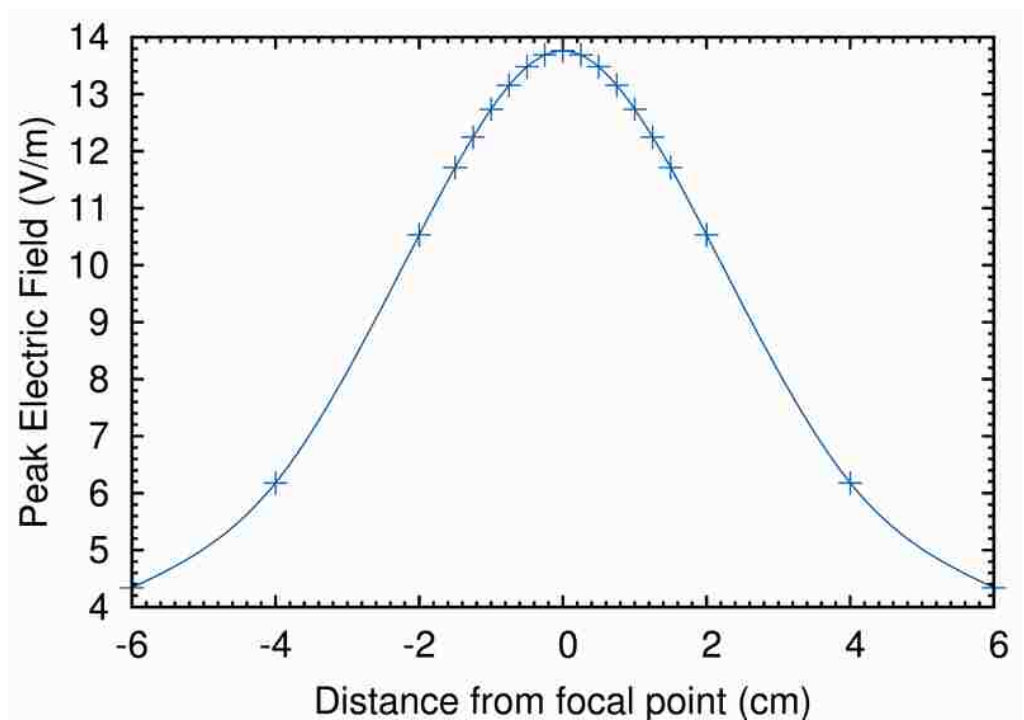


Figure 5.9: Spot size for the T4FASC-SPV configuration.

### 5.3.2 T4FASC with a Cylindrical Pressure Vessel and Cylindrical Hydrogen Chamber (T4FASC-CPVCHC)

Consider Fig. 5.10 which shows the setup of a cylindrical pressure vessel with a spherical launching lens. The objective is to determine the optimum dimensions of the pressure vessel which leads to a practically reasonable relative dielectric constant for the launching lens. The following notations are used [58],

$\epsilon_{r_{hc}}$	$= 1.0$	= relative permittivity of hydrogen chamber,
$\epsilon_{r_{pv}}$	$= 3.7$	= relative permittivity of pressure vessel,
$\epsilon_{r_{ll}}$		= relative permittivity of launching lens; to be determined,
$\theta$		= switch cone half-angle,
$\theta_i$		= incidence angle for ray $OA$ travelling from hydrogen chamber into pressure vessel,
$\theta_t$		= transmitted angle for ray $AB$ travelling from hydrogen chamber into pressure vessel,
$h_{sw}$		= height of switch cone,
$r_{sw}$		= radius of switch cone,
$h_{hc}$		= height of hydrogen chamber,
$r_{hc}$		= radius of hydrogen chamber,
$h_{pv}$		= (half-)height of pressure vessel,
$r_{pv}$		= radius of pressure vessel,
$r_{ll}$		= radius of spherical launching lens,
$h_{swgap}$		= height of switch gap.

For a  $200 \Omega$  bicone switch immersed in the pressure vessel medium,  $Z_c = (200 \Omega / \sqrt{\epsilon_{r_{pv}}})$ . Therefore, the half-angle of the switch cones is  $\theta = \frac{\pi}{2} - \theta_i = 45.58^\circ$ .

We require the ray travelling along the edge of the switch cone, ray  $OA$ , to be refracted such that it takes path  $AB$  where  $B$  is the edge of the pressure vessel.

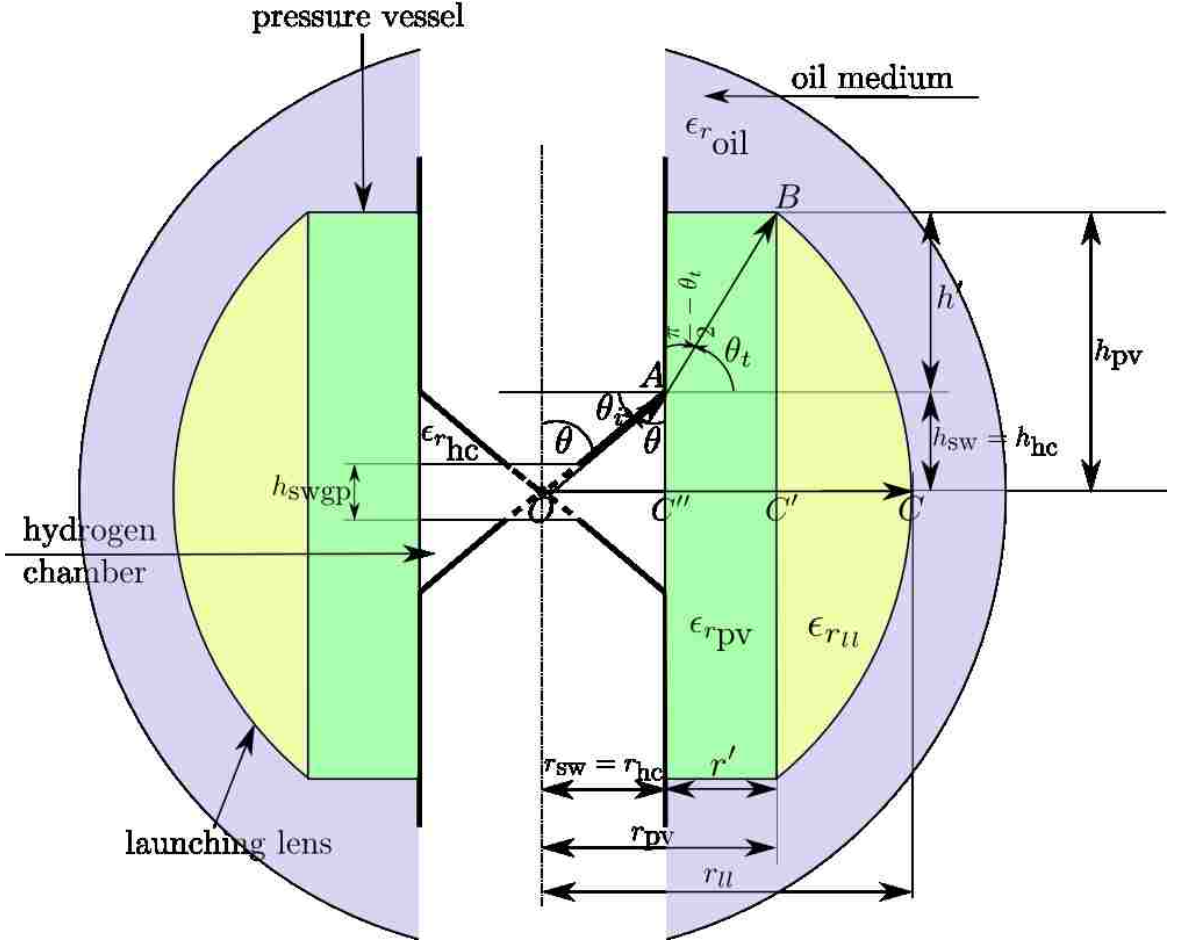


Figure 5.10: Diagram for cylindrical pressure vessel and launching lens calculations.

Therefore, we have from Snell's law,

$$\sqrt{\epsilon_{r_{hc}}}\sin(\theta_i) = \sqrt{\epsilon_{r_{pv}}}\sin(\theta_t) \Rightarrow \theta_t = \arcsin\left(\sqrt{\frac{\epsilon_{r_{hc}}}{\epsilon_{r_{pv}}}}\cos(\theta)\right). \quad (5.1)$$

Also,

$$\tan(\theta) = \frac{r_{hc}}{h_{hc}} = \frac{r_{sw}}{h_{sw}} \Rightarrow h_{hc} = r_{hc} \cot(\theta), \quad (5.2)$$

$$\tan(\theta_t) = \frac{h'}{r'} \Rightarrow \theta_t = \arctan\left(\frac{h'}{r'}\right). \quad (5.3)$$

Further,

$$r' = r_{\text{pv}} - r_{\text{hc}} = \text{“thickness” of the pressure vessel}, \quad (5.4)$$

$$h' = h_{\text{pv}} - h_{\text{hc}} = h_{\text{pv}} - r_{\text{hc}} \cot(\theta). \quad (5.5)$$

Substituting (5.4) and (5.5) in (5.3),

$$\theta_t = \arctan \left( \frac{h_{\text{pv}} - h_{\text{hc}}}{r_{\text{pv}} - r_{\text{hc}}} \right). \quad (5.6)$$

From (5.1) and (5.6)

$$\arctan \left( \frac{h_{\text{pv}} - h_{\text{hc}}}{r_{\text{pv}} - r_{\text{hc}}} \right) = \arcsin \left( \sqrt{\frac{\epsilon_{r_{\text{hc}}}}{\epsilon_{r_{\text{pv}}}}} \cos(\theta) \right) \quad (5.7)$$

$$\Rightarrow \frac{h_{\text{pv}} - r_{\text{hc}} \cot(\theta)}{r_{\text{pv}} - r_{\text{hc}}} = \tan \left( \arcsin \left( \sqrt{\frac{\epsilon_{r_{\text{hc}}}}{\epsilon_{r_{\text{pv}}}}} \cos(\theta) \right) \right). \quad (5.8)$$

Therefore, the height of the pressure vessel can be determined as a function of its radius, i.e.,

$$h_{\text{pv}} = [r_{\text{pv}} - r_{\text{hc}}] \tan \left( \arcsin \left( \sqrt{\frac{\epsilon_{r_{\text{hc}}}}{\epsilon_{r_{\text{pv}}}}} \cos(\theta) \right) \right) + r_{\text{hc}} \cot(\theta). \quad (5.9)$$

To determine the relative permittivity of the spherical launching lens, the equal time condition must be satisfied, i.e.,

$$OA\sqrt{\epsilon_{r_{\text{hc}}}} + AB\sqrt{\epsilon_{r_{\text{pv}}}} = OC''\sqrt{\epsilon_{r_{\text{hc}}}} + C''C'\sqrt{\epsilon_{r_{\text{pv}}}} + C'C\sqrt{\epsilon_{r_{\text{ll}}}}. \quad (5.10)$$

From Fig. 5.10,

$$\begin{aligned} OC'' &= r_{\text{sw}} = r_{\text{hc}}, \\ \sin(\theta) &= \frac{OC''}{OA} \Rightarrow OA = \frac{r_{\text{hc}}}{\sin(\theta)}, \\ C''C' &= r' = r_{\text{pv}} - r_{\text{hc}}, \\ \sin(\theta_t) &= \frac{h'}{AB} \Rightarrow AB = \frac{h_{\text{pv}} - r_{\text{hc}} \cot(\theta)}{\sin(\theta_t)}, \\ OB^2 &= OC'^2 + C'B^2 \Rightarrow r_{\text{ll}} = \sqrt{r_{\text{pv}}^2 + h_{\text{pv}}^2}, \\ C'C &= r_{\text{ll}} - r_{\text{pv}} = \sqrt{r_{\text{pv}}^2 + h_{\text{pv}}^2} - r_{\text{pv}}. \end{aligned} \quad (5.11)$$

Substituting (5.11) in (5.10),

$$\begin{aligned} & \left[ \frac{r_{\text{hc}}}{\sin(\theta)} \right] \sqrt{\epsilon_{r_{\text{hc}}}} + \left[ \frac{h_{\text{pv}} - r_{\text{hc}} \cot(\theta)}{\sin(\theta_t)} \right] \sqrt{\epsilon_{r_{\text{pv}}}} = \\ & r_{\text{hc}} \sqrt{\epsilon_{r_{\text{hc}}}} + [r_{\text{pv}} - r_{\text{hc}}] \sqrt{\epsilon_{r_{\text{pv}}}} + \left[ \sqrt{r_{\text{pv}}^2 + h_{\text{pv}}^2} - r_{\text{pv}} \right] \sqrt{\epsilon_{r_{\text{ul}}}}. \end{aligned} \quad (5.12)$$

$\therefore \epsilon_{r_{\text{ul}}}$  is determined as

$$\epsilon_{r_{\text{ul}}} = \left[ \frac{[\csc(\theta) - 1] r_{\text{hc}} \sqrt{\epsilon_{r_{\text{hc}}}} + \left[ \frac{h_{\text{pv}} - r_{\text{hc}} \cot(\theta)}{\sin(\theta_t)} \right] - [r_{\text{pv}} - r_{\text{hc}}] \sqrt{\epsilon_{r_{\text{pv}}}}}{\sqrt{r_{\text{pv}}^2 + h_{\text{pv}}^2} - r_{\text{pv}}} \right]^2, \quad (5.13)$$

$$\epsilon_{r_{\text{ul}}} = \left[ \frac{[\csc(\theta) - 1] r_{\text{hc}} \sqrt{\epsilon_{r_{\text{hc}}}} + \left[ \frac{h_{\text{pv}} - r_{\text{hc}} \cot(\theta)}{\sqrt{\epsilon_{r_{\text{hc}}}/\epsilon_{r_{\text{pv}}}} \cos(\theta)} \right] - [r_{\text{pv}} - r_{\text{hc}}] \sqrt{\epsilon_{r_{\text{pv}}}}}{\sqrt{r_{\text{pv}}^2 + h_{\text{pv}}^2} - r_{\text{pv}}} \right]^2. \quad (5.14)$$

The use of a cylindrical pressure vessel mandates the need of cylindrical (guiding) structures over the switch cones as shown in Fig. 5.11. These cylindrical structures, of height  $H_{\text{css}}$ , are required to provide structural support to the pressure vessel. They also serve to guide the waves originating from the source. It is evident that  $H_{\text{css}}$  must be constrained such that  $H_{\text{css}} + h_{\text{sw}} \geq h_{\text{pv}}$ . For the discussion that follows, consider  $H_{\text{css}} + h_{\text{sw}} = h_{\text{pv}}$ , i.e., the cylindrical guiding structures end at the edge of the pressure vessel. Further, it is desired that the spherical TEM wave, of rise time  $t_\delta = 100$  ps, is guided by the switch cones, cylindrical support structures and the feed arms, i.e.,  $H_{\text{css}} + h_{\text{sw}} = h_{\text{pv}} < ct_\delta$ . If  $H_{\text{css}} + h_{\text{sw}} = h_{\text{pv}} > ct_\delta$ , the wave will be guided only by the switch cones and the cylinder and not by the feed arms. Let us assume for the calculations that follow that  $h_{\text{pv}} \leq 2.0$  cm =  $(2/3)ct_\delta$ .

The medium surrounding the switch, pressure vessel and launching lens is assumed to be oil,  $\epsilon_{r_{\text{oil}}} = 2.25$  as shown in Fig. 5.11. For a net increase in the transmission coefficient (“bump-up”), the relative permittivity of the launching lens must be constrained such that  $\epsilon_{r_{\text{oil}}} \leq \epsilon_{r_{\text{ul}}} \leq \epsilon_{r_{\text{pv}}} \Rightarrow 2.25 \leq \epsilon_{r_{\text{ul}}} \leq 3.7$ .

From (5.9) and (5.14) it is clear that there exists an  $r_{pv}$  and  $h_{pv}$  for which  $\epsilon_{ru} = \epsilon_{roil} = 2.25$ , i.e., the surrounding oil medium can be used as the launching lens. This obviates the need of a separate launching lens. We therefore have only the cylindrical hydrogen chamber, cylindrical pressure vessel and the surrounding oil medium in the design.

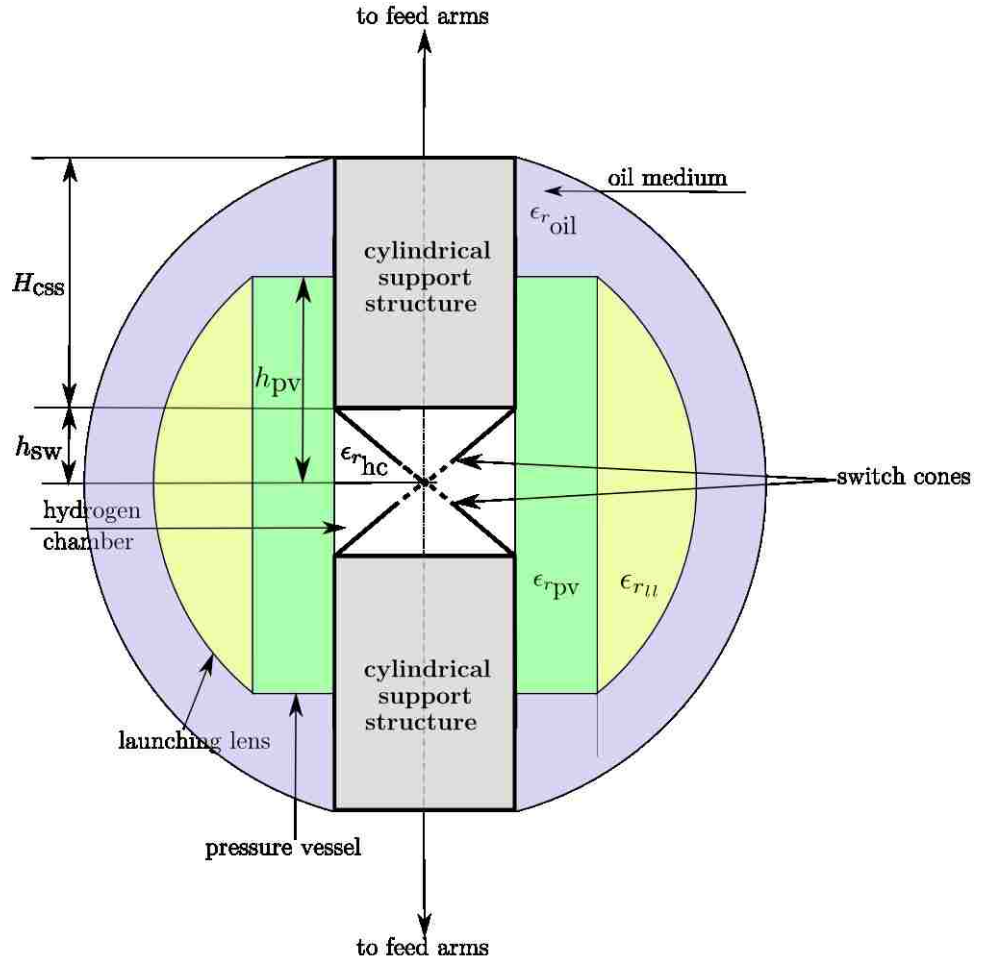


Figure 5.11: Cylindrical pressure vessel showing the need for a cylindrical guiding structure on top of the switch cones.

Fig 5.12 shows the side view of the various components of the switch system. The dimensions of the components are summarized in Table 5.3. The radius and height of the pressure vessel are determined using (5.9) and (5.14) such that the surrounding oil medium is the launching lens;  $r_{hc} = h \tan \theta = 0.5 \tan(45.58^\circ) = 0.51$



cm and  $\epsilon_{rll} = 2.25$  where  $\epsilon_{rll}$  is the relative permittivity of the launching lens. Note that  $h_{pv} = h + H_{css}$  in Table 5.3.

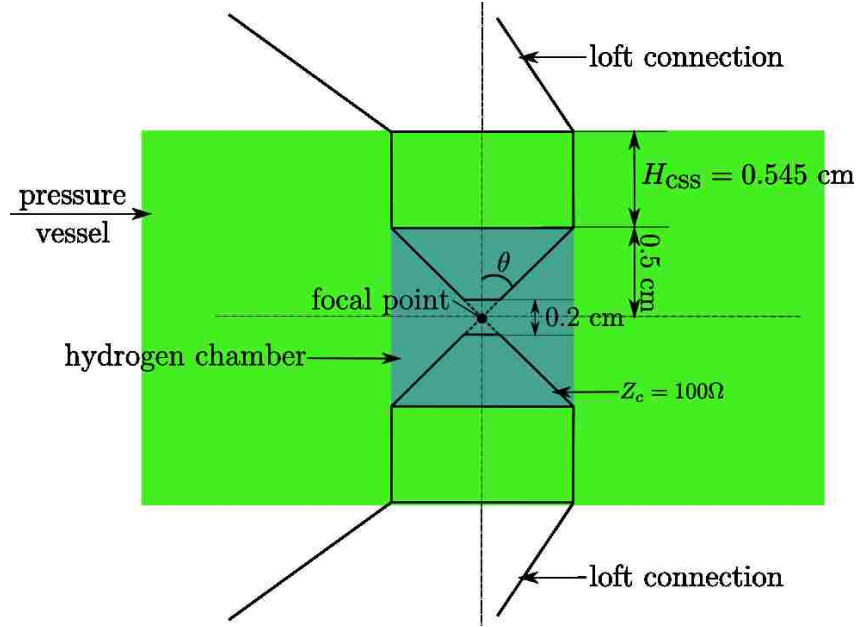


Figure 5.12: Side view of the T4FASC configuration with a cylindrical pressure vessel and cylindrical hydrogen chamber.

Table 5.3: Dimensions of switch system components for the T4FASC-CPVCHC design.

Component	Height (cm)	Radius (cm)
switch cone	$h = 0.5$	0.51
cylindrical support	$H_{css} = 0.545$	0.51
hydrogen chamber	$h_{hc} = 1.0$	0.51
pressure vessel	$h_{pv} = 1.045$	$r_{pv} = 1.905$
oil medium	—	$r_{oil} = 5.0$

The time-of-arrival of the electric fields on probes placed on a spherical surface of radius 10 cm showed a time spread of less than 20 ps, similar to the T4FASC-SPVSHC [58]. The focal waveform and spot size are shown in Fig. 5.13 and Fig. 5.14.

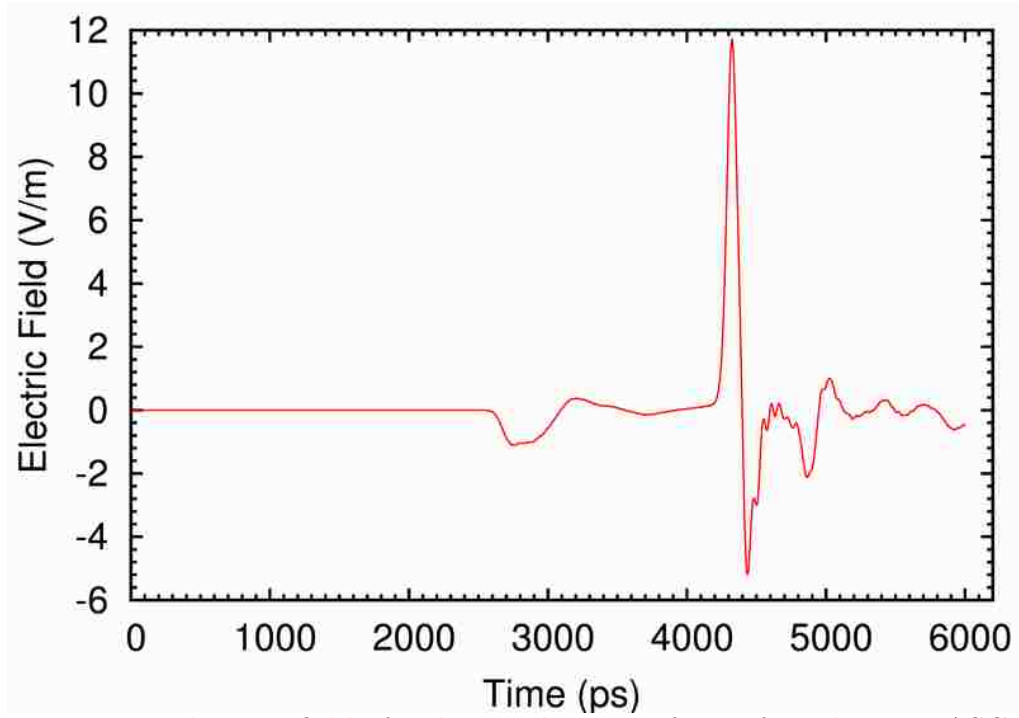


Figure 5.13: Electric field focal impulse waveform for the T4FASC-CPV configuration.

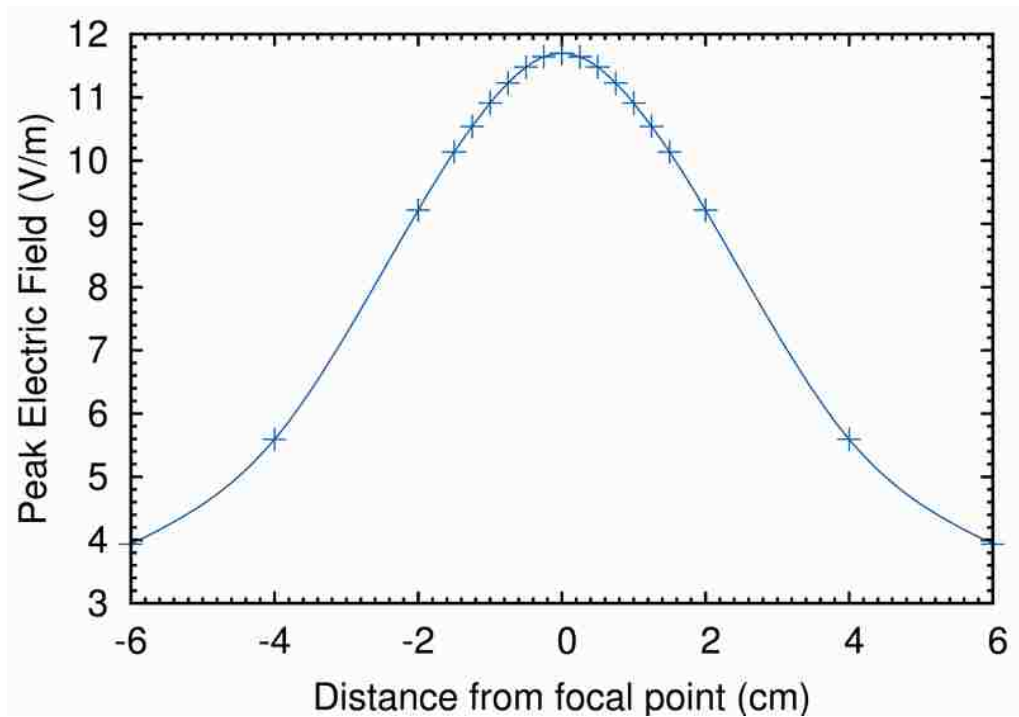


Figure 5.14: Spot size for the T4FASC-CPV configuration.

Again, these results indicate that the electric field is enhanced, compared to the T4FASC configuration in Table 5.1, with the pressure vessel by approximately 62%,  $E_{\max} = 11.7$  V/m. The corresponding increase in the spot diameter is only 18%, beam width = 4.95 cm. Although the  $E_{\max}$  is less than the T4FASC-SPVSHC, the T4FASC-CPVCHC configuration is attractive since it is easier to fabricate.

Note that the high-frequency (optical) approximations used to determine the pressure vessel dimensions are only accurate to first order as they do not take into account the lower frequencies (larger wavelengths) in the input pulse. Also, the hydrogen chamber does not play any role in the propagation of the expanding spherical wave [59].

## 5.4 Optimization of Switch System Components

Various components of the switch and pressure vessel design were optimized so that a large peak electric field and a small spot size were obtained. For the spherical pressure vessel configuration the following ranges yield a satisfactory electric field amplification [60],

- Feed arm length:  $18 \text{ cm} \leq l \leq 22 \text{ cm}$ ,
- Height of cylindrical support structure:  $0.2 \text{ cm} \leq H_{\text{css}} \leq 0.6 \text{ cm}$ ,
- Pressure vessel radius:  $1.50 \text{ cm} \leq r_{\text{pv}} \leq 3.0 \text{ cm}$ .

The height and radius of the pressure vessel for the cylindrical pressure vessel design are fixed by the formulas in the previous section. The range of the feed arm length,  $l$ , for the T4FASC-CPVCHC configuration is identical to the T4FASC-SPVSHC design.

## 5.5 Comparison of electromagnetic parameters for the T4FASC-SPVSHC and T4FASC-CPVCHC configurations with the focusing lens

Having completed the switch system and pressure vessel designs it is imperative to revisit the electromagnetic parameters, as calculated in Ch. 3, for the full PSIRA system composed of the reflector, switch, pressure vessel and the focusing lens. In order to do so, consider the following optimized dimensions for the T4FASC-SPVSHC and T4FASC-CPVCHC designs [61],

- SPVSHC:
  - feed arm + loft length,  $l = 19.0$  cm,
  - height of the CSS,  $H_{\text{css}} = 0.2$  cm,
  - radius of the pressure vessel,  $r_{\text{pv}} = 2.0$  cm,
- CPVCHC: feed arm + loft length,  $l = 19.0$  cm.

The electromagnetic parameters, at the second focus, of the 4 Feed-Arm (4FA), T4FASC-SPVSHC and T4FASC-CPVCHC configurations, in air and with the focusing lens are summarized in Table. 5.4. The spot sizes are compared in Table. 5.5. The 4FA configuration is identical to that in Ch. 3. One notes that, compared to the 4FA, there is over a 180% increase in the peak focal impulse electric fields with the focusing lens for the T4FASC-SPVSHC and T4FASC-CPVCHC configurations. This amplification overshadows the corresponding small increase in spot size. Also, the electric and magnetic enhancements are not significantly affected.

Table 5.4: Comparison of the electric and magnetic field information, for the 4FA, T4FASC-CSS-SPVSHC, T4FASC-CSS-CPVCHC configurations, at focal point, in air and with focusing lens (FL)

Field Information	Configuration		
	4FA	T4FASC-CSS-SPVSHC	T4FASC-CSS-CPVCHC
Peak E-Field No FL (V/m)	6.247	13.762	11.701
Peak H-Field No FL (A/m)	0.0151	0.03495	0.0297
Peak E-Field With FL (V/m)	10.725	21.864	18.637
Peak H-Field With FL (A/m)	0.0734	0.1537	0.1302
Impedance No FL ( $\Omega$ )	$Z_{\text{NFL}} = E_{\text{max}}^{\text{NFL}}/H_{\text{max}}^{\text{NFL}}$	393.763	393.973
Impedance With FL ( $\Omega$ )	$Z_{\text{WFL}} = E_{\text{max}}^{\text{WFL}}/H_{\text{max}}^{\text{WFL}}$	146.117	143.141
Electric enhancement	$E_{\text{max}}^{\text{WFL}}/E_{\text{max}}^{\text{NFL}}$	1.717	1.589
Magnetic enhancement	$H_{\text{max}}^{\text{WFL}}/H_{\text{max}}^{\text{NFL}}$	4.861	4.384

Table 5.5: Comparison of spot size for E and H field, for the 4FA, T4FASC-CSS-SPVSHC, T4FASC-CSS-CPVCHC configurations, with and without the focusing lens (FL)

Spot Size Information	Configuration		
	4FA	T4FASC-CSS-SPVSHC	T4FASC-CSS-CPVCHC
E-Field Spot Size No FL (cm)	3.6104	4.644	4.949
H-Field Spot Size No FL (cm)	3.6502	4.937	5.232
E-Field Spot Size With FL (cm)	1.187	1.448	1.537
H-Field Spot Size With FL (cm)	1.1954	1.514	1.575
E-Field Spot Size reduction	EFSS <sup>NFL</sup> /EFSS <sup>WFL</sup>	3.042	3.207
H-Field Spot Size reduction	HFSS <sup>NFL</sup> /HFSS <sup>WFL</sup>	3.054	3.261

## 5.6 Discussion

The basic PSIRA system can be thought to consist of three major components: (1) reflector, (2) focusing lens, and (3) launching lens. The focusing lens design in Ch. 3 together with the launching lens designs in this chapter complete the conceptual realization of the PSIRA.

As mentioned in Ch. 2, the primary application of the PSIRA system is intended for treatment of skin cancer (melanoma). The expectations of our collaborators at the Old Dominion University (ODU), from the PSIRA, are summarized in Table 5.6<sup>1</sup> [62].

Table 5.6: Parameters expected from the PSIRA by ODU.

Parameter	Requirement
FWHM	$\leq 200$ ps
Peak impulse amplitude	20-50 kV/cm
Spot area	$\leq 1$ cm <sup>2</sup>
Frequency (repetition rate)	$\gtrsim 10$ kHz
Duration	5-10 mins

For the PSIRA system designed, with the focusing and launching lenses, the FWHM is well below 200 ps, even after allowing for dispersion inside the lens materials. From Table. 5.4, the peak electric field with the launching and focusing lenses is approximately 0.2 V/cm. To obtain a 20 kV/cm peak impulse amplitude requires an input of approximately  $20/0.2$  kV = 100 kV or more, which is quite easily achieved in practice (the actual input voltage is likely much greater to account for experimental losses, such as losses in the lens materials). As observed in Table 5.5, the spot areas are approximately twice that of the desired values. However, a ten layer focusing lens would bring this down to the millimeter range. The duration of 5-10 mins is also practically achievable. The most challenging constraint is the frequency or repetition

<sup>1</sup>Personal communication with Shu Xiao, Assistant Professor, ODU

rate. With the current technology, the maximum frequency of the switch discharge is only a few 100 Hz with a maximum of 1 KHz<sup>2</sup>.

The designs of the switch system and launching lens outlined provide an excellent starting point for the experimental realization and testing of a high-voltage prototype PSIRA. Nevertheless, there are many practical challenges, some of which are discussed below.

Numerical simulations used in the design of the switch system in this chapter have not considered the physics of gas discharges. Ultrafast switching (100 ps domain) depends on extremely fast electrical pulses generated by mm spark gaps at high gas pressure (typically  $H_2$ ). Factors such as the electron drift velocity, velocity of electromagnetic propagation in the switch region and the inductance of the arc will have to be thoroughly studied in the context of the PSIRA [63]. As mentioned above, a major hurdle pertains to high-frequency switching. Higher frequencies, of the order of a few kHz, are required to induce apoptosis in cells. Hence, techniques to increase the frequency of switch discharges must be investigated.

In the experimental realization of the switch system, the (truncated) feed-arms are charged, to a few 100 kV, and then discharged through the switch cones. The hydrogen chamber is filled with high-pressure gas to avoid breakdown at lower voltages (cf. Paschen's law). The pressure vessel prevents the system from blowing apart due to the high pressure in the hydrogen chamber. External support structures are typically used to hold the pressure vessel together. Capacitors may be used in series with the feed-arms to provide desired rise times in the input voltage. Some initial considerations for a feed and mechanical support structure are outlined in [64].

For the two and four feed-arm PSIRA configurations it has been analytically established that the size of the reflector solely dictates the magnitude of the pre-

---

<sup>2</sup>Personal communication with Mike Skipper, ASR Corporation



pulse [10]. For the T4FASC-SPVSHC and T4FASC-CPVCHC designs however, one observes that the prepulse is of a much shorter duration, as seen from Fig. 5.8 and Fig. 5.13. This shorter prepulse permits the scaling down of the reflector size and hence the overall dimensions of the system. It is shown in [65] that the reflector can be scaled down by as much as 55%-70% while providing a satisfactory  $E_{\max}$  and spot size.

The fast electromagnetic pulses delivered by the PSIRA can also be used to diagnose the permittivities and thicknesses of layered dielectric media. For such an application, the Brewster angle of the first layer plays an important role. For transmitting an intense short electromagnetic pulse, normal incidence, augmented by the focusing lens, is found to be optimal. Analytical considerations of such a concept are outlined in [66].

# TERAHERTZ APPLICATION

SWO

## Chapter 6

# The Switched Oscillator as a THz Antenna

*“What we work on today, others will first think of tomorrow.”*

*– Alan Perlis*

Despite great scientific interest since the late 1920s, the terahertz (THz) frequency range remains one of the least tapped regions of the electromagnetic spectrum. Sandwiched between infrared and optical frequencies, it has received little commercial emphasis over the years [67]. The exact definition varies among authors [67, 68] but the following definition is adopted here [69],

$$0.1 \text{ THz} < f < 10 \text{ THz} \tag{6.1}$$

THz radiation is used in various applications, such as imaging, security surveillance, spectroscopy, submillimeter astronomy, among others. In this dissertation, the focus is on secure communication and radar applications. At present, most wireless communication networks exploit the radio wave and microwave portions of

the electromagnetic spectrum; therefore, transmission of a signal in the THz range is relatively secure because these waves cannot propagate long distances.

As frequency increases it becomes increasingly difficult to generate radiation at usable power levels. This limitation is due to the decrease in size of the frequency-sensitive elements. High-power microwave sources typically operate at hundreds of kV of charge voltage, and release the stored energy in nanosecond time scales. As an example, the MATRIX wideband source developed at the Air Force Research Laboratory [70] operates at approximately 200 kV charge voltage, switching this out through a high pressure hydrogen switch which closes in approximately 100 ps with a radiated waveform lasting tens of nanoseconds. This discharges a length of transmission line with one end approximately open (antenna end) and the other shorted (switch end) as a quarter wave resonator. The microwaves are synthesized as the voltage on the transmission line oscillates back and forth. This is rather high pulsed power. Scaling this down to THz frequencies (mm scale) one can perhaps operate at a hundred volts or so.

One pulsed power approach to THz generation uses PhotoConductively (PC) switched planar antennas illuminated by ultra short optical pulses. Recent advances in femtosecond (fs) lasers and ultrafast PC semiconducting thin films have made this approach attractive [68]. The use of a PC-switched Switched Oscillator (SwO) as an antenna is outlined in this chapter. Compared to other sources of THz radiation, such as traveling wave tubes, backward wave oscillators, free electron lasers, and optical approaches, PC-Switched Antennas (PCSAs) are attractive due to their conceptual simplicity, small size and their ability to radiate high-energy resonant pulses. In addition, this solution is a relatively inexpensive approach.

## 6.1 Frequencies for Atmospheric Transmission

Communication and radar applications require transmission through the atmosphere, perhaps for kilometers. While radar means radio detection and ranging, one might call a THz radar as a TEDAR (Terahertz Detection and Ranging).

Measurements have been made of the propagation (attenuation) of THz radiation through both dry and moist air [71]. The frequencies of interest (minima in the attenuation curves) are summarized in Table 6.1.

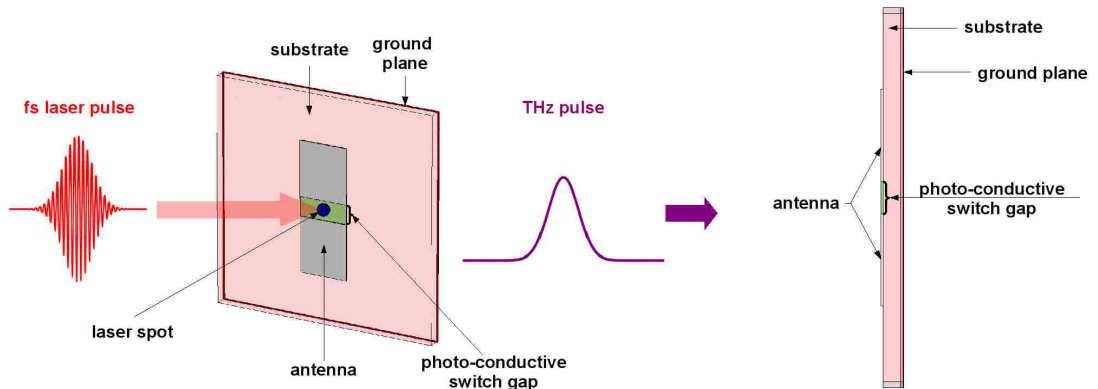
Table 6.1: Attenuation of the Electromagnetic Waves at favorable frequencies

Frequency (THz)	Attenuation (dB/Km)
0.080	0.3 – 4
0.205	2 – 10
0.300	4 – 12
0.405	15 – 30
0.680	50 – 100
0.880	40 – 100

In the presence of rain, the attenuation is slightly increased over the upper values. A frequency of approximately 0.3 THz is found to be most appropriate for transmission over large distances [69].

## 6.2 Desired Properties of the Photoconductive Switch Material

Figure 6.1 shows a typical pulse generation scheme using a PCSA mounted over a substrate [68].



(a) Terahertz (THz) generation using a photoconductive switch gap and an (dipole) antenna mounted over a substrate. (b) Side-view of antenna, switch gap and substrate.

Figure 6.1: Schematic diagram of THz generation using a photoconductive switch and an (dipole) antenna.

When the PC switch gap is pumped with femtosecond optical pulses with an energy greater than the bandgap of the semiconductor, free electrons (holes) are generated in the conduction (valence) band. These carriers result in a pulsed photocurrent in the antenna. The antenna is designed to emit a picosecond-scale electromagnetic transient, i.e., a THz pulse [68].

It is clear that the material properties of the PC switch and the antenna geometry play an important role in this scheme. In our design, hundreds of volts will be applied across the switch. The antenna is designed such that the radiated energy decays as a damped sinusoid, i.e., the carrier lifetime of the PC switch gap material should be much longer than the duration of the input pulse. Therefore, the PC switch material must have properties such as long carrier lifetime, high mobility and high breakdown

voltage. Of the currently used PC materials, Cr-doped SI-GaAs (semi-insulating gallium arsenide) is found to satisfy these design constraints, as summarized in Table 6.2 [68].

Table 6.2: Parameters of Cr-doped SI-GaAs.

Parameter	Value
Carrier lifetime	50 – 100 ps
Mobility	0.1 m <sup>2</sup> /(V s)
Resistivity	10 <sup>4</sup> Ω m
Breakdown field	50 M V/m

### 6.3 The Switched Oscillator as a Terahertz Radiator

Having identified the frequencies required for our application and the most suitable technology for THz generation, this section presents a proof-of-concept design of a high-energy, pulsed-power, switched-oscillator, PC-switched antenna [72].

The SwO is an electrical, shock-excited resonant structure (e.g., a transmission line). The excitation may come in the form of the discharge of some slowly charged capacitance through a fast closing switch. The waveform delivered to the load is characterized by one or more damped sinusoids [73].

Here we adapt the SwO as the planar antenna in Fig. 6.1. As the most basic formulation of the problem, consider the setup shown in Fig. 6.2, where the SwO is operated in differential form as a half-wave micro-strip resonator to maximize the

energy in the radiated pulse.

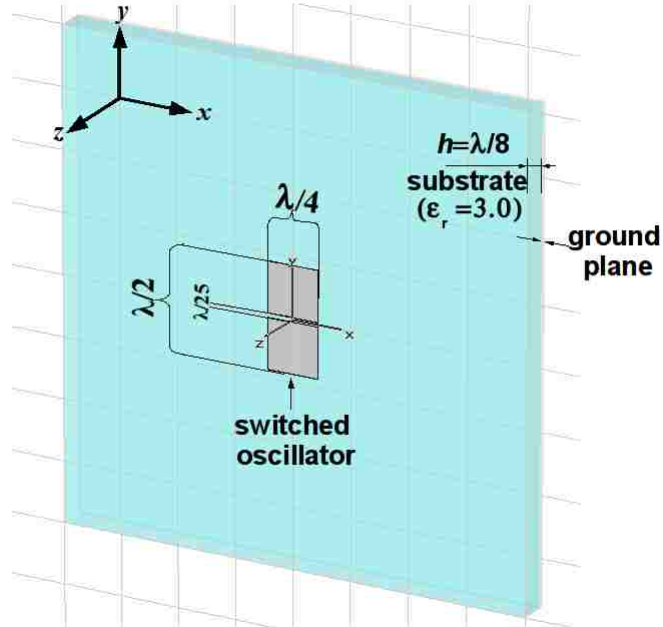


Figure 6.2: Schematic of a SwO mounted over a substrate.

The width of the SwO is (arbitrarily) chosen as a quarter wavelength to reduce skin effect losses without introducing other modes of oscillation. The length of the PC switch gap is  $\lambda/25$  and is kept small to minimally perturb the SwO. The SwO is mounted on a substrate of relative permittivity  $\epsilon_r=3.0$  and height  $\lambda/8$ . A ground plane below the substrate ensures the radiation is confined in the  $+z$  direction (see Fig. 6.2 for the coordinate system). Our primary aim is to maximize the radiated electric field at the desired resonant frequency. Note that  $\lambda$  corresponds to the wavelength in the dielectric.

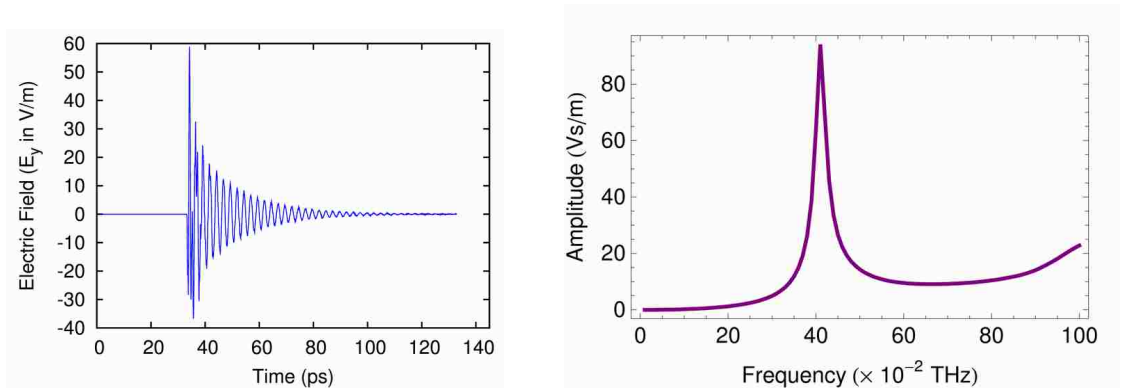
The structure in Fig. 6.2 was simulated using CST Microwave Studio®<sup>1</sup>, a commercially available finite integration time domain (FITD) electromagnetic software. In the simulations, the SwO is assumed to be a perfect electric conductor (PEC) and the substrate dielectric material is assumed to be lossless and dispersionless. The SwO dimensions are determined for a free space wavelength of  $\lambda_0 = 500 \mu\text{m}$

<sup>1</sup><http://www.cst.com>



corresponding to a (resonant) frequency of 0.6 THz. The wavelength  $\lambda$  in the substrate is  $\lambda_0/\sqrt{3} = 346.1 \mu\text{m}$ . A 1 V ramp rising excitation, with a 0.1 ps rise time, was applied between the switch gap. A far-field electric field probe, oriented in the  $+y$  direction, at a distance 1 cm from the origin on the  $z$ -axis, was used to monitor the electric fields radiated by the antenna.

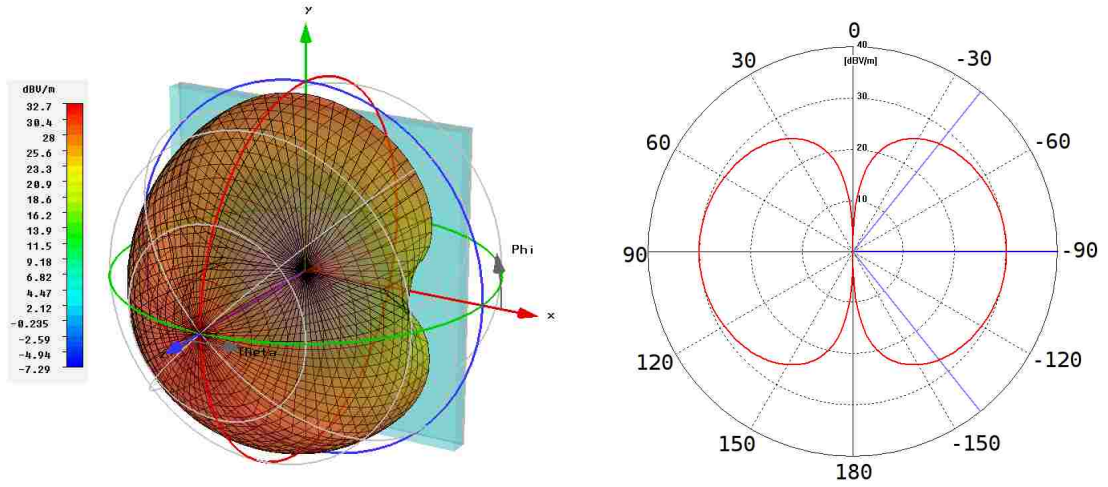
The electric field waveform is shown in Fig. 6.3(a). The damped sinusoidal electric field profile decays to zero in approximately 50 ps, and is one of the reasons SI-GaAs was chosen as the PC switch material. SI-GaAs has a sufficiently long carrier lifetime, 50-100 ps, which ensures that the photocurrent decays completely before the next input pulse. The Fourier transform of the electric field, Fig. 6.3(b), indicates a resonance at 0.4 THz. The radiation pattern is dipole-like, as shown in Fig. 6.4. Note that while the dimensions were determined for a frequency of 0.6 THz, the SwO is found to resonate at 0.4 THz. This is because the calculations of the resonant frequency were based on crude assumptions and did not accurately account for various factors such as the finite closing time of the switch, switch length, SwO width, fringe fields, among others. The dependence of the radiated power and resonant frequency on various parameters is more thoroughly investigated in the next chapter.



(a) Electric field response,  $E_y$ , from far-field probe at 1 cm from the origin on the  $z$ -axis.

(b) Fourier transform of the electric field response,  $E_y$ , from the far-field probe.

Figure 6.3: Electric field response and its Fourier transform.



(a) 3D electric field radiation pattern from SwO antenna at 0.4 THz. (b) 2D E-plane electric-field radiation pattern ( $\theta = 90^\circ$ ) at 0.4 THz.

Figure 6.4: Electric field radiation patterns from SwO at the resonant frequency, 0.4 THz.

While previous researchers have focused on generating a single transient pulse [68], the pulse radiated from a SwO antenna is of a much longer duration. This results in roughly an order of magnitude increase in the energy in the pulse.

## 6.4 Maximizing Energy in Terahertz Pulse Radiation from a Switched Oscillator

Pursuing the design of a pulsed (damped sinusoid) SwO THz radiator we need to find some optimization conditions. Given some frequency,  $f_0$ , how much energy can we radiate in a damped sinusoidal pulse? This depends on the various parameters of the antenna and the source. For the present purposes let us consider the configuration in Fig. 6.5 [74].

Here we have a conducting ground plane (typically copper). This is separated from the antenna by a dielectric of permittivity  $\epsilon$  and thickness  $h$ . The antenna is

a half-wavelength radiator of length  $l_a$ . Each half is charged to  $\pm V_0$ , respectively. These halves are separated by a switch medium (say semi-insulating gallium arsenide) of length  $l_s$ . The width of the antenna is  $w$ . The switch is illuminated by a femtosecond laser to cause it to conduct (close).

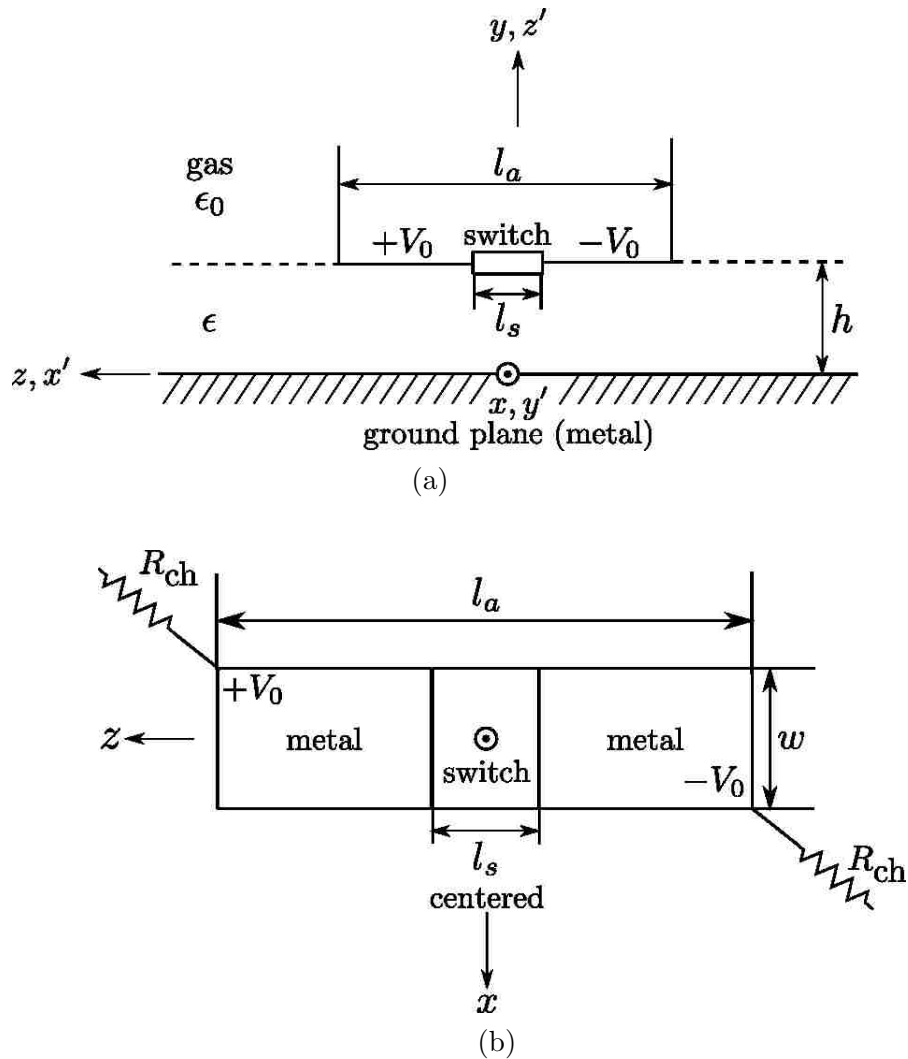


Figure 6.5: THz radiator. (a) Side view and (b) Front view.

### 6.4.1 Maximizing the Stored Energy

The stored energy is

$$U_0 = \frac{1}{2}C[2V_0]^2 = 2CV_0^2. \quad (6.2)$$

The energy available at  $f_0$ , the dominant half-wave resonant frequency, is estimated as [75]

$$U_1 = \frac{8}{\pi^2}U_0 \approx 0.81U_0, \quad (6.3)$$

with the remaining energy used to excite higher order resonant frequencies, which we neglect. We need to maximize this energy and radiate as much of this as possible. Thus we need to maximize  $2CV_0^2$ .

Consider the capacitance,  $C \approx \epsilon w l_a / h$ . For a given  $h$ , this is maximized by large  $w$ , the length,  $l_a$ , being given by

$$\begin{aligned} \lambda_{\text{os}} &\approx 2l_a = \frac{v}{f_0}, \quad (\text{"os"} = \text{oscillator}), \\ v &\approx c\epsilon_r^{-1/2}, \quad \epsilon_r = \frac{\epsilon}{\epsilon_0}, \end{aligned} \quad (6.4)$$

or more accurately

$$c > v > c\epsilon_r^{-1/2}, \quad (6.5)$$

with  $v$  approaching  $c\epsilon_r^{-1/2}$  for large  $w$ , since most of the capacitive energy lies between the antenna and the ground plane. However, we do not want  $w$  to be so large that higher order oscillation modes are supported. Thus, we constrain the width as

$$w \approx \frac{l_a - l_s}{2}, \quad (6.6)$$

for obtaining a large capacitance. This capacitance can be estimated as

$$C \approx \frac{\epsilon w [l_a - l_s]}{4h}, \quad (6.7)$$

as two capacitors in series.

One can maximize  $C$  by minimizing  $h$ , but it is the energy we wish to maximize. So consider maximizing  $V_0$ . As an approximation we can estimate this via

$$V_1 = E_d h, \quad (6.8)$$

$E_d \equiv$  average breakdown electric field through  
dielectric to ground plane.

This includes the edge effects on the antenna which can be mitigated to some extent by roll-ups on the edges.

Another voltage limitation concerns the switch, which needs to be highly insulating before the arrival of the fs laser pulse. Let us estimate the voltage stand-off as

$$V_2 = E_s l_s, \quad (6.9)$$

$E_s \equiv$  average breakdown electric field through  
switch between two antenna halves.

As we increase  $V_0$  and accordingly increase  $h$  we have

$$U_0 = 2CV_0^2 = \frac{\epsilon w [l_a - l_s]}{2h} [E_d h]^2 = \frac{\epsilon w [l_a - l_s]}{2} h E_d^2, \quad (6.10)$$

thereby increasing  $U_0$ . Similarly, as we increase  $V_0$  and accordingly increase  $l_s$  we have

$$U_0 = 2CV_0^2 = \frac{\epsilon w [l_a - l_s]}{2h} [E_s l_s]^2. \quad (6.11)$$

Increasing  $h$  in (6.10) increases the stored energy up until the switch limits the voltage. Increasing  $h$  beyond this *decreases* the stored energy. Equating the two results gives

$$\frac{\epsilon w [l_a - l_s]}{2} h E_d^2 = \frac{\epsilon w [l_a - l_s]}{2h} [E_s l_s]^2 \Rightarrow \frac{h}{l_s} = \frac{E_s}{E_d} \quad (6.12)$$

Chapter 6. The Switched Oscillator as a THz Antenna

as an approximate optimum. However, while one may wish

$$h \approx \frac{\lambda}{4}, \quad (6.13)$$

for radiation characteristics, we need

$$l_s < l_a, \quad (6.14)$$

as a limiting factor, which may alter the results of (6.12). For example, if

$$E_d > E_s, \quad (6.15)$$

then our limitation on the energy is given by (6.11) with the limit in (6.13). In that case we need to maximize (for fixed  $l_a$ )

$$X = [l_a - l_s]l_s^2. \quad (6.16)$$

Differentiating with respect to  $l_s$  gives

$$0 = 2l_al_s - 3l_s^2 \Rightarrow \frac{l_s}{l_a} = \frac{2}{3}. \quad (6.17)$$

There are still other factors to consider such as switch losses and conductor losses.

## 6.4.2 Ideal Radiation Characteristics

### 6.4.2.1 Single electric dipole radiator

Let us make some simple estimate of the radiated fields. An electric dipole, in free space, has far fields [76]

$$\begin{aligned}\tilde{\vec{E}}_f(\vec{r}, s) &= \frac{\mu_0}{4\pi r} s^2 e^{-\gamma r} \overleftrightarrow{\mathbf{1}}_r \times [\vec{\mathbf{1}}_r \times \tilde{\vec{p}}(s)] = -\frac{\mu_0 s^2}{4\pi r} \vec{\mathbf{1}}_r \cdot \tilde{\vec{p}}(s) e^{-\gamma r}, \\ \tilde{\vec{H}}_f(\vec{r}, s) &= Z_0^{-1} \vec{\mathbf{1}}_r \times \vec{E}_f(\vec{r}, s),\end{aligned}\quad (6.18)$$

$\tilde{\phantom{x}} \equiv$  Laplace transform (two sided),

$\gamma \equiv s/c \equiv$  propagation constant,

$s \equiv \Omega + j\omega \equiv$  Laplace-transform variable or complex frequency,

$Z_0 \equiv [\mu_0/\epsilon_0]^{1/2} \equiv$  wave impedance of free space,

$\tilde{\vec{p}}(s) \equiv \tilde{p}(s) \vec{\mathbf{1}}_z \equiv$  electric dipole moment,

$\overleftrightarrow{\mathbf{1}}_r \equiv \overleftrightarrow{\mathbf{1}} - \vec{\mathbf{1}}_r \vec{\mathbf{1}}_r = \vec{\mathbf{1}}_\theta \vec{\mathbf{1}}_\theta - \vec{\mathbf{1}}_\phi \vec{\mathbf{1}}_\phi \equiv$  transverse dyad.

This gives a radiated power,  $s = j\omega$ , as

$$P_1 = \frac{1}{2} \int_S [\tilde{\vec{E}}_f(\vec{r}, j\omega) \times \tilde{\vec{H}}_f(\vec{r}, -j\omega)] 4\pi r^2 dS, \quad (6.19)$$

$S \equiv$  sphere of radius  $r$ . The factor  $1/2$  gives the average power over a cycle. Appropriately substituting gives

$$\begin{aligned}
 P_1 &= \frac{\mu_0 \omega^4}{32\pi^2 r^2 c} \int_S \tilde{\vec{p}}(j\omega) \cdot \overleftarrow{\mathbf{1}}_r \cdot \tilde{\vec{p}}(-j\omega) 4\pi r^2 dS \\
 &= \frac{\mu_0 \omega^4}{8\pi c} \int_0^\pi \int_0^{2\pi} |\tilde{\vec{p}}(j\omega)|^2 \overleftarrow{\mathbf{1}}_z \cdot \overleftarrow{\mathbf{1}}_r \cdot \overleftarrow{\mathbf{1}}_z \sin(\theta) d\phi d\theta \\
 &= \frac{\mu_0 \omega^4}{4c} |\tilde{\vec{p}}(j\omega)|^2 \int_0^\pi [\overleftarrow{\mathbf{1}}_z \cdot \overleftarrow{\mathbf{1}}_\theta]^2 \sin(\theta) d\theta \\
 &= \frac{\mu_0 \omega^4}{4c} |\tilde{\vec{p}}(j\omega)|^2 \int_0^\pi \sin^3(\theta) d\theta \\
 &= \frac{\mu_0 \omega^4}{3c} |\tilde{\vec{p}}(j\omega)|^2 \approx 0.33 \mu_0 \omega^4 |\tilde{\vec{p}}(j\omega)|^2, \\
 c &= [\mu_0 \epsilon_0]^{-1/2} \equiv \text{speed of light.}
 \end{aligned} \tag{6.20}$$

#### 6.4.2.2 Two dipole radiators $\lambda/2$ apart

Let us approximate the SwO over a ground plane as two dipoles, the SwO and its image separated by a half-wavelength,  $180^\circ$  out of phase, but only radiating into a half-space. Let one dipole be at  $y = +\lambda/4$  with the second at  $y = -\lambda/4$ . Then we can superimpose the two dipole fields as

$$\begin{aligned}
 \tilde{\vec{E}}_f(\vec{r}, s) &= \frac{-\mu_0}{4\pi r} s^2 \overleftarrow{\mathbf{1}}_r \cdot \tilde{\vec{p}}(s) \overleftarrow{\mathbf{1}}_z [e^{-\gamma[r - \frac{\lambda}{4} \overleftarrow{\mathbf{1}}_y \cdot \overleftarrow{\mathbf{1}}_r]} - e^{-\gamma[r + \frac{\lambda}{4} \overleftarrow{\mathbf{1}}_y \cdot \overleftarrow{\mathbf{1}}_r]}] \\
 &= \frac{-\mu_0}{4\pi r} \tilde{\vec{p}}(s) \overleftarrow{\mathbf{1}}_r \cdot \tilde{\vec{p}}(s) e^{-\gamma r} 2 \sinh\left(\frac{\gamma \lambda}{4} \sin(\theta) \sin(\phi)\right), \\
 \tilde{\vec{H}}_f(\vec{r}, s) &= Z_0^{-1} \overleftarrow{\mathbf{1}}_r \times \tilde{\vec{E}}_f(\vec{r}, s).
 \end{aligned} \tag{6.21}$$

This is an odd function of  $\phi$  (or  $\sin(\phi)$ ). For  $s = j\omega$  we also have

$$\gamma = jk = j\frac{\omega}{c}. \tag{6.22}$$

Now, it is convenient to change variables so that the argument of  $\sinh$  is a function



of only one coordinate. For this purpose choose

$$\begin{aligned}
 (x', y', z') &= (z, x, y) \Rightarrow (\vec{\mathbf{1}}_{x'}, \vec{\mathbf{1}}_{y'}, \vec{\mathbf{1}}_{z'}) = (\vec{\mathbf{1}}_z, \vec{\mathbf{1}}_x, \vec{\mathbf{1}}_y), \\
 r &= [x^2 + y^2 + z^2]^{1/2} = [x'^2 + y'^2 + z'^2]^{1/2}, \\
 z' &= r \cos \theta', \\
 \psi' &= [x'^2 + y'^2]^{1/2} = r \sin(\theta'), \\
 x' &= \psi' \cos(\phi') = r \sin(\theta') \cos(\phi'), \\
 y' &= \psi' \sin(\phi') = r \sin(\theta') \sin(\phi'), \\
 \vec{\mathbf{1}}_r &= \vec{\mathbf{1}}_{z'} \cos \theta' + \vec{\mathbf{1}}_{\psi'} \sin(\theta') \\
 &= \vec{\mathbf{1}}_{z'} \cos(\theta') + \vec{\mathbf{1}}_{x'} \sin(\theta') \cos(\phi') \\
 &\quad + \vec{\mathbf{1}}_{y'} \sin(\theta') \sin(\phi') \\
 &= \vec{\mathbf{1}}_z \cos(\theta) + \vec{\mathbf{1}}_\psi \sin(\theta) \\
 &= \vec{\mathbf{1}}_z \cos(\theta) + \vec{\mathbf{1}}_x \sin(\theta) \cos(\phi) + \vec{\mathbf{1}}_y \sin(\theta) \sin(\phi).
 \end{aligned} \tag{6.23}$$

This implies

$$\begin{aligned}
 \sin(\theta) \sin(\phi) &= \cos(\theta'), \\
 \vec{\mathbf{1}}_{x'} \cdot \overleftrightarrow{\mathbf{1}}_r \cdot \vec{\mathbf{1}}_{x'} &= 1 - [\vec{\mathbf{1}}_{x'} \cdot \vec{\mathbf{1}}_r]^2 = 1 - \sin^2(\theta') \cos^2(\phi').
 \end{aligned} \tag{6.24}$$

Then we have the radiated power

$$\begin{aligned}
 P_2 &= \frac{1}{2} \int_S [\vec{\mathbf{E}}_f(\vec{r}, j\omega) \times \vec{\mathbf{H}}_f(\vec{r}, -j\omega)] \cdot \vec{\mathbf{1}}_r dS \\
 &= \frac{\mu_0 \omega^4}{32\pi^2 r^2 c} |\tilde{p}(j\omega)|^2 \int_S \vec{\mathbf{1}}_{x'} \cdot \overleftrightarrow{\mathbf{1}}_r \cdot \vec{\mathbf{1}}_{x'} 4 \sin^2 \left( \frac{k\lambda}{4} \cos \theta' \right) dS \\
 &= \frac{\mu_0 \omega^4}{2\pi c} |\tilde{p}(j\omega)|^2 \int_0^\pi \int_0^{2\pi} \sin^2 \left( \frac{k\lambda}{4} \cos \theta' \right) [1 - \sin^2(\theta') \cos^2(\phi')] \sin(\theta') d\phi' d\theta' \\
 &= \frac{\mu_0 \omega^4}{2c} |\tilde{p}(j\omega)|^2 \int_0^\pi \sin^2 \left( \frac{k\lambda}{4} \cos \theta' \right) [2 - \sin^2(\theta')] \sin(\theta') d\theta'.
 \end{aligned} \tag{6.25}$$

Substituting

$$\begin{aligned}\eta &= \cos(\theta'), \quad d\eta = -\sin(\theta')d\theta', \\ \sin^2(\theta') &= 1 - \cos^2(\theta') = 1 - \eta^2,\end{aligned}\tag{6.26}$$

gives

$$P_2 = \frac{\mu_0\omega^4}{2c} |\tilde{p}(j\omega)|^2 \int_0^1 \sin^2\left(\frac{k\lambda}{4}\eta\right) [1 + \eta^2] d\eta.\tag{6.27}$$

Substituting

$$\nu = \frac{k\lambda\eta}{4}, \quad d\nu = \frac{k\lambda}{4}d\eta,\tag{6.28}$$

gives

$$P_2 = \frac{\mu_0\omega^4}{2c} |\tilde{p}(j\omega)|^2 \frac{4}{k\lambda} \int_0^{\frac{k\lambda}{4}} \sin^2(\nu) \left[1 + \left[\frac{4\nu}{k\lambda}\right]^2\right] d\nu,\tag{6.29}$$

which is simplified as

$$P_2 = \frac{\mu_0\omega^4}{2c} |\tilde{p}(j\omega)|^2 \left[ \frac{-4k\lambda \cos\left(\frac{k\lambda}{2}\right) - 2(k^2\lambda^2 - 4) \sin\left(\frac{k\lambda}{2}\right)}{k^3\lambda^3} + \frac{2}{3} \right].\tag{6.30}$$

For a resonant (half-wave) condition we have

$$\begin{aligned}\lambda_0 &= 2l_a, \\ f_0\lambda_0 &= c, \quad f = \frac{\omega_0}{2\pi} = \frac{c}{\lambda_0} = \frac{c}{2l_a}, \\ k_0\lambda_0 &= \frac{\omega_0\lambda_0}{c} = 2\pi.\end{aligned}\tag{6.31}$$

In (6.30) we have

$$\sin\left(\frac{k\lambda}{2}\right) = 0, \quad \cos\left(\frac{k\lambda}{2}\right) = -1,$$

giving

$$\begin{aligned}P_2 &= \frac{\mu_0\omega^4}{2c} |\tilde{p}(j\omega)|^2 \left[ \frac{4}{k^2\lambda^2} + \frac{2}{3} \right] = \frac{\mu_0\omega^4}{2c} |\tilde{p}(j\omega)|^2 \left[ \frac{1}{\pi^2} + \frac{2}{3} \right] \\ &\approx 0.38 \frac{\mu_0\omega^4}{c} |\tilde{p}(j\omega)|^2.\end{aligned}\tag{6.32}$$

Noting that, with the ground plane, the radiation is only in the  $+z'$  direction, we have

$$P_3 = \frac{P_2}{2} \approx 0.19 \frac{\mu_0 \omega^4}{c} |\tilde{p}(j\omega)|^2 \quad (6.33)$$

as the forward radiated power.

### 6.4.2.3 Applicability

The foregoing analysis applies strictly to an imaged dipole in free space. The permittivity of the medium above the ground plane alters these results somewhat. Therefore this analysis should be applied for relatively small  $\epsilon_r$ .

As  $\epsilon_r$  is increased the half-wave resonant length becomes less than  $\lambda/2$  in free space, making the antenna a less efficient radiator. It still radiates, but it takes a longer time to radiate the energy,  $U_1$ , giving a higher  $Q$ .

Also, as  $\epsilon_r$  is increased there can be bound surface waves propagating along the dielectric surface. This takes some of the energy in an undesirable direction.

Even for  $\epsilon = \epsilon_0$ , the antenna is no longer electrically small, making the dipole characterization of the antenna only approximate.

### 6.4.2.4 Two closely spaced electric-dipole radiators

Now let the two dipoles be placed at

$$z' = \pm h, \quad h \ll \frac{\lambda}{4}. \quad (6.34)$$

Then (6.21) is replaced by

$$\begin{aligned}
 \vec{\tilde{E}}_f(\vec{r}, s) &= \frac{-\mu_0}{4\pi r} s^2 \tilde{p}(s) \overleftrightarrow{\mathbf{1}}_r \cdot \vec{\mathbf{1}}_z e^{-\gamma r} 2 \sinh(\gamma D \sin(\theta) \sin(\phi)) \\
 &\approx \frac{-\mu_0}{4\pi r} s^2 \tilde{p}(s) \overleftrightarrow{\mathbf{1}}_r \cdot \vec{\mathbf{1}}_z e^{-\gamma r} 2\gamma D \sin(\theta) \sin(\phi), \\
 \vec{\tilde{H}}_f(\vec{r}, s) &= Z_0^{-1} \overleftrightarrow{\mathbf{1}}_r \times \vec{\tilde{E}}_f(\vec{r}, s).
 \end{aligned} \tag{6.35}$$

Making the same coordinate transformation as in (6.23) and (6.24) gives a radiated power

$$\begin{aligned}
 P_2 &= \frac{1}{2} \int_s [\vec{\tilde{E}}_f(\vec{r}, j\omega) \times \vec{\tilde{H}}_f(\vec{r}, -j\omega)] \cdot \vec{\mathbf{1}}_r dS \\
 &= \frac{\mu_0 \omega^4}{8\pi^2 r^2 c} |\tilde{p}(j\omega)|^2 \int_S \vec{\mathbf{1}}_{x'} \cdot \overleftrightarrow{\mathbf{1}}_r \cdot \vec{\mathbf{1}}_{x'} [kh]^2 \cos^2(\theta') dS \\
 &= \frac{\mu_0 \omega^4}{2\pi c} |\tilde{p}(j\omega)|^2 [kh]^2 \int_0^\pi \int_0^{2\pi} \cos^2(\theta') [1 - \sin^2(\theta') \cos^2(\phi)] \sin(\theta') d\phi' d\theta' \\
 &= \frac{\mu_0 \omega^4}{2c} |\tilde{p}(j\omega)|^2 [kh]^2 \int_0^\pi \cos^2(\theta') [2 - \sin^2(\theta')] \sin(\theta') d\theta'.
 \end{aligned} \tag{6.36}$$

Substituting as in (6.26) gives

$$\begin{aligned}
 P_2 &= \frac{\mu_0 \omega^4}{c} |\tilde{p}(j\omega)|^2 [kh]^2 \int_0^1 \eta^2 [1 + \eta^2] d\eta \\
 &= \frac{\mu_0 \omega^4}{c} |\tilde{p}(j\omega)|^2 [kh]^2 \left[ \frac{1}{3} + \frac{1}{5} \right] \\
 &= \frac{8}{15} \frac{\mu_0 \omega^4}{c} |\tilde{p}(j\omega)|^2 \left[ \frac{\omega h}{c} \right]^2 \approx 0.53 \frac{\mu_0 \omega^4}{c} |\tilde{p}(j\omega)|^2 \left[ \frac{\omega h}{c} \right]^2.
 \end{aligned} \tag{6.37}$$

Note the extra factor of  $[kh]^2$ , lowering the radiated power. This factor is the square of the fraction of a half wavelength given by  $l_a$ . The electrically small antenna is a less efficient radiator.

Noting that the radiation is only in the  $+z'$  direction we have

$$P_3 = \frac{P_2}{2} = \frac{4}{15} \frac{\mu_0 \omega^4}{c} |\tilde{p}(j\omega)|^2 \left[ \frac{\omega h}{c} \right]^2 \approx 0.27 \frac{\mu_0 \omega^4}{c} |\tilde{p}(j\omega)|^2 \left[ \frac{\omega h}{c} \right]^2. \tag{6.38}$$

### 6.4.3 Matching to Electric Dipoles

#### 6.4.3.1 Dipole Characteristics

Our formulae are in terms of the dipole moment at the resonant frequency. We need to evaluate  $\tilde{p}(j\omega)$ . When the switch is closed (ideally instantaneously) there is generated a square wave oscillation with frequency  $f_0$ . The current in this wave is

$$I = \frac{V_0}{Z_c},$$

$$Z_c \approx Z_w \frac{h}{w} \equiv \text{transmission line characteristic impedance}, \quad (6.39)$$

$$Z_w \approx Z_0 \epsilon_r^{-1/2} = \left[ \frac{\mu_0}{\epsilon_0} \right]^{1/2} \equiv \text{wave impedance}. \quad (6.40)$$

This is only approximate.  $Z_c$  is lowered by fringe fields if  $w$  is not  $\gg h$ . Furthermore, the impedance is influenced by  $\epsilon_0$  above the dielectric as well as  $\epsilon$  in the dielectric.

In [75] it is shown that the peak current in the resonant mode is

$$I_{\max} = \frac{4}{\pi} I_0. \quad (6.41)$$

In this resonant mode the current is  $I_{\max}$  at the antenna center, but zero at the ends, giving,

$$I(z) = I_{\max} \cos\left(\frac{\pi z}{l_a}\right) \quad (6.42)$$

as the spatial distribution of the current.

An alternate formula [76] (compared to charge times distance) for an electric dipole moment is

$$\begin{aligned} \tilde{p}(j\omega_0) &= \frac{1}{s} \int_{-l_a/2}^{l_a/2} \tilde{I}(z, s) dz = \frac{I_{\max}}{j\omega_0} \int_{-l_a/2}^{l_a/2} \cos\left(\frac{\pi z}{l_a}\right) dz = \frac{I_{\max}}{j\omega_0} \left(\frac{2l_a}{\pi}\right) \quad (6.43) \\ &= -j \frac{8}{\pi^2} \frac{l_a}{\omega_0} I_0 = -j \frac{8}{\pi^2} \frac{l_a}{\omega_0} \frac{V_0}{Z_c} \approx -j \frac{8}{\pi^2} \frac{l_a}{\omega_0} \frac{w}{h} \frac{V_0}{Z_w} \approx -j \frac{4}{\pi^2} \frac{\lambda_0}{\omega_0} \frac{w}{h} \frac{V_0}{Z_w} \\ &= -j \frac{8}{\pi} \frac{c}{\omega_0^2} \frac{w}{h} \frac{V_0}{Z_w}. \end{aligned}$$

Hence we see the advantage of a large (but not too large) width  $w$ . As discussed in Section 6.4 we may not use the  $\lambda/4$  for  $h$ , but something less to increase the stored energy as in (6.11). This may also increase the  $Q$  of the resonance, except for possibly other losses.

### 6.4.3.2 Radiation Q

The radiation is, of course, in the form of a damped sinusoid. The  $Q$  of this resonance can be estimated as

$$Q = \pi N, \quad (6.44)$$

$N$  = number of cycles for field to fall to  $e^{-1}$  or energy to  $e^{-2}$

In one cycle the energy radiated is

$$\begin{aligned} U_3 &\approx P_3 T, \\ T &= \frac{1}{f_0} \approx \frac{\lambda_0}{c} \approx 2 \frac{l_a}{c} \\ &= \text{period of resonance.} \end{aligned} \quad (6.45)$$

The fractional energy radiated in one cycle is

$$\Delta U = \frac{U_3}{U_1} = \frac{\pi^2 P_3 T}{8 U_0}. \quad (6.46)$$

The fractional field lost in one cycle is

$$\Delta F \approx \frac{\Delta U}{2} = \frac{\pi^2 P_3 T}{16 U_0}, \quad (6.47)$$

giving

$$\begin{aligned} N &= \frac{1}{\Delta F} = \frac{2}{\Delta U} = \frac{16 U_0}{\pi^2 P_3 T}, \\ Q &= \pi N = \frac{16 U_0}{\pi P_3 T}. \end{aligned} \quad (6.48)$$

### 6.4.3.3 Combined results for $h = \lambda/4$

Combining (6.43) with (6.33) gives

$$P_3 = \frac{1}{2} \left[ \frac{1}{3} + \frac{1}{2\pi^2} \right] \frac{\mu_0 \omega_0^4}{c} \left[ \frac{8}{\pi} \frac{c}{\omega_0^2} \frac{V_0}{Z_w} \right]^2 \approx 1.25 \frac{V_0^2}{Z_w}. \quad (6.49)$$

This result is for  $h = \lambda/4$ , which is also of the order of  $w$ . So radiated power is of the general order of  $V_0^2/Z_w$  as one might expect.

Assuming the dielectric as the basic limitation with

$$V_0 \approx hE_d, \quad (6.50)$$

$$U_0 \approx \frac{\epsilon w [l_a - l_s]}{h} V_0^2. \quad (6.51)$$

the  $Q$  is then

$$Q = \pi N \approx \frac{16}{\pi} \frac{\epsilon w [l_a - l_s]}{h} V_0^2 \frac{Z_w}{1.25 V_0^2} \frac{c}{2l_a} \approx 2 \frac{w [l_a - l_s]}{h l_a}. \quad (6.52)$$

This is of the general order of 2.0 (since it is assumed that  $l_a \gg l_s$  and  $w \approx h$ ;  $\therefore Q \approx 2w/h = 2.0$ ), indicating a highly damped oscillation, for which our approximations are inaccurate. This low  $Q$  is associated with our *very fat* dipoles. This would change significantly if  $w$  were  $\ll h$ .

### 6.4.3.4 Combined results for $h \ll \lambda/4$

Using the results of (6.38) instead, we have

$$P_3 = \frac{4}{15} \frac{\mu_0 \omega_0^4}{c} \left[ \frac{\omega_0 h}{c} \right]^2 \left[ \frac{8}{\pi} \frac{c}{\omega_0^2} \frac{V_0}{Z_w} \right]^2 = \frac{256}{15\pi^2} \left[ \frac{\omega_0 h}{c} \right]^2 \frac{V_0^2}{Z_w}. \quad (6.53)$$

Now we see the power reduction by the factor  $[\omega_0 h/c]^2$ . We see a power radiated proportional to  $h^2 V_0^2$ , and a field proportional to  $h V_0$ .

Again, assuming the dielectric as the basic limitation, as in (6.50), we have

$$Q = \pi N \approx \frac{16}{\pi} \frac{\epsilon w [l_a - l_s]}{h} V_0^2 \frac{15\pi^2}{256} \left[ \frac{c}{\omega_0 h} \right]^2 \frac{Z_w}{V_0^2} \frac{c}{2l_a} \approx \frac{15\pi}{32} \frac{w [l_a - l_s]}{h l_a} \left[ \frac{c}{\omega_0 h} \right]^2. \quad (6.54)$$

With  $h \ll l_a/2$  we might make  $l_s$  small since the switch needs to hold off less voltage.

This gives,

$$Q \approx \frac{15\pi w}{32 h} \left[ \frac{c}{\omega_0 h} \right]^2 = \frac{15 w}{128\pi h} \left[ \frac{c}{f_0 h} \right]^2 = \frac{15 w}{128\pi h} \left[ \frac{\lambda_0}{h} \right]^2 = \frac{15 w}{32\pi h} \left[ \frac{l_a}{h} \right]^2. \quad (6.55)$$

With

$$w \approx \frac{l_a}{2}, \quad (6.56)$$

this becomes

$$Q \approx \frac{15}{64\pi} \left[ \frac{l_a}{h} \right]^3. \quad (6.57)$$

allowing one to adjust to some desired  $Q$ .

#### 6.4.3.5 Limitations

The foregoing is for the case of air, dielectric between the antenna and the ground plane. Practically, one needs a dielectric plane with relative dielectric constant of a few to support the antenna. This will shorten  $l_a$  for a given resonance frequency, thereby lowering the efficiency of radiating into air, thereby raising the  $Q$ . There may also be some thin dielectric to coat the switch and perhaps antenna to increase the voltage standoff to  $> V_0$  as desired.

#### 6.4.4 Effect of Dielectrics

Of necessity there needs to be a substrate to support the antenna above the ground plane as in Fig. 6.5. This complicates the electromagnetic analysis, introducing surface waves guided by the dielectric over the ground plane.

These surface waves have been studied previously, e.g., [77–80]. It is noted that the cutoff efficiency is obtained just below the cutoff thickness of the  $H_0$  surface-wave



mode. The  $E_0$  surface wave mode does not have a cutoff frequency, but for small  $h$  is only weakly excited by the antenna. Maximum efficiency occurs just before the  $H_0$  surface wave mode can be excited. The optimum substrate thickness satisfies [81]

$$h_{\text{opt}} \lesssim \frac{\lambda_0}{4} [\epsilon_r - 1]^{-1/2}. \quad (6.58)$$

Furthermore, it would appear that the presence of a superstrate may further improve the design [81].

Note that the dielectrics decrease the size of the antenna for the resonant condition. This will significantly affect the  $Q$ .

### 6.4.5 Skin-Effect Losses

There are losses associated with the finite conductivity of the metal. The skin depth for a good conductor is [82]

$$\delta_s = \left[ \frac{2}{\omega \mu_0 \sigma} \right]^{1/2} = \left[ \frac{1}{\pi f \mu_0 \sigma} \right]^{1/2}. \quad (6.59)$$

This gives a surface impedance

$$Z_s = R_s + sL_s = [1 + j][\sigma \delta_s]^{-1} = [1 + j] \left[ \frac{\omega \mu_0}{2\sigma} \right]^{1/2}, \quad (6.60)$$

$$R_s = \left[ \frac{\omega \mu_0}{2\sigma} \right]^{1/2} = 2\pi \left[ \frac{10^{-7} f}{\sigma} \right]^{1/2} \equiv \text{surface resistance.}$$

At a frequency,  $f$ , of 0.3 THz we have for copper

$$R_s = 0.14 \, \Omega. \quad (6.61)$$

A transmission line model to estimate these losses is detailed in [74].

### 6.4.6 Switch Losses

The switch has length  $l_s$ , width  $w$ , and some thickness to be determined ( $\ll h$ ). The switch resistance depends on the carrier density generated by the fs laser. Compared

to the skin-effect resistance, the switch resistance can be somewhat larger and still achieve an acceptable  $Q$ .

Immediately we can see that the carrier lifetime can be a limitation depending on the antenna  $Q$ . At 0.3 THz, the period is 3.3 ps which gives 30 cycles in 100 ps corresponding to a  $Q$  of about 94. One may wish to choose  $h$  to get the number of cycles down to 30 or so (large  $h$  allows larger  $V_0$ ).

Assume as in Fig. 6.5 that  $l_s$  is small and can be modelled after closure by a resistance  $R_{sw}$  (time independent). As shown in Fig. 6.6 assume a folded antenna and ground plane.

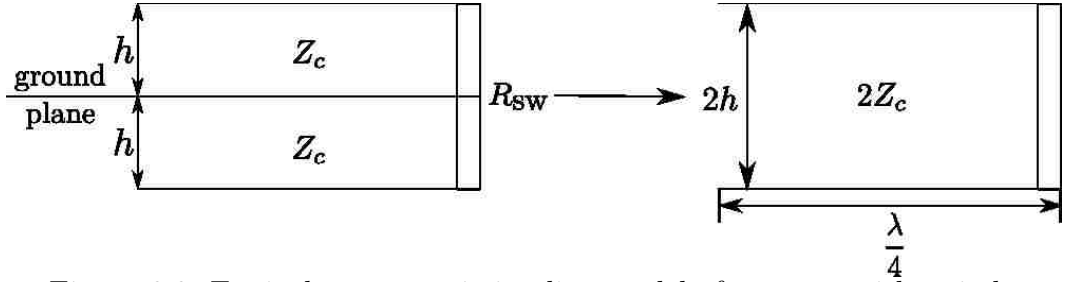


Figure 6.6: Equivalent transmission-line model of antenna with switch.

Here the reflection coefficient at  $R_{sw}$  is

$$\rho = \frac{2Z_c - R_{sw}}{2Z_c + R_{sw}} = \frac{1 - \frac{R_{sw}}{2Z_c}}{1 + \frac{R_{sw}}{2Z_c}} \approx 1 - \frac{R_{sw}}{Z_c}, \quad \text{for small } \frac{R_{sw}}{Z_c}. \quad (6.62)$$

In [73], the number of cycles to achieve  $e^{-1}$  is

$$N = -\frac{1}{2 \ln(\rho)} \approx \frac{Z_c}{2R_{sw}}, \quad (6.63)$$

$$Q = \pi N \approx \frac{\pi R_{sw}}{2 Z_c}.$$

How small should  $R_{sw}$  be?

Choose the parameters

$$\begin{aligned}
 Z_c &\approx Z_w \frac{h}{w}, \\
 h &< \frac{\lambda}{4} \text{ in dielectric,} \\
 Z_w &\approx Z_0 \epsilon_r^{-1/2}, \\
 \epsilon_r &\approx 3.
 \end{aligned} \tag{6.64}$$

Let  $w \approx \frac{\lambda}{4}$ ,  $h \approx \frac{\lambda}{8}$ , then

$$\begin{aligned}
 \frac{h}{w} &\approx \frac{1}{2}, \\
 2Z_c &\approx Z_w = \frac{377}{\sqrt{3}} \approx 218 \ \Omega.
 \end{aligned} \tag{6.65}$$

For  $N = 30$  we have

$$R_{\text{sw}} = \frac{Z_c}{2N} = \frac{Z_w}{4N} \approx \frac{377}{4\sqrt{3} \cdot 30} \approx 1.8 \ \Omega. \tag{6.66}$$

This can be used to estimate the SI-GaAs doping and fs laser parameters.

## 6.5 Discussion

This chapter has demonstrated the concept of a switched oscillator as a THz antenna. A first-order analytical formulation, which provides qualitative insight into the SwO antenna, has been presented. However, there are still many design optimization questions. One needs to maximize the stored energy depending on the dielectric thickness and switch dimensions. The antenna needs to radiate most of this energy, and there is a trade-off between amplitude and number of cycles ( $Q$ ). The skin-effect losses are not significant, but the switch losses need to be quantified and made acceptably small. These optimization considerations are extensively explored, using numerical simulation software, in the next chapter.

# Chapter 7

## Parameter Study of the SwO Antenna

*“Engg. Research Rule of Thumb: When in doubt, fit a curve.”*

The theoretical analysis of an idealized SwO presented in the previous chapter used several approximations to simplify the problem. As a result, an accurate quantitative relationship between the various parameters could not be obtained. Numerical simulation software, such as CST®MWS, can be used to study a more complete model of the SwO antenna, with fewer assumptions. Such a model would therefore provide a better understanding of the interdependence between various SwO parameters and the radiated fields. This chapter investigates the skin effect losses, substrate height ( $h$ ), relative permittivity of the substrate ( $\epsilon_{rs}$ ), switch length ( $l_s$ ) and antenna width ( $w$ ) parameters as a function of the radiation quality factor ( $Q$ ) and the resonant frequency ( $f_0$ ) using CST. A practical range of values is determined for each parameter which yields a large  $Q$  and high radiated power density while maintaining a dipole-like radiation pattern.

## 7.1 Validation of CST MWS®

In Ch. 6, Section 6.3, CST MWS® was used to demonstrate the SwO as a photoconductively switched antenna. Since similar simulation models will continue to be used to describe, explain and optimize the SwO antenna design, it is essential to validate our numerical results [83]. For this purpose, previously published experimental results for the 5-10-5 MAX1 (Hertzian dipole) antenna are used [6].

### 7.1.1 Determination of the Input Waveform for the 5-10-5 MAX1 Antenna

One of the most important parameters in modeling any antenna is the shape and rise time of the input pulse. A simple Drude formalism in [6] was used to estimate the shape of the current pulse in the photoconductive switch region for the 5-10-5 MAX1 antenna. The rise time of this pulse was approximately 60 fs. Such a fast rise time is unsuitable for our simulations since it leads to an unreasonably large number of mesh cells (and hence a very long simulation time). Therefore, to compare our numerical results against the analytical model in [6], an input pulse with a slower rise had to be used. A rise time of 0.5 ps was found to be appropriate. The task then is to determine an input pulse with a maximum rate of rise,  $t_{\text{mr}}$ , of 0.5 ps which matches the shape of the pulse in [6]. Note that the  $t_{\text{mr}}$  is used here as the definition of the rise time [84].

The Drude response in [6] evaluated to a double-exponential type function for the current in the photoconductive region. For our simulations it is more convenient to approximate this input with a Reciprocal-of-the-Sum-of-two-Exponentials Excitation (RSEE), as the RSEE transitions more smoothly at higher frequencies and hence

leads to a smaller simulation domain [84].

The RSEE is defined here as

$$f(t) = \frac{\chi}{\exp[-\alpha(t - t_0)] + \exp[\beta(t - t_0)]}, \quad \alpha \geq 0, \quad \beta \geq 0, \quad (7.1)$$

which is almost identical to the definition in [84], except for the  $\chi$  parameter which is included to scale the peak amplitude of the function. The parameters  $t_0$ ,  $\chi$  and  $\beta$  are estimated by fitting the RSEE to the analytical input excitation in [6].

For a  $t_{\text{mr}}$  of 0.5 ps, the analytical excitation published in [6] and the RSEE are compared in Fig. 7.1 [83]. One observes excellent agreement between the two curves. Note that fitting the RSEE input to the published data, i.e., the Drude model, implicitly takes into account the photoconductive switch properties (carrier mobility, carrier lifetime etc.) which are otherwise difficult to accurately model in CST.

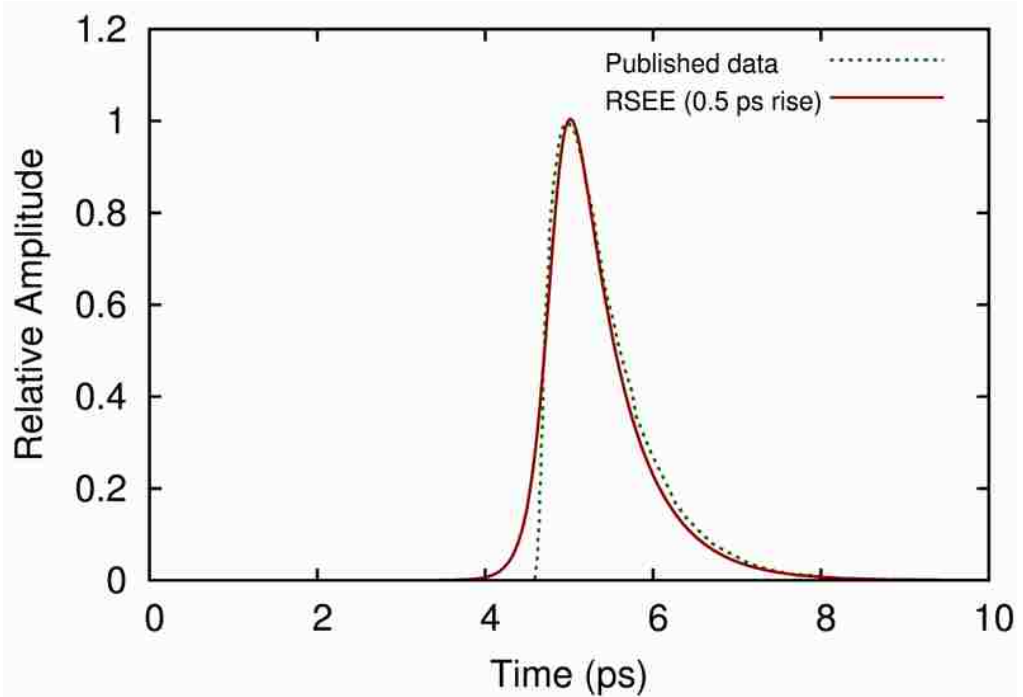
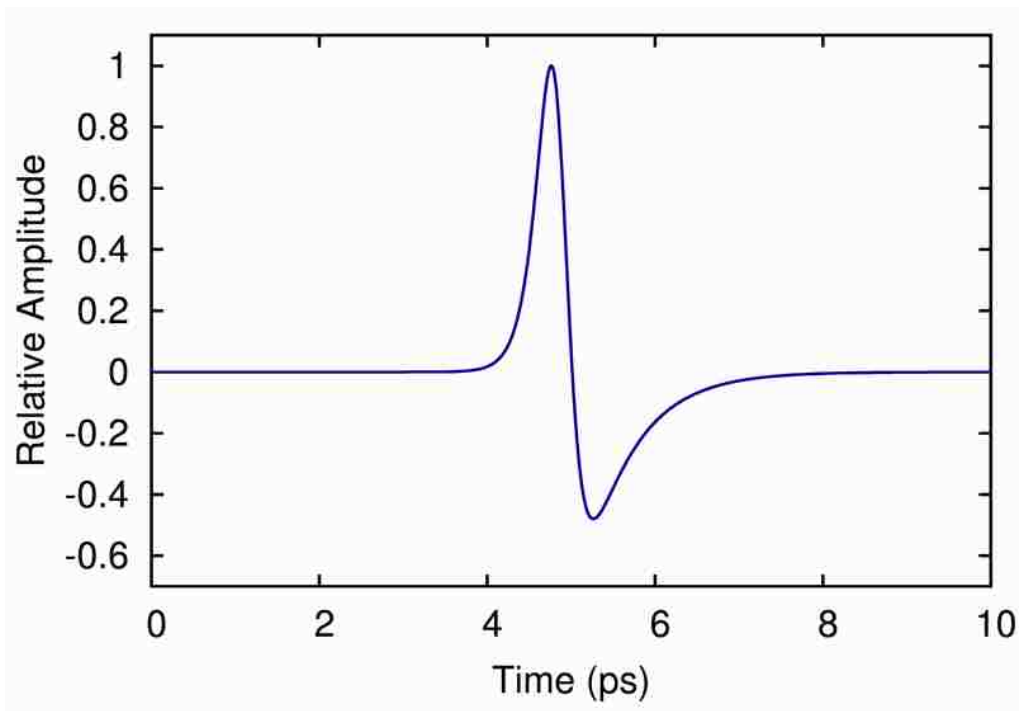
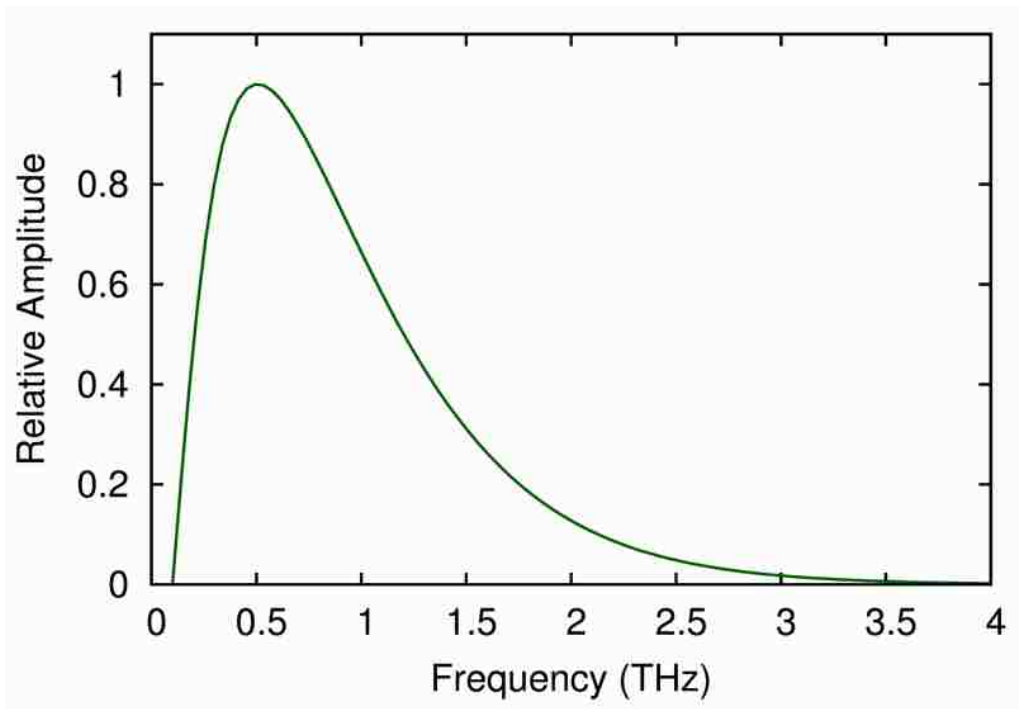


Figure 7.1: Comparison of the analytical excitation published in [6] and the RSEE with a  $t_{\text{mr}}$  of 0.5 ps.



(a) Shape of radiated pulse; derivative of the input excitation.



(b) Frequency spectrum (Fourier Transform) of Fig. 7.2(a).

Figure 7.2: Shape of radiated electric field and its Fourier transform.

As mentioned in [6], the shape of the radiated pulse is identical to the derivative of the input excitation. The normalized derivative of the RSEE is shown in Fig. 7.2(a).

The 5-10-5 MAX1 antenna is a broadband radiator and the experimental results in [6] are compared to the analytical approximations in the frequency domain. The normalized Fourier transform of Fig. 7.2(a), shown in Fig. 7.2(b), is therefore of more interest since a good agreement between our simulation results and Fig. 7.2(b) implies good agreement with published experimental data.

## 7.1.2 Results

A simplified subset of the problem is solved as the original dimensions and the experimental setup of the 5-10-5 MAX1 antenna in [6] lead to a very large simulation domain. Details of the simplifications and simulation setup are provided in [83].

The normalized analytical waveform, Fig. 7.2(a), and numerical simulation result for the far-field electric field ( $E_y$ ), at  $r = 1.0$  cm, in the time domain, are compared in Fig. 7.3. One observes excellent agreement between the two curves.

Corresponding results in the frequency domain are compared in Fig. 7.4 (Fourier transform of the curves in Fig. 7.3). Again, one notes good agreement between the two curves. The peak frequency, 0.5 THz, in the simulation results differs only by  $\approx 0.1$  THz from that predicted analytically. The experimental frequency domain response in [6] was also found to agree very well with the predicted analytical response. This implies an excellent agreement between our simulation results and the experimental results in [6].



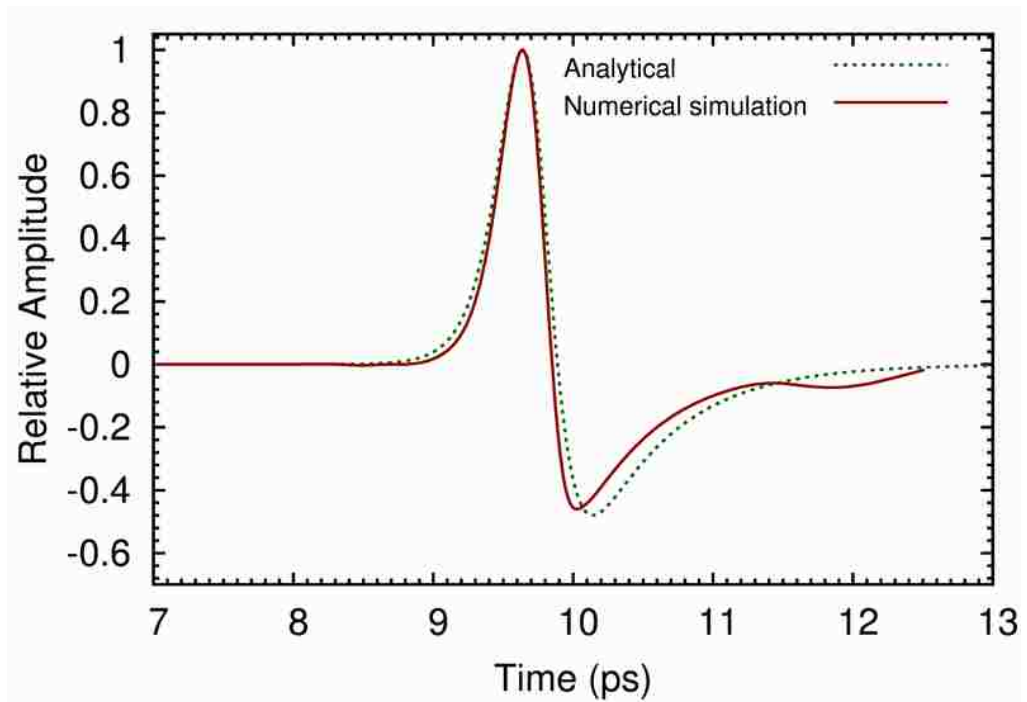


Figure 7.3: Comparison of the normalized analytical and numerical simulations results for the electric field ( $E_y$ ).

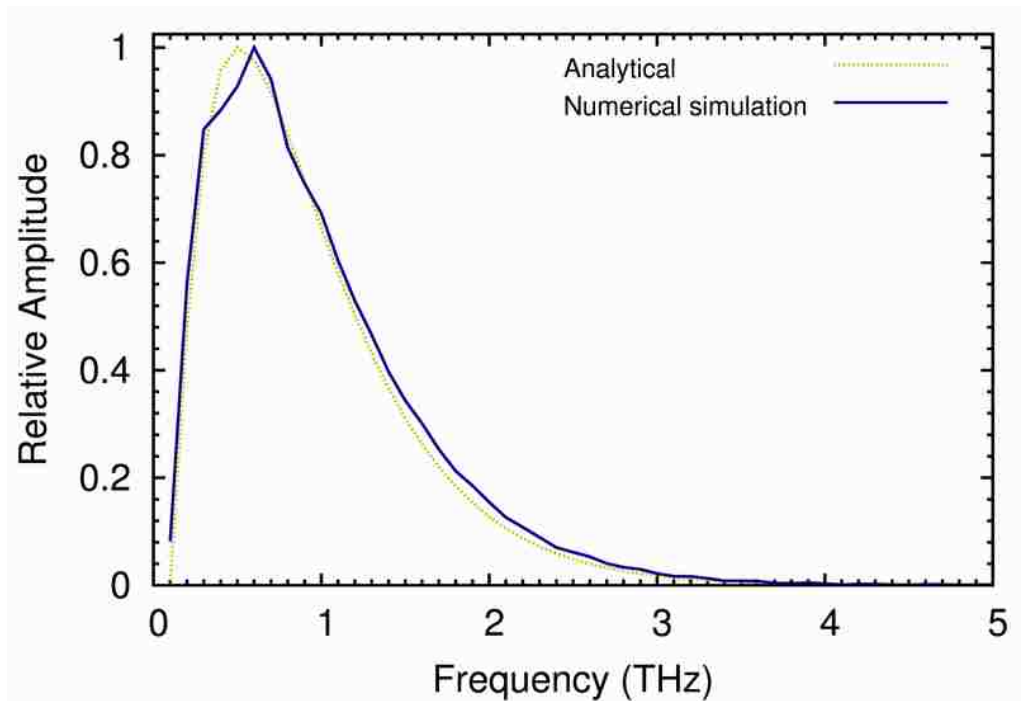


Figure 7.4: Comparison of the normalized analytical and numerical simulations results for the electric field ( $E_y$ ) in the frequency domain (FFT of Fig. 7.3).

## 7.2 Determination of the Input Waveform for the SwO Antenna

The input to the SwO antenna is a ramp rising step with a  $t_{mr}$  corresponding to the desired rise time. An ideal ramp rising input, as used in Ch. 6, Sec. 6.3, and [72], gives very approximate results. This is because the sharp “knee” in such a waveform leads to inaccuracies at higher frequencies. Therefore, an input function which transitions smoothly from higher to lower frequencies is desired as it not only leads to more accurate simulations but also reduces the size of the simulation domain. A logistic function with a  $t_{mr}$  of 0.5 ps was found to lead to a reasonable number of mesh cells [85]. A plot of the input waveform is shown in Fig. 7.5.

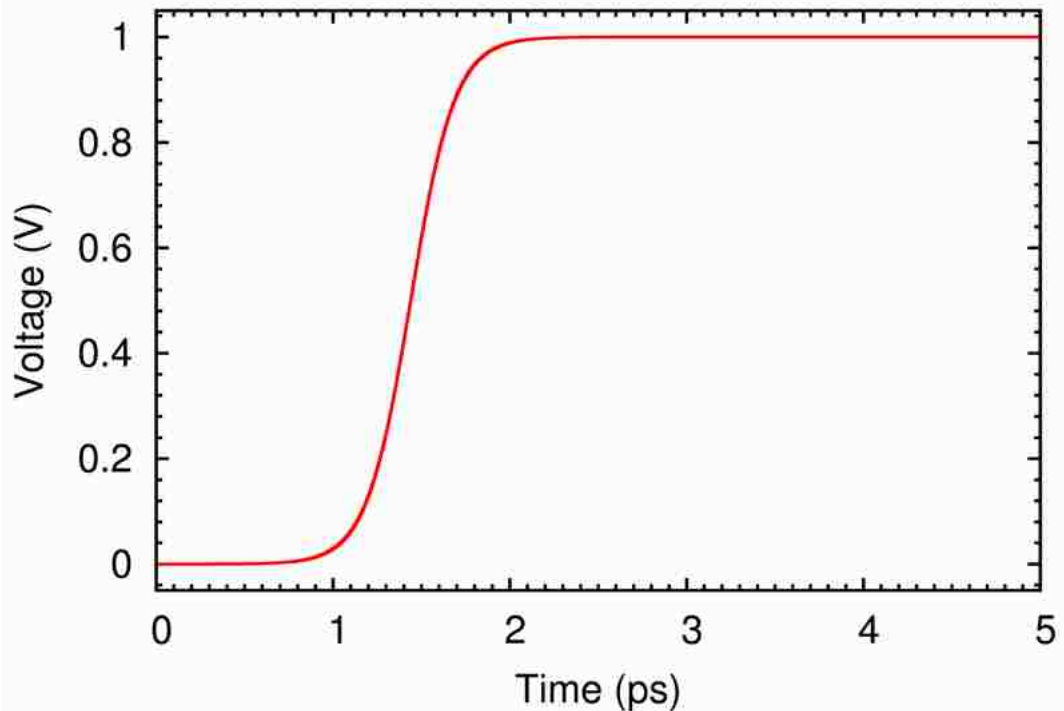


Figure 7.5: Logistic input voltage waveform, with a  $t_{mr}$  of 0.5 ps, for the SwO antenna.

### 7.3 Simulation Setup

To investigate the interdependence between various parameters a “reference” SwO is used, and each parameter is varied while others are kept fixed. A copper SwO above a copper ground plane with a polyethylene substrate medium,  $\epsilon_{rs} = 2.25$ , with the dimensions in Table 7.1 was (arbitrarily) chosen as the reference. The dimensions correspond to a frequency of 0.5 THz, i.e.,  $\lambda = \lambda_0 = 600 \mu\text{m}$ . Ideally, one desires a substrate with a relative permittivity as close to air as possible to avoid losses, mostly due to impedance mismatches and surface waves. Polyethylene was chosen as it has a low relative permittivity, is readily available and lends itself easily to fabrication. The substrate is assumed to be lossless and dispersionless. The wavelength, in the substrate medium is reduced as  $\lambda = \lambda_0/\sqrt{\epsilon_{rs}} = (2/3)\lambda_0$ .

Table 7.1: Dimensions of a “reference” copper SwO above a copper ground plane with a (lossless) polyethylene substrate medium.

Parameter	Dimensions ( $\mu\text{m}$ )
Antenna length, $l_a$	$\lambda/2 = 200$
Antenna height (thickness)	1
Switch length, $l_s$	$\lambda/50 = 8$
Antenna width, $w$	$(l_a - l_s)/2 = 144$
Height of substrate, $h$	$\lambda/8 = 50$
Length of substrate and ground plane	$3\lambda = 1200$
Width of substrate and ground plane	$3\lambda = 1200$
Height of ground plane (thickness)	1

The SwO simulation structure and orientation are similar to that in Fig. 6.2 (Ch. 6, Sec. 6.3). As in Ch. 6, Sec. 6.3, a far-field electric field probe oriented in the  $+y$  direction at a distance of 1 cm from the origin on the  $z$ -axis, was used to monitor the electric fields radiated by the antenna. Further details of the simulation setup, probe placements and CST simulation parameters are given in [85]. For simulation results presented in the rest of this chapter, the setup and antenna dimensions in

this section are to be considered as the default, unless mentioned otherwise.

Having established that CST MWS® can reliably reproduce experimental data, determine the appropriate input waveform, and setup a reference simulation domain, let us now proceed with the parameter study of the SwO. The approach adopted here does not consider the physics of the PC-switch region (carrier lifetime, carrier mobility, etc.). Nevertheless, the idealized (perfect) switch assumed provides valuable insight into the relationships between various parameters of interest.

## 7.4 Investigation of the Skin-Effect Losses in a Copper SwO Antenna Above a Copper Ground Plane

The skin-effect losses are determined by comparing the radiation  $Q$ s for PEC and copper SWOs. The simulation setup is identical to that described in the previous subsection except that there is no substrate medium, i.e., vacuum between the SwO and ground plane.

The radiation  $Q$  as a function of  $h$  for the PEC and copper cases are compared in Fig. 7.6. The analytical points, calculated using the formulas in Ch. 6, Sec. 6.4, for the extrema,  $h = \lambda/4$  and  $h = \lambda/20$  ( $h \ll \lambda/4$ ), are also indicated for reference [85].

As expected from the formulae in the previous chapter, Sec. 6.4, the  $Q$  increases as  $h$  is decreased for both the PEC and copper cases. This increase in  $Q$  can also be understood, at least in part, due to the corresponding increase in the stored

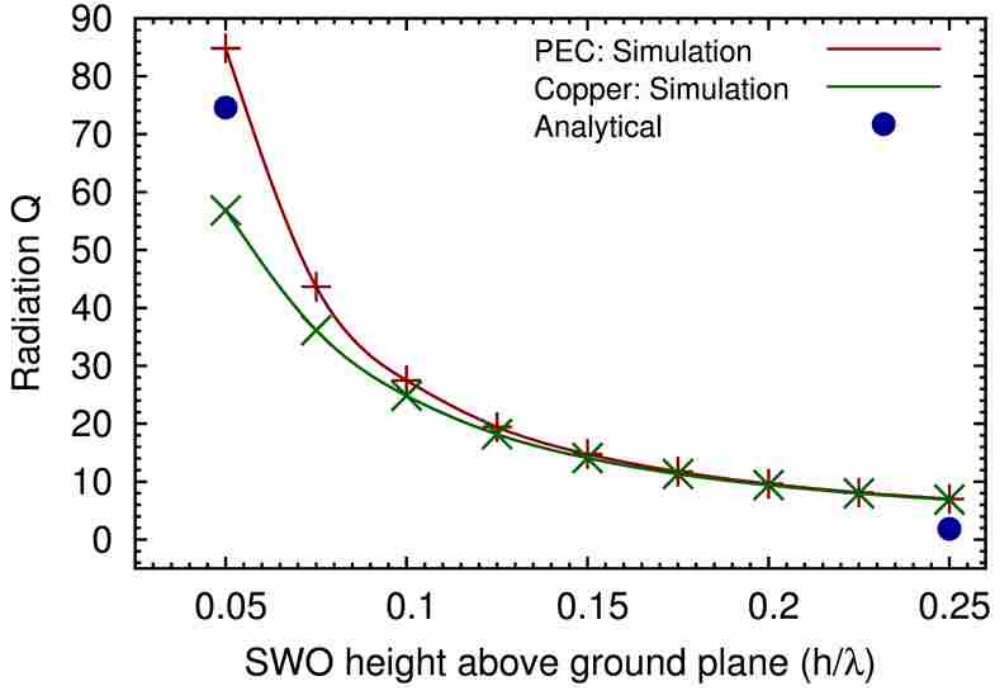


Figure 7.6: Comparison of the quality factors as a function of the SwO height above the ground plane for PEC and copper.

capacitive energy, i.e.,

$$U_0 = 2CV_0^2 = 2 \left( \frac{\epsilon_0 A}{h} \right) V_0^2 \quad \therefore \downarrow h \Rightarrow \uparrow C \Rightarrow \uparrow U_0 \Rightarrow \uparrow Q, \quad (7.2)$$

where  $A = wl_a$  is the area of the SwO. From Fig. 7.6 one also observes that the resistive losses,  $R_s$ , are not a concern for  $h \gtrsim \lambda/10$ . However, for  $h \lesssim \lambda/10$  the skin-effect losses significantly reduce the  $Q$ .

## 7.5 $Q$ and $f_0$ as a function of $h$

We now extend the previous study to include the polyethylene substrate medium. This section explores  $Q$  and  $f_0$  as a function of the height of the substrate between a copper SwO and a copper ground plane. We wish to optimize  $h$  so as to obtain the desired  $Q$  while maximizing the radiated power.

The  $Q$ s with and without the substrate are compared in Fig. 7.7. The results are almost identical. An empirical relation between  $Q$  and  $h/\lambda$ , determined by fitting a

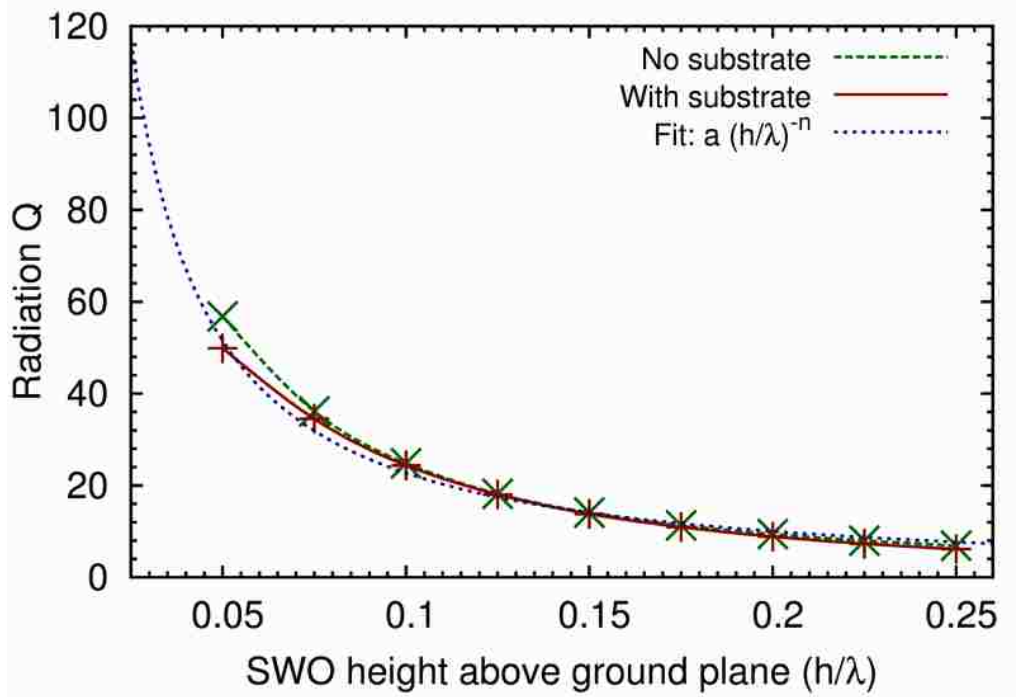


Figure 7.7: Comparison of quality factors ( $Q$ ), as a function of the SwO height above the ground plane, with and without the polyethylene substrate medium. A function is fit to the results, with the substrate, to obtain an empirical relation between  $Q$  and  $h$ .

curve to Fig. 7.7, is,

$$Q(h/\lambda) \approx \frac{3}{2} \left[ \frac{h}{\lambda} \right]^{-6/5}, \quad 0.05 \leq \frac{h}{\lambda} \leq 0.25, \quad (7.3)$$

where the fitting curve is based on a generalized form of (7.2). For two arbitrary configurations,  $\alpha$  and  $\beta$ , we have

$$\frac{Q_\alpha^n}{Q_\beta^n} = \left[ \frac{h_\alpha/\lambda_\alpha}{h_\beta/\lambda_\beta} \right]^{-6/5}, \quad (7.4)$$

i.e.,  $h_\alpha/\lambda_\alpha = h_\beta/\lambda_\beta \Rightarrow Q_\alpha = Q_\beta$  regardless of the substrate medium used, which explains the identical results for  $Q$ , with and without the substrate, in Fig. 7.7. This

can also be explained using (7.2) as,

$$U_0 = 2 \left[ \frac{\epsilon_0 \epsilon_{rs} w l_a}{h} \right] V_0^2 \propto 2 \left[ \frac{\epsilon_0 \epsilon_{rs} \left( \frac{\lambda_0^2}{\epsilon_{rs}} \right)}{h} \right] V_0^2 \propto 2 \left( \frac{\epsilon_0 \lambda_0^2}{h} \right) V_0^2, \quad (7.5)$$

i.e.,  $Q$ , which is correlated to  $U_0$ , is independent of the relative permittivity of the substrate medium,  $\epsilon_{rs}$ .

For the range of  $h$  investigated, it is also observed that there is little deviation in  $f_0$  compared to that in  $Q$ . The mean  $f_0$  is 0.371 THz with a standard deviation of 0.0074 [86].

Besides the quality factor, a second constraint on the substrate height is imposed by the *duration* of the radiation,  $\tau$ , i.e., the time taken for the far-field electric field to completely decay to zero. This is dictated by the lifetime of the carriers in the photoconductive region of the switch. As mentioned previously, we use SI-GaAs, which has a carrier lifetime in the 50-100 ps range. Imposing the constraint that  $\tau \leq 100$  ps gives [86]

$$0.05 \leq \frac{h}{\lambda} \leq 0.100 \Rightarrow 25 \leq Q \leq 50, \quad (7.6)$$

## 7.6 $Q$ and $f_0$ as a function of $\epsilon_{rs}$

The relative permittivity of the substrate medium is varied from  $\epsilon_{rs} = 2.0$  to  $\epsilon_{rs} = 10.0$ , a range of practical interest. The substrate medium is assumed to be lossless and dispersionless for all  $\epsilon_{rs}$ . Fig. 7.8 shows a plot of  $f_0$  versus  $\epsilon_{rs}$ .

A simple fit relation between  $f_0$  and  $\epsilon_{rs}$  is obtained as,

$$f_0(\epsilon_{rs}) \approx \frac{\sqrt{\epsilon_{rs}}}{4} \text{ THZ}, \quad 2 \leq \epsilon_{rs} \leq 10. \quad (7.7)$$

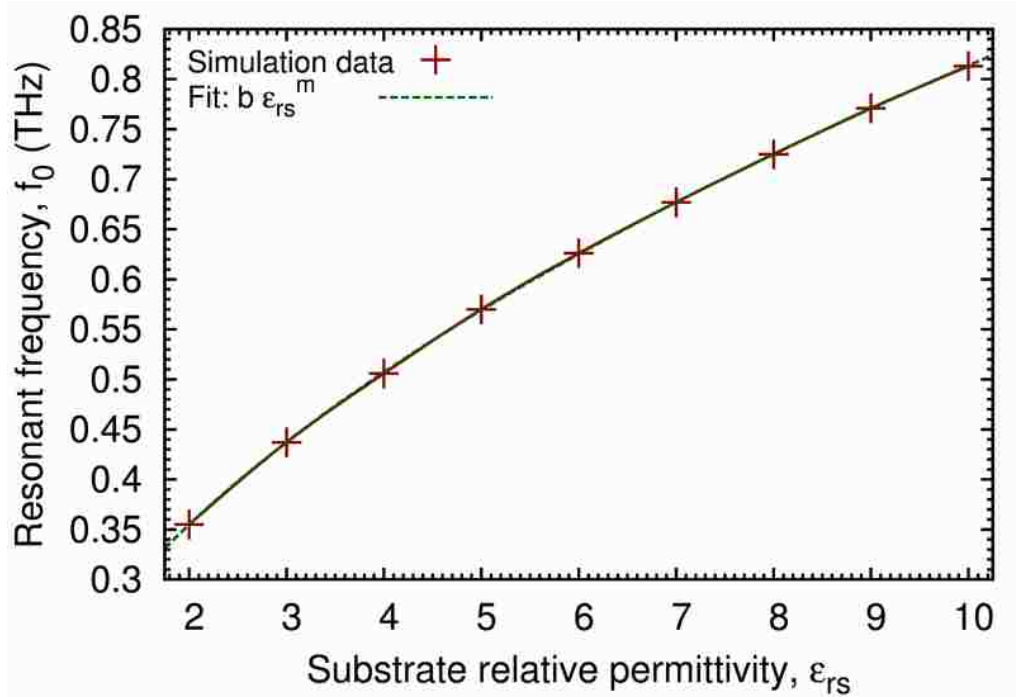


Figure 7.8: The resonant frequency,  $f_0$ , as a function of the relative permittivity of the substrate medium,  $\epsilon_{rs}$ . A function is fit to the results to obtain an empirical relation between  $f_0$  and  $\epsilon_{rs}$ .

The SwO dimensions are scaled relative to the wavelength in each substrate medium and the overall size of the SwO therefore decreases with an increase in  $\epsilon_{rs}$ . Since losses from surface waves and impedance mismatches increase with an increase in  $\epsilon_{rs}$ , a smaller SwO radiates less energy compared to a larger SwO. Hence, a small  $\epsilon_{rs}$  (large SwO) is more desirable to maximize the radiated energy. As shown in (7.5), the  $Q$  is independent of  $\epsilon_{rs}$  [86].

Note that we have only considered  $\epsilon_{rs}$  and not the *effective* relative permittivity ( $\epsilon_{re}$ ) that is conventionally used in the study of microstrip patch antennas.  $\epsilon_{re}$  is a function of  $\epsilon_{rs}$ , the relative permittivity of the surrounding free space medium ( $\epsilon_{r0} = 1$  in our case),  $h, l_s, w$  and is, in general, not trivial to determine. Nevertheless, all formulas containing  $\epsilon_{rs}$  can be expressed in terms of  $\epsilon_{re}$  if desired. If  $h, l_s$  and  $w$  are fixed, as in this section, then  $\epsilon_{re}$  is only a function of  $\epsilon_{rs}$  and  $\epsilon_{r0}$ , i.e.,  $f_0(\epsilon_{rs}) \Rightarrow$



$$f_0(\epsilon_{re}, \epsilon_{r0}).$$

Unlike the parameter  $h$  and  $\epsilon_{rs}$  investigated above, the effects of  $l_s$  and  $w$  on  $Q$  and  $f_0$  are too complicated to assess theoretically. Analytical approximations in the previous chapter, Sec. 6.4, simplified the problem by assuming that the switch gap length was much less than the antenna length,  $l_s \ll l_a$ , and that  $w \approx \lambda/4$ . The following sections investigate the effects of  $l_s$  and  $w$  on the radiation quality factor and the resonant frequency of the SwO.

## 7.7 $Q$ and $f_0$ as a function of $l_s$

The switch length is important as it ultimately dictates the requirements of the laser beam incident on the photoconductive switch region. The switch length,  $l_s$ , is varied from  $l_s = \lambda/50$  to  $l_s = \lambda/5$ . Also, the width of the antenna is fixed at  $w = l_a/2 = \lambda/4$ , i.e.,  $w \neq (l_a - l_s)/2$  as in Table 7.1.

Figure 7.9 and Fig. 7.10 show a plot of  $Q$  and  $f_0$  as a function of  $l_s$ . Empirical relations between  $Q$ ,  $f_0$  and  $l_s$  are,

$$Q \left( \frac{l_s}{\lambda} \right) \approx 125 \sqrt{\frac{l_s}{\lambda}}, \quad \frac{1}{50} \leq \frac{l_s}{\lambda} \leq \frac{1}{5}, \quad (7.8)$$

$$f_0 \left( \frac{l_s}{\lambda} \right) \approx 0.22 \left[ \frac{l_s}{\lambda} \right]^{-0.15}, \quad \frac{1}{50} \leq \frac{l_s}{\lambda} \leq \frac{1}{5}. \quad (7.9)$$

The results in Fig. 7.9 are interesting as they suggest that for a fixed  $h$ ,  $\epsilon_{rs}$  and  $w$ , the  $Q$  can be increased by increasing the switch length. However, we must also ensure that the time taken for the radiated electric field to decay to zero,  $\tau$ , is less than 100 ps. Imposing this second constraint we have [87]

$$0.025 \leq \frac{l_s}{\lambda} \leq 0.075 \Rightarrow 20 \leq Q \leq 35. \quad (7.10)$$

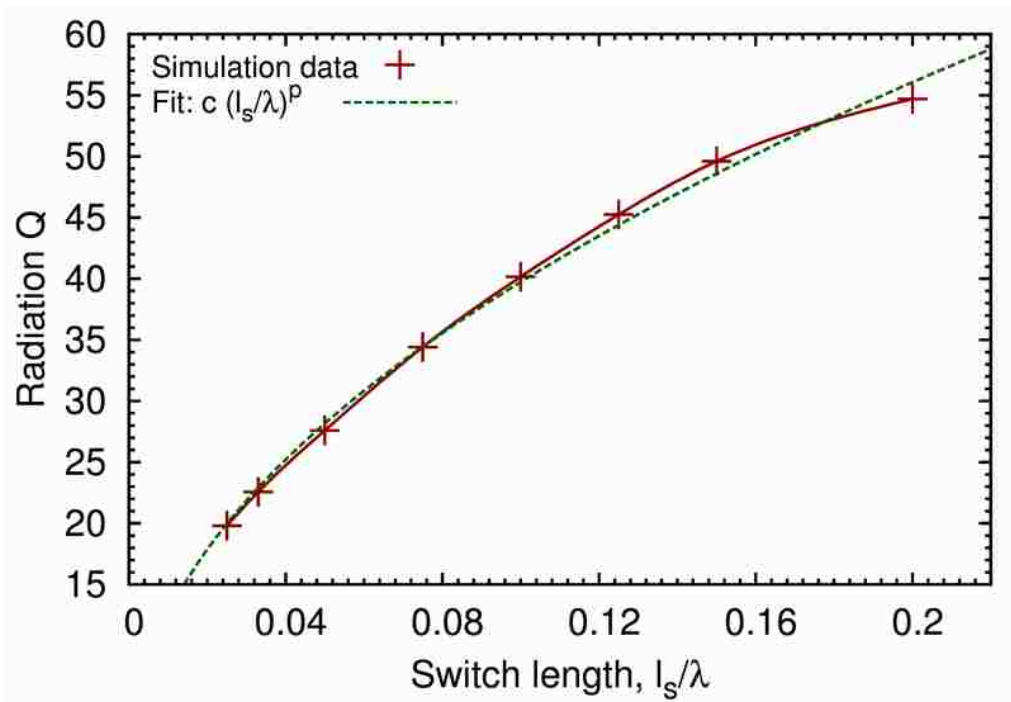


Figure 7.9: The quality factor,  $Q$ , as a function of the switch length,  $l_s$ . A function is fit to the results to obtain an empirical relation between  $Q$  and  $l_s$ .

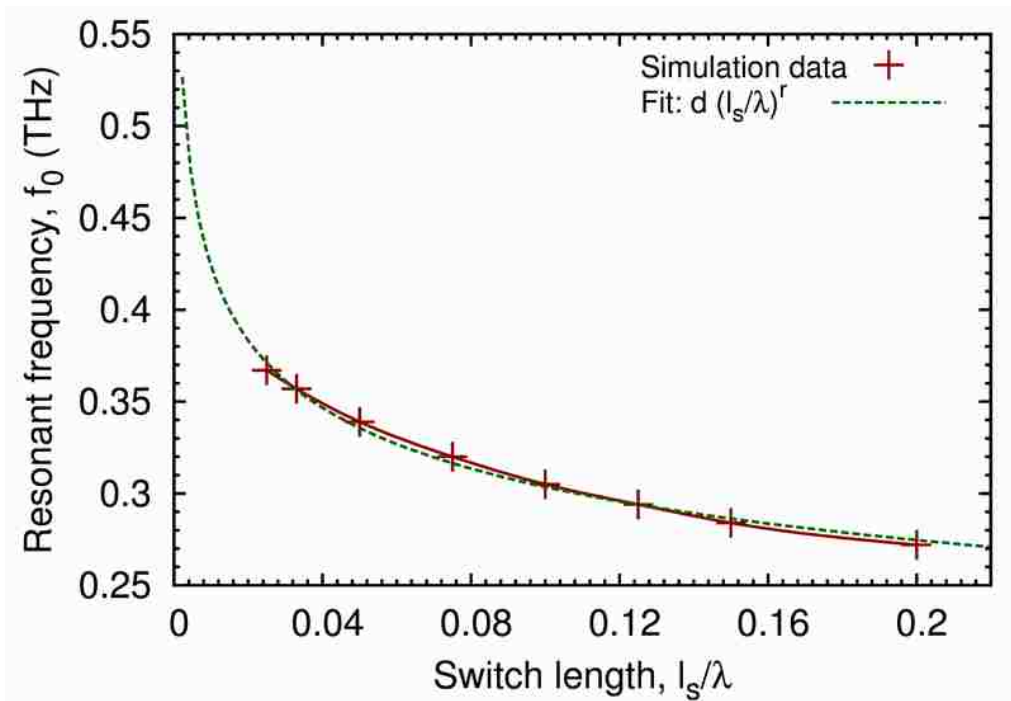


Figure 7.10: The resonant frequency,  $f_0$ , as a function of the switch length,  $l_s$ . A function is fit to the results to obtain an empirical relation between  $f_0$  and  $l_s$ .

Note that compared to varying  $h$ , varying  $l_s$  to increase the  $Q$  has the disadvantage that the resonant frequency also changes, since  $f_0$  is also a function of  $l_s$ . Moreover, we have from Sec. 7.5,

$$0.05 \leq \frac{h}{\lambda} \leq 0.100 \Rightarrow 25 \leq Q \leq 50, \quad (7.11)$$

i.e., a higher  $Q$  is obtained by varying  $h$  than that obtained by varying  $l_s$ . Nevertheless, increasing  $l_s$  may be attractive from an experimental perspective as the voltage hold-off is dictated by  $l_s$  and not  $h$ , since, typically,  $l_s \ll h$ . Increasing  $l_s$  would therefore imply a higher input voltage, which is desirable.

## 7.8 $Q$ and $f_0$ as a function of $w$

The antenna width is important as it determines the modes that can be sustained by the radiator. The primary aim in optimizing  $w$  is to eliminate unwanted modes to obtain the desired  $Q$  and maximize the radiated power density,  $P_{\text{rad}}$ . The antenna width,  $w$ , is varied from  $w = \lambda/20$  to  $w = \lambda$ .  $w$  can be considered to represent the inductance of the antenna, i.e., smaller  $w \Rightarrow$  larger inductance.

Figure 7.11 and Fig. 7.12 show a plot of  $Q$  and  $f_0$  as a function of  $w$ . There is a large variation of both, the  $Q$  and  $f_0$  with  $w$ . The fit relations for this case are,

$$Q\left(\frac{w}{\lambda}\right) \approx 36 \left[\frac{w}{\lambda}\right]^{1.35} + 14, \quad \frac{1}{20} \leq \frac{w}{\lambda} \leq 1, \quad (7.12)$$

$$f_0\left(\frac{w}{\lambda}\right) \approx -0.35\sqrt{\frac{w}{\lambda}} + 0.6, \quad \frac{1}{20} \leq \frac{w}{\lambda} \leq 1. \quad (7.13)$$

Again, an increase in  $Q$  with an increase in  $w$  can be inferred from (7.2). Imposing the constraint of the decay time of the radiated electric field, i.e.,  $\tau \leq 100$  ps, the width of the antenna is constrained as  $w < \lambda/2$  [87].

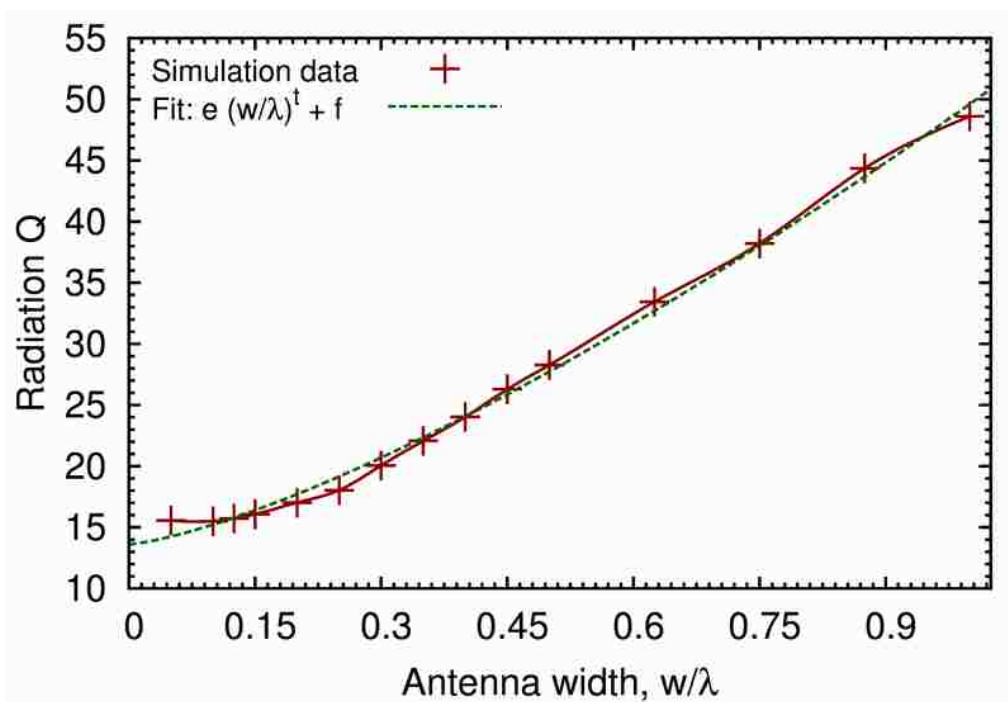


Figure 7.11: The quality factor,  $Q$ , as a function of the switch length,  $w$ . A function is fit to the results to obtain an empirical relation between  $Q$  and  $w$ .

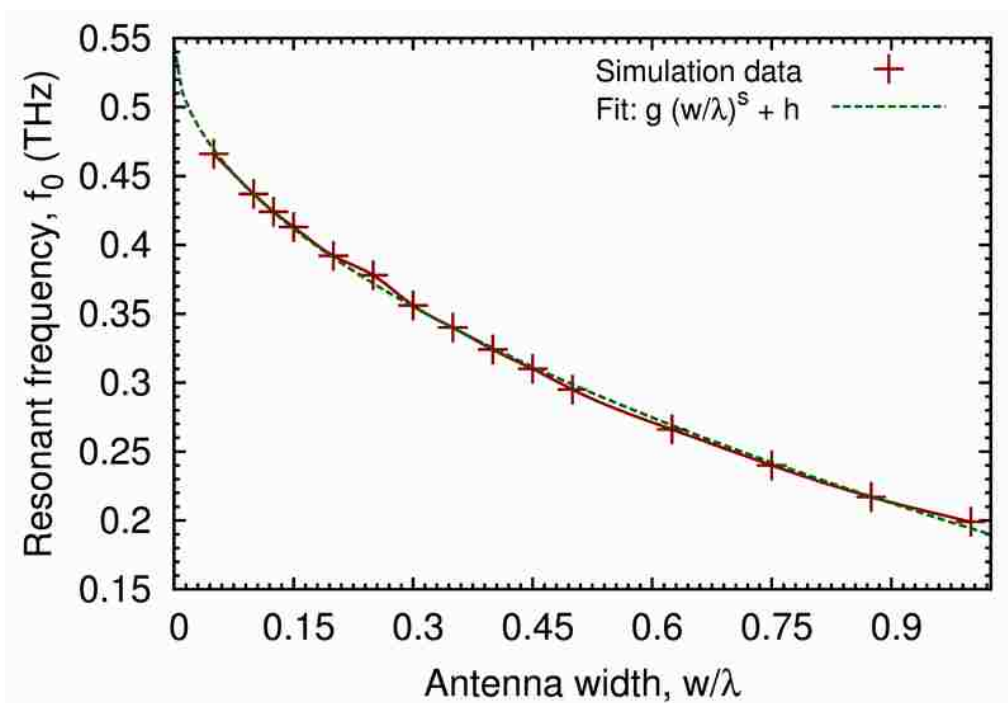


Figure 7.12: The resonant frequency,  $f_0$ , as a function of the antenna width,  $w$ . A function is fit to the results to obtain an empirical relation between  $f_0$  and  $w$ .

The radiation  $Q$ s and peak radiated power densities (at  $r = 1$  m in the  $\theta = 90^\circ$  plane) for various  $w$  are compared in Fig. 7.13. It is clear that the radiated power density is maximum at  $w = \lambda/8$  and  $w = \lambda/2$ . At these widths, the peak radiated power is approximately 10 times that at  $w = \lambda/4$ . Since  $w < \lambda/2$ , the most suitable choice for the antenna width is  $w = \lambda/8$ . An additional advantage of using the smaller width is its propensity to disallow the propagation of higher order modes. The  $Q$  of the system can then be increased by increasing the switch length,  $l_s$ , as in Sec. 7.7.

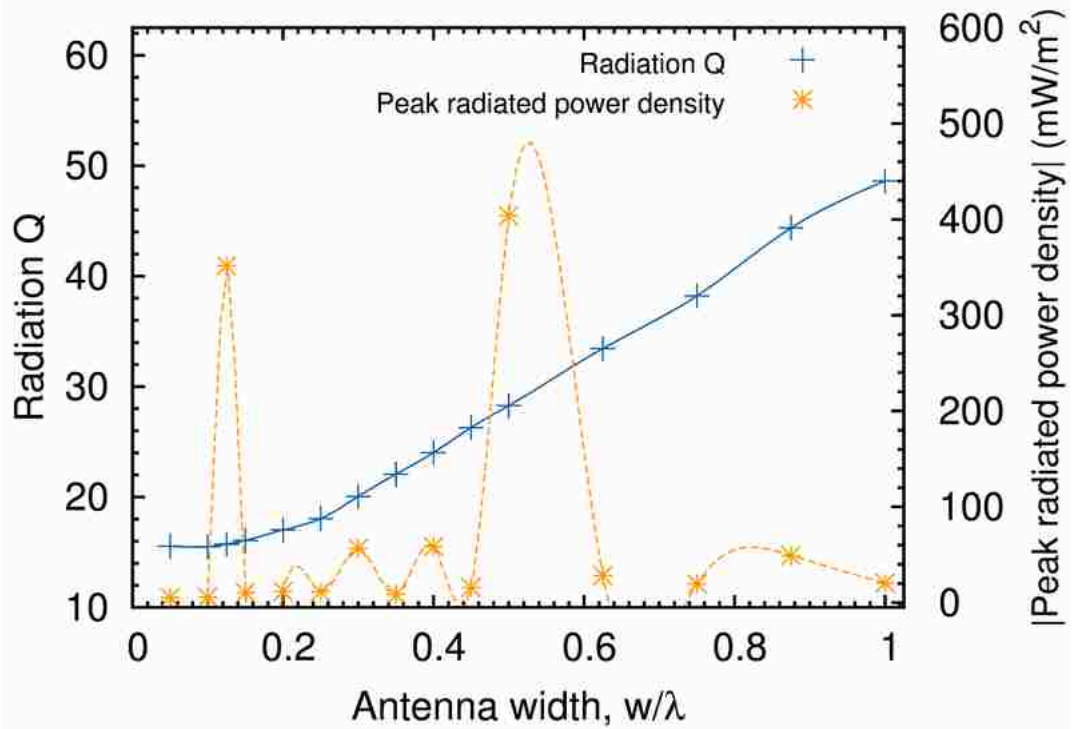


Figure 7.13: Comparison of the quality factor and the peak radiated power density (at  $r = 1$  m) as a function of the antenna width.

## 7.9 Summary

The empirical fit relations for the various parameters are summarized in Table 7.2. For all the  $h$ ,  $\epsilon_{rs}$ ,  $l_s$  and  $w$  values investigated it was observed that far-field radiated

power density patterns, at the respective resonant frequencies, are dipole-like [86, 87]. Additionally, for  $h, \epsilon_{rs}$  and  $l_s$ , the peak radiated power density is, for all values explored, less than  $30 \text{ mW/m}^2$ . This is approximately 500% less than that observed for  $w = \lambda/8$  and  $w = \lambda/2$ . Clearly, the antenna width plays the most crucial role in the SwO design.

Table 7.2: Summary of parametric study of the SwO.

Parameter	Range	Empirical Relations	
		$Q$	$f_0$
$h$	$\frac{\lambda}{20} \leq h \leq \frac{\lambda}{4}$	$\frac{3}{2} \left[ \frac{h}{\lambda} \right]^{-\frac{6}{5}}$	Constant
$\epsilon_{rs}$	$2 \leq \epsilon_{rs} \leq 10$	Constant	$\frac{\sqrt{\epsilon_{rs}}}{4}$
$l_s$	$\frac{\lambda}{50} \leq l_s \leq \frac{\lambda}{5}$	$125 \sqrt{\frac{l_s}{\lambda}}$	$0.22 \left[ \frac{l_s}{\lambda} \right]^{-0.15}$
$w$	$\frac{\lambda}{20} \leq w \leq \lambda$	$36 \left[ \frac{w}{\lambda} \right]^{1.35} + 14$	$-0.35 \sqrt{\frac{w}{\lambda}} + 0.6$

The empirical relations in Table 7.2 are constrained as they apply only to specific SwO dimensions, since only one parameter is varied at a time. Nevertheless, these results provide valuable quantitative insight, and a much needed starting point, for the antenna design. Of course, once a SwO design is known to resonate at some frequency, the length of the antenna elements may be rescaled so that the resonant frequency of the SwO is at the desired transmission frequency.

## 7.10 Future Work

The SwO antenna presents a unique approach to a THz radiator design. However, only a simplified model of the SwO has been assumed in this paper. There are many other factors to consider before a working model of the SwO antenna can be realized. A few of these considerations are addressed here.

The theory in the previous chapter, Sec. 6.4, and the numerical simulations in this chapter have assumed an idealized switch, i.e., the resistivity of the switch has not been taken into account. This in turn depends on the photoconductive properties of the switch region (carrier lifetime, carrier mobility etc.) which have to be determined through experiments. An analytical formulation of the switch current or switch voltage, similar to that in [6], which accurately models the physics of the switch region must be incorporated into the simulations. This would also help determine the amount of laser energy required to achieve the desired  $Q$  and radiated power density.

Several other factors such as surface waves, voltage hold-off etc., will have to be considered in the context of the physical realization of the device. As an example, physical limitations imposed by the voltage hold-off may require the SwO design to be altered (such as using a superstrate to increase the voltage hold-off). Dielectric lenses may also be used to increase the directivity of the radiated beam.

Once a working prototype of the SwO antenna has been developed, the power and directivity of the resulting beam can be further increased by using arrays. The SwO can be used in conjunction with other configurations, such as zig-zag antennas [88, 89], or as individual elements of the array [90]. The new challenges, such as input feed, mutual coupling etc., associated with arrays would also have to be addressed. By including focusing reflectors or lenses, a THz beam can propagate to distances of approximately 1 km, limited by atmospheric attenuation [91].

With voltages on the order of 100 V on the transmitting switched oscillator, one can envision radiated powers on the order of some tens of watts from a single antenna. An array of such elements increases this by the number of elements  $N$  in the array (say 25 or 100) [91]. Of course this lasts for a very short time. For 30 cycles at 0.3 THz this lasts for 100 ps, so the total energy is small with, say, 20 W multiplied by  $10^{-8}$ s times  $N$ , putting us in the  $\mu$ J range. The average power depends on the PRF (pulse repetition frequency). A PRF of 1 MHz puts the average power in the Watt range.

One also needs to receive the THz bursts (e.g. damped sinusoidal pulses) in a manner which retrieves the information contained in a string of such pulses (e.g. pulse-code modulation) [92]. One approach to this problem is to rectify the RF burst. For example, if one had about 30 cycles at 0.3 THz, this would give a pulse of about 0.1 ns (or 100 ps) wide. This corresponds to a half period at about 5 GHz which can be handled by existing microwave technology.

One can take the incoming THz beam and handle it in a way similar to the transmitting antenna. (Good transmitting antennas make good receiving antennas). Using a paraboloidal reflector (in perhaps a Cassegrain configuration [91]) the THz beam can be concentrated on the small THz antennas. The signal from the latter can be rectified to come out at a much lower frequency which still retains the information.



# Chapter 8

## Conclusions

42.

- *Douglas Adams, The Hitchhiker's Guide to the Galaxy.*

This dissertation has presented two EMP/HPE devices designed for specific biological and terahertz applications, the PSIRA and the SwO.

Analytical calculations, numerical simulations and experimental results on a five-layer, hemispherical, dielectric focusing lens have been detailed. Such a lens is used at the second focal point of the PSIRA to better match the focused pulses into the (biological) target medium. Electromagnetic enhancements from the experiments were found to agree well with those obtained from numerical simulations. However, losses in the lens materials reduce the peak amplitude of the focal impulse and increase the beam width, both of which are undesirable. As mentioned in Ch. 4, Sec. 4.7, perhaps the most immediate practical challenge is to explore new materials for the lens which are negligibly lossy in the 0-10 GHz range. By comparing the focal impulse waveforms in air and in the lens, in the spectral domain, it was also found that the focusing lens acts as a bandpass filter from approximately 0.4-3.4 GHz.

## Chapter 8. Conclusions

Heuristic methods used to design and explore various switch configurations, with the primary objective of maximizing the peak focal impulse amplitude with a small compromise in the spot size, were outlined. The center of the switch is located at the first focal point which leads to a simpler design than that explored previously. After narrowing the acceptable switch configurations, the pressure vessel and hydrogen chamber were integrated into the system. As mentioned in Ch. 5, Sec. 5.6, the pressure vessel and hydrogen chamber are required for input voltages of 100 kV or more, to effectively launch a spherical TEM wave from the first focal point. The use of the pressure vessel as the launching lens further simplifies the design of the switch system. Spherical and cylindrical pressure vessel designs were investigated and both were found to be viable candidates. Again, there remain many practical challenges in the experimental realization of the system and the corresponding measurements associated with the high-voltages and fast rise times.

The PSIRA system described is conceptually complete. Despite the obvious challenges, it is hoped that the studies in this dissertation will stimulate further experimental investigation in this field.

Compared to the PSIRA, the research on the SwO antenna is still in its nascent stages. Conventionally, the SwO has been used to radiate high-power pulses in the MHz range. The adaptation of the SwO as an antenna to radiate pulses in the THz range is a unique and novel proposition. Analytical calculations for the SwO have been detailed. It has been shown that the two plates of the SwO, above a ground plane, can be considered as two capacitors in series. The SwO is also analyzed as two dipole radiators, which helps in the calculation of various parameters of interest, such as the radiation  $Q$  and the radiated power. Numerical simulations were used to optimize and more thoroughly study the antenna. Of course, the various parametric studies are constrained to maintain a tenable simulation space; only one parameter is varied at a time within a domain of interest. Nevertheless, this study provides a very

*Chapter 8. Conclusions*

valuable and necessary foundation for the experimental realization of the antenna.

# References

- [1] P. Kumar, S. Altunc, C. E. Baum, C. G. Christodoulou, E. Schamiloglu, and C. J. Buchenauer, “Radially Inhomogeneous Spherical Dielectric Lens for Matching 100 ps Pulses into Biological Targets,” *IEEE Transactions Plasma Science, Special Issue - Nonthermal Medical/Biological Applications Using Ionized Gases and Electromagnetic Fields*, vol. 38, pp. 1915–1927, Aug. 2010.
- [2] C. E. Baum, “Tiny Fast-Pulse B-Dot and D-Dot Sensors in Dielectric Media,” *Sensor and Simulation Note 544*, June 2009.
- [3] S. Altunc, C. E. Baum, C. G. Christodoulou, and E. Schamiloglu, “Lens Design for a Prolate-Spheroidal Impulse Radiating Antenna (IRA),” *Sensor and Simulation Note 525*, Oct. 2007.
- [4] P. Kumar, S. Altunc, C. E. Baum, C. G. Christodoulou, and E. Schamiloglu, “Investigation of various switch configurations,” *EM Implosion Memo 39*, Feb. 2010.
- [5] P. Kumar, S. Altunc, C. E. Baum, C. G. Christodoulou, and E. Schamiloglu, “Effect of the impedance of a bicone switch on the focal impulse amplitude and beam width,” *EM Implosion Memo 38*, Feb. 2010.
- [6] D. R. Grischkowsky and N. Katzenellenbogen, *Femtosecond Pulses of THz Radiation: Physics and Applications*, vol. 9, pp. 9–14. Washington, DC: OSA

## REFERENCES

- Proceedings on Picosecond Electronics and Optoelectronics, Optical Society of America, 1991.
- [7] C. E. Baum, “From the Electromagnetic Pulse to High-Power Electromagnetics,” *IEEE Proc.*, vol. 80, pp. 789–817, June 1992.
- [8] R. Nuccitelli, U. Pliquett, X. Chen, W. Ford, R. J. Swanson, S. J. Beebe, J. F. Kolb, and K. H. Schoenbach, “Nanosecond Pulse Electric Fields Cause Melanomas to Self-Destruct,” *Biochemical and Biophysical Research Communications*, vol. 343, p. 351, 2006.
- [9] J. Zhang, P. F. Blackmore, B. Y. Hargrave, S. Xiao, S. J. Beebe, and K. H. Schoenbach, “Nanosecond Pulse Electric Field (nanopulse): A Novel Non-Ligand Agonist for Platelet Activation.,” *Arch. Biochem. Biophys.*, vol. 471, pp. 240 – 248, Mar. 2008.
- [10] S. Altunc, *Focal Waveform of a Prolate-Spheroidal Impulse Radiating Antenna (IRA)*. PhD thesis, University of New Mexico, Dec. 2007.
- [11] K. H. Schoenbach, B. Hargrave, R. P. Joshi, J. F. Kolb, C. Osgood, R. Nuccitelli, A. Pakhomov, R. J. Swanson, M. Stacey, J. A. White, S. Xiao, J. Zhang, S. J. Beebe, P. F. Blackmore, and E. S. Buescher, “Bioelectric Effects of Intense Nanosecond Pulses,” *IEEE Transactions on Dielectrics and Electrical Insulation*, vol. 14, pp. 1088 – 1119, Oct. 2007.
- [12] K. H. Schoenbach, C. E. Baum, R. P. Joshi, and S. J. Beebe, “A Scaling Law for Membrane Permeabilization with Nanopulses,” *IEEE Trans. on Dielectrics and Electrical Insulation, Special Issue on Bioelectrics*, vol. 16, pp. 1224 – 1235, Oct. 2009.
- [13] K. H. Schoenbach, S. Xiao, R. P. Joshi, J. T. Camp, T. Heeren, J. F. Kolb, and S. J. Beebe, “The Effect of Intense Subnanosecond Electrical Pulses on

## REFERENCES

- Biological Cells,” *IEEE Transactions on Plasma Science*, vol. 36, pp. 414 – 422, Apr. 2008.
- [14] S. Xiao, S. Guo, J. T. Camp, N. Vasyly, A. Pakhomov, R. Heller, and K. H. Schoenbach, “Biological Cells Response to High Power Electromagnetic Pulses,” *Invited talk at the IEEE Int. Power Modulator and High Voltage Conf.*, vol. 9O1/2, May 2010.
- [15] C. E. Baum, “Focal waveform of a prolate-spheroidal impulse-radiating antenna,” *Radio Sci.*, vol. 42, no. RS6S27, 2007.
- [16] S. Xiao, S. Altunc, P. Kumar, C. E. Baum, and K. H. Schoenbach, “A Reflector Antenna for Focusing in the Near Field,” *IEEE Antennas and Wireless Propagation Letters*, vol. 9, pp. 12 – 15, 2010.
- [17] S. Altunc, C. E. Baum, C. G. Christodoulou, E. Schamiloglu, and C. J. Buchenauer, “Design of a Special Dielectric Lens for Concentrating a Sub-nanosecond Electromagnetic Pulse on a Biological Target,” *IEEE Transactions on Dielectrics and Electrical Insulation*, vol. 16, pp. 1364–1375, Oct. 2009.
- [18] K. H. Schoenbach, R. P. Joshi, J. F. Kolb, N. Chen, M. Stacey, P. F. Blackmore, E. S. Buescher, and S. J. Beebe, “Ultrashort Electric Pulses Open a New Gateway into Biological Cells,” *IEEE Proceedings*, vol. 92, pp. 1122 – 1137, July 2004.
- [19] D. V. Giri and F. M. Tesche, “Classification of intentional electromagnetic environments (IEME),” *IEEE Trans. on Electromagnetic Compatibility*, vol. 46, pp. 322–328, Aug. 2004.
- [20] International Electrotechnical Commission, “Electromagnetic compatibility (EMC) Part 2-13:Environment High-power electromagnetic (HPEM) environments Radiated and conducted,” Mar. 2005.

## REFERENCES

- [21] C. E. Baum, D. V. Giri, and E. G. Farr, "John Kraus Antenna Award," *IEEE Antennas and Propagation Magazine*, vol. 48, pp. 101–102, June 2006.
- [22] S. Altunc, C. E. Baum, C. G. Christodoulou, E. Schamiloglu, and G. Buchenauer, "Focal Waveforms for Various Source Waveforms Driving a Prolate-Spheroidal Impulse Radiating Antenna," *Radio Sci.*, vol. 43, Feb. 2008.
- [23] C. E. Baum, "Focal Waveform of a Prolate-Spheroidal IRA," *Sensor and Simulation Note 509*, Feb. 2006.
- [24] C. E. Baum, "Addition of a Lens Before the Second Focus of a Prolate-Spheroidal IRA," *Sensor and Simulation Note 512*, Apr. 2006.
- [25] C. E. Baum and A. P. Stone, *Transient Lens Synthesis (Electromagnetics Library Series)*. Taylor and Francis, First ed., 1990.
- [26] C. E. Baum and J. M. Lehr, "Tapered Transmission-Line Transformers for Fast High-Voltage Transients," *IEEE Trans. in Plasma Sci.*, vol. 30, pp. 1712 – 1721, 2002.
- [27] C. E. Baum, S. Altunc, and P. Kumar, "Scaling Relationships for Electromagnetic Parameters for Focusing Graded Dielectric Lenses," *Sensor and Simulation Note 537*, Apr. 2009.
- [28] S. Altunc, C. E. Baum, C. G. Christodoulou, and E. Schamiloglu, "Increasing Lens-Medium Permittivity Over Target-Medium Permittivity to Increase Electric Field and Decrease Spot Size at Target," *Sensor and Simulation Note 529*, June 2008.
- [29] C. E. Baum, S. Altunc, K. H. Schoenbach, and S. Xiao, "Focusing an Electromagnetic Implosion Inside Tissue," *Bioelectric Note 3*, Oct. 2008.
- [30] J. S. Tyo, "Optimization of the Feed Impedance for an Arbitrary Crossed-Fed-Arm Impulse Radiating Antenna," *Sensor and Simulation Note 438*, Nov. 1999.

## REFERENCES

- [31] M. J. Baretela and J. S. Tyo, "Improvement of Prompt Radiated Response from Impulse Radiating Antennas by Aperature Rrimming," *IEEE Trans. Antennas Propagat.*, vol. 51, pp. 2158 – 2167, 2003.
- [32] C. E. Baum, *Electromagnetic Sensors and Measurement Techniques*, pp. 73 – 144 in J. E. Thompson and L.H. Luessen. *Fast Electrical and Optical Measurements*, Martinus Nijhoff Publishers, Dordrecht, 1986.
- [33] C. E. Baum, S. Altunc, C. G. Christodoulou, and E. Schamiloglu, "Electromagnetic Implosion Using an Array," *IEEE Transactions on Plasma Science*, vol. 36, pp. 757 – 763, 2008.
- [34] C. E. Baum, "Accuracy Considerations in the Design of B-Dot and I-Dot Sensors," *Sensor and Simulation Note 344*, June 1992.
- [35] G. D. Sower, "Optimization of the Asymptotic Conical Dipole EMP Sensors," *Sensor and Simulation Note 544*, Oct. 1986.
- [36] C. E. Baum, "Electromagnetic Sensors and Measurement Techniques," *J. E. Thompson and L. H. Leussen, Fast Electrical and Optical Measurements*, pp. 73–144, 1986.
- [37] C. E. Baum, "An Equivalent-Charge Method for Defining Geometries of Dipole Antennas," *Sensor and Simulation Note 72*, Jan. 1969.
- [38] C. E. Baum, "A Circular Conical Antenna Simulator," *Sensor and Simulation Note 36*, Mar. 1967.
- [39] C. E. Baum, "A Conical-Transmission-Line Loop," *Sensor and Simulation Note 42*, May 1967.
- [40] T. K. Liu, "Impedances and Field Distributions of Curved Parallel-Plate Transmission-Line Simulators," *Sensor and Simulation Note 170*, Feb. 1973.



## REFERENCES

- [41] D. R. Wilton, "Static Analysis of Conical Antenna Over a Ground Plane," *Sensor and Simulation Note 224*, Aug. 1976.
- [42] E. G. Farr and C. E. Baum, "Prepulse Associated with the TEM Feed of an Impulse Radiating Antenna," *Sensor and Simulation Note 337*, Mar. 1992.
- [43] P. Kumar, S. Altunc, C. E. Baum, C. G. Christodoulou, and E. Schamiloglu, "Experimental results for the focal waveform and beam width in air with a 100 ps filter," *EM Implosion Memo 50*, July 2010.
- [44] P. Kumar, S. Altunc, C. E. Baum, C. G. Christodoulou, and E. Schamiloglu, "Experimental results for the focal waveform and beam width in the focusing lens with a 100 ps filter," *EM Implosion Memo 51*, July 2010.
- [45] S. Altunc, C. E. Baum, J. C. Buchenauer, C. G. Christodoulou, and E. Schamiloglu, "Testing a Sample Slab to Be Used as a Focusing Lens Layer," *EM Implosion Memo 24*, May 2008.
- [46] P. Kumar, S. Altunc, C. E. Baum, C. G. Christodoulou, and E. Schamiloglu, "An artificial dielectric consisting of a random array of short, thin wires embedded in a dielectric medium," *EM Implosion Memo 36*, Nov. 2009.
- [47] D. V. Giri, J. M. Lehr, W. D. Prather, C. E. Baum, and R. J. Torres, "Intermediate and Far Fields of a Reflector Antenna Energized by a Hydrogen Spark-Gap Switched Pulser," *IEEE Trans. Plasma Sci.*, vol. 28, pp. 1631–1636, Oct. 2000.
- [48] C. E. Baum, E. G. Farr, and D. Giri, *Review of impulse-radiating antennas*, pp. 403–439 in W. R. Stone. *Review of Radio Science*, Oxford Univ. Press, New York, 1996-1999.

## REFERENCES

- [49] S. Altunc, C. E. Baum, C. G. Christodoulou, and E. Schamiloglu, “Analytical calculations of a lens for launching a spherical TEM wave,” *Sensor and Simulation Note 534*, Oct. 2008.
- [50] P. Kumar, S. Altunc, C. E. Baum, C. G. Christodoulou, and E. Schamiloglu, “Analytical considerations for curve defining boundary of a non-uniform launching lens,” *EM Implosion Memo 26*, June 2009.
- [51] P. Kumar, S. Altunc, C. E. Baum, C. G. Christodoulou, and E. Schamiloglu, “Simulation results for 3-layer and 6-layer planar non-uniform launching lens,” *EM Implosion Memo 27*, June 2009.
- [52] P. Kumar, S. Altunc, C. E. Baum, C. G. Christodoulou, and E. Schamiloglu, “Derivation of the dielectric constant as a function of angle for designing a conical non-uniform launching lens,” *EM Implosion Memo 28*, June 2009.
- [53] P. Kumar, S. Altunc, C. E. Baum, C. G. Christodoulou, and E. Schamiloglu, “Simulation results for 6-layer and 7-layer conical non-uniform launching lens,” *EM Implosion Memo 29*, June 2009.
- [54] P. Kumar, S. Altunc, C. E. Baum, C. G. Christodoulou, and E. Schamiloglu, “The truncated four feed-arm configuration with switch cones (T4FASC) and a spherical pressure vessel,” *EM Implosion Memo 42*, May 2010.
- [55] P. Kumar, S. Altunc, C. E. Baum, C. G. Christodoulou, and E. Schamiloglu, “150  $\Omega$  impedance-matched bicone switch configuration with a spherical pressure vessel,” *EM Implosion Memo 43*, May 2010.
- [56] P. Kumar, S. Altunc, C. E. Baum, C. G. Christodoulou, and E. Schamiloglu, “Design and numerical simulation of switch and pressure vessel setup - part I,” *EM Implosion Memo 31*, Aug. 2009.

## REFERENCES

- [57] P. Kumar, S. Altunc, C. E. Baum, C. G. Christodoulou, and E. Schamiloglu, “Design and numerical simulation of switch and pressure vessel setup - part II,” *EM Implosion Memo 32*, Aug. 2009.
- [58] P. Kumar, S. Altunc, C. E. Baum, C. G. Christodoulou, and E. Schamiloglu, “Design considerations for a cylindrical pressure vessel with a spherical launching lens,” *EM Implosion Memo 41*, Mar. 2010.
- [59] P. Kumar, S. Altunc, C. E. Baum, C. G. Christodoulou, and E. Schamiloglu, “The truncated four feed-arm configuration with switch cones (T4FASC) and a cylindrical pressure vessel,” *EM Implosion Memo 44*, May 2010.
- [60] P. Kumar, S. Altunc, C. E. Baum, C. G. Christodoulou, and E. Schamiloglu, “Optimization of the T4FASC-CSS-SPVSHC and T4FASC-CSS-CPVCHC configurations,” *EM Implosion Memo 45*, May 2010.
- [61] P. Kumar, S. Altunc, C. E. Baum, C. G. Christodoulou, and E. Schamiloglu, “Comparison of electromagnetic parameters for the T4FASC-CSS-SPVSHC and T4FASC-CSS-CPVCHC configurations with the focusing lens,” *EM Implosion Memo 46*, May 2010.
- [62] P. Kumar, S. Altunc, C. E. Baum, C. G. Christodoulou, and E. Schamiloglu, “Revisiting ODU’s requirements from the PSIRA,” *EM Implosion Memo 47*, May 2010.
- [63] C. E. Baum, P. Kumar, and S. Altunc, “Electron Drift Velocity and Ultrafast Gaseous Switching,” *Switching Note 35*, Apr. 2009.
- [64] P. Kumar, S. Altunc, C. E. Baum, C. G. Christodoulou, and E. Schamiloglu, “Structural support considerations for the launching lens,” *EM Implosion Memo 48*, May 2010.

## REFERENCES

- [65] P. Kumar, S. Altunc, C. E. Baum, C. G. Christodoulou, and E. Schamiloglu, “Scaling down the reflector dimensions,” *EM Implosion Memo 49*, May 2010.
- [66] C. E. Baum, P. Kumar, S. Altunc, C. G. Christodoulou, and E. Schamiloglu, “Matching Fast Electromagnetic Pulses into Dielectric Targets,” *Sensor and Simulation Note 552*, Feb. 2010.
- [67] P. H. Siegel, “Terahertz Technology,” *IEEE Transactions on Microwave Theory and Techniques*, vol. 50, pp. 910 – 928, Mar. 2002.
- [68] K. Sakai, *Terahertz Optoelectronics*. Springer, Heidelberg, 2005.
- [69] C. E. Baum, P. Kumar, S. Altunc, K. F. McDonald, C. Christodoulou, and E. Schamiloglu, “Choice of Frequencies for THz Atmospheric Transmission,” *Terahertz Memo 2*, Oct. 2009.
- [70] W. D. Prather, C. E. Baum, R. J. Torres, F. Sabath, and D. Nitsch, “Survey of Worldwide High-Power Wideband Capabilities,” *IEEE Transactions on Electromagnetic Compatibility*, vol. 46, pp. 335 – 344, Aug. 2004.
- [71] R. W. McMillan, “Advances in Sensing with Security Applications.” pp. 1 - 26, in J. Byrnes(ed.), *Terahertz Imaging Milimeter-Wave Radar*, Springer, Dordrecht, The Netherlands, 2006.
- [72] P. Kumar, C. E. Baum, S. Altunc, C. G. Christodoulou, and E. Schamiloglu, “Switched oscillator as an antenna,” *Terahertz Memo 1*, Sept. 2009.
- [73] C. E. Baum, “Switched Oscillators,” *Circuit and Electromagnetic System Design Note 45*, Sept. 2000.
- [74] C. E. Baum and P. Kumar, “Maximizing Energy in Terahertz Pulse Radiation from a Switched Oscillator,” *Sensor and Simulation Note 554*, July 2010.

## REFERENCES

- [75] C. E. Baum, “Combined Electric and Magnetic Dipoles for Mesoband Radiation, Part 2,” *Sensor and Simulation Note 531*, May 2008.
- [76] C. E. Baum, “Some Characteristics of Electric and Magnetic Dipole Antennas for Radiating Transient Pulses,” *Sensor and Simulation Note 125*, Jan. 1971.
- [77] P. Katehi and N. Alexopoulos, “On the Effect of Substrate Thickness and Permittivity on Printed Circuit Dipole Properties,” *IEEE Transactions on Antennas and Propagation*, vol. 31, pp. 34 – 39, Jan. 1983.
- [78] N. G. Alexopoulos, P. B. Katehi, and D. B. Rutledge, “Substrate Optimization for Integrated Circuit Antennas,” *IEEE Transactions on Microwave Theory and Techniques*, vol. 31, pp. 550 –557, July 1983.
- [79] D. M. Pozar, “Considerations for Millimeter Wave Printed Antennas,” *IEEE Transactions on Antennas and Propagation*, vol. 31, pp. 740 – 747, Sept. 1983.
- [80] F. Schwiring and A. A. Oliner, “Millimeter-Wave Antennas.” Ch. 17 in Y. T. Lo and S. W. Lee (eds.), *Antenna Handbook*, VanNostrand Reinhold, 1988.
- [81] N. Alexopoulos and D. Jackson, “Fundamental Superstrate (Cover) Effects on Printed Circuit Antennas,” *IEEE Transactions on Antennas and Propagation*, vol. 32, pp. 807 – 816, Aug. 1984.
- [82] C. E. Baum, “Terahertz Antennas and Oscillators Including Skin-Effect Losses,” *Sensor and Simulation Note 535*, Sept. 2008.
- [83] P. Kumar, C. E. Baum, D. R. Grischkowsky, K. F. McDonald, C. Christodoulou, and E. Schamiloglu, “Comparison of experimental and numerical simulation results for the 5-10-5 max1 antenna,” *Terahertz Memo 3*, Aug. 2010.
- [84] C. E. Baum, “Some Considerations Concerning Analytic EMP Criteria Waveforms,” *Theoretical Note 285*, Oct. 1976.

## REFERENCES

- [85] P. Kumar, C. E. Baum, K. F. McDonald, C. G. Christodoulou, and E. Schamiloglu, "Investigation of the skin-effect losses in a copper swo antenna above a copper ground plane," *Terahertz Memo 4*, Aug. 2010.
- [86] P. Kumar, C. E. Baum, K. F. McDonald, C. G. Christodoulou, and E. Schamiloglu, "Optimization of the substrate height for a copper SWO radiator above a copper ground plane," *Terahertz Memo 5*, Sept. 2010.
- [87] P. Kumar, C. E. Baum, K. F. McDonald, C. G. Christodoulou, and E. Schamiloglu, "The effect of the switch length and antenna width on the radiation quality factor and resonant frequency," *Terahertz Memo 6*, Sept. 2010.
- [88] M. E. Shaik, C. E. Baum, and C. G. Christodoulou, "Integrated Switched Oscillator and Zig-Zag Antenna with Photoconductive Semiconductor Switch as a Terahertz (THz) Pulse Transmitter," *Sensor and Simulation Note 541*, July 2009.
- [89] C. E. Baum, P. Kumar, and S. Altunc, "Arrays of Zig-Zag Antennas Driven by Switched Oscillators," *Sensor and Simulation Note 542*, Aug. 2009.
- [90] C. E. Baum, P. Kumar, and S. Altunc, "Line-Source Switched-Oscillator Antenna," *Sensor and Simulation Note 551*, Feb. 2010.
- [91] C. E. Baum, "From Small THz Arrays to Large Antenna Aperatures for THz Beams Propagating to Large Distances: The THz Flashlight," *Sensor and Simulation Note 549*, Aug. 2009.
- [92] C. E. Baum, "Downconverting THz Resonant Pulses upon Reception," *Circuit and Electromagnetic System Design Note 67*, June 2010.